

AD-A108 581

SAN FERNANDO LABS PACOIMA CA

F/G 11/6

INVESTIGATION OF THE CNTD MECHANISM AND ITS EFFECT ON MICROSTRU--ETC(U)

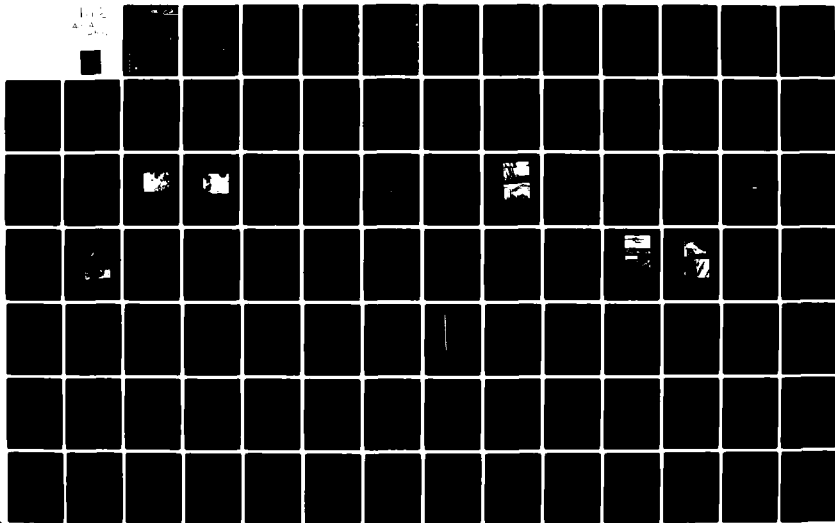
SEP 81 D G BHAT, R M PANOS

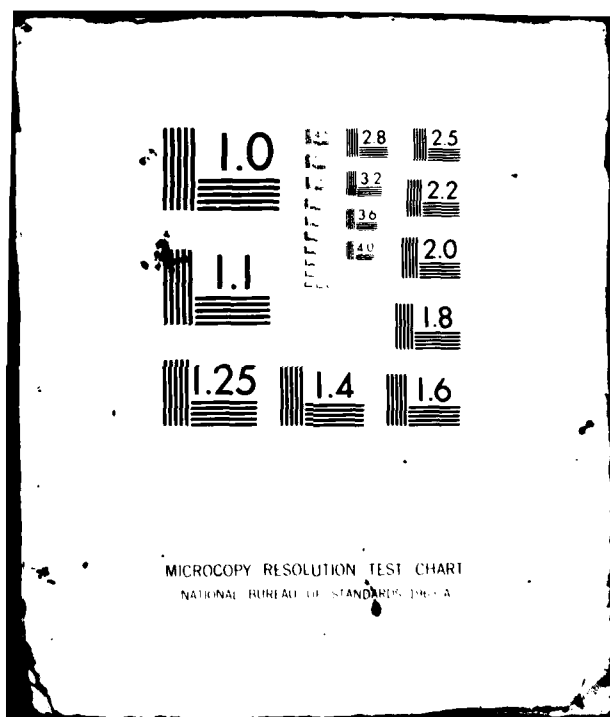
F49620-79-C-0041

UNCLASSIFIED

AFOSR-TR-81-0748

NL





AD A108581

INVESTIGATION OF THE CRYD MECHANISM AND THE
EFFECT ON MICROSTRUCTURAL PROPERTIES
of SIC and AIN

DTIC
DEC 19 1981

D. C. Bhat, Ph.D.

R. R. Panoos, Ph.D.

*Now with Litton Industries, San Diego, CA

San Fernando, California
10710 Santa Monica
Boulevard, CA 91340

September 1981

14 020

314549

Approved for public release
Distribution unlimited.

12

FOREWORD

The work described in this report was conducted under AFOSR Contract No. F49620-79-C-0041

We wish to thank the contract monitors Maj. W. Simmons and Capt. S. Wax for their guidance during the course of this work.

The deposition runs were conducted by Mr. S. Cerna.

We would like to thank Dr. J. Stiglich of San Fernando Laboratories and G. Quinn of AMMRC for the high temperature strength measurements and Dr. D. Kotchick of AiResearch for the Weibull analysis.

DTIC
ELECTE
DEC 15 1981
S H

TABLE OF CONTENTS

I.	INTRODUCTION	1
II.	SECTION II	
A.	CVD Systems	5
B.	Characterization of Materials.	9
B.1	Flexure Tests.	9
B.2	X-Ray Diffraction.	13
B.3	Scanning Electron Microscopy (SEM) and Energy Dispersive Analysis of X-Rays (EDAX).	13
B.4	Microprobe Analysis.	14
B.5	Microhardness and Fracture Toughness	14
III.	SECTION III	
	SiC Investigation - Results and Discussions	15
A.	First Year's Efforts	15
A.1	Furnace Process Attempts	18
A.2	SiCl ₂ Disproportionation	25
A.3	Deposition on Resistance Heated Graphite	30
B.	Second Year's Efforts	42
B.1	Furnace Development.	43
B.1a	Slotted Top Furnace.	43
B.1b	Slotted Wall Furnace	46
B.1c	Flower Pot Furnace	48
B.2	Elevated Temperature Strength Testing.	50
B.3	Elemental Analysis	68
B.4	Residual Stress Measurements	77
B.5	Correlation with Run Conditions.	84
C.	Summary and Conclusions.	86
IV.	SECTION IV	
	AlN Results and Discussions.	89
A.	Structural Material.	89
A.1	Equipment and Procedures	90

Accession #	
NTIS	DTIC
Unannounced Justification	
By	Distribution/
89	Availability Code
90	Avail and/or Special
Dis:	
A	

REPORT DOCUMENTATION PAGE		READ INSTRUCTIONS BEFORE COMPLETING FORM
1. REPORT NUMBER AFOSR-TR. 81-0748	2. GOVT ACCESSION NO. AD-4108581	3. RECIPIENT'S CATALOG NUMBER
4. TITLE (and Subtitle) Investigation of the CNTD Mechanism and its Effect on Microstructural Properties of SiC and AlN	5. TYPE OF REPORT & PERIOD COVERED FINAL	
7. AUTHOR(s) Deepak G. Bhat, Ph.D. Rodney M. Panos, Ph.D.*	6. PERFORMING ORG. REPORT NUMBER	
9. PERFORMING ORGANIZATION NAME AND ADDRESS San Fernando Laboratories 9N294 10258 Norris Avenue Pacoima, CA 913312281	8. CONTRACT OR GRANT NUMBER(s) F49620-79-C-0041	
AFOSR/NE BOLLING A.F.B., D.C. BLDG. 410 WASH. D.C. 20332	10. PROGRAM ELEMENT, PROJECT, TASK AREA & WORK UNIT NUMBERS 2306/A2 61102F	
	12. REPORT DATE September 1981	
14. MONITORING AGENCY NAME & ADDRESS (if different from Controlling Office)	13. NUMBER OF PAGES 175	
	15. SECURITY CLASS. (of this report) Unclassified	
15a. DECLASSIFICATION/DOWNGRADING SCHEDULE		
16. DISTRIBUTION STATEMENT (of this Report) Approved for public release; distribution unlimited.		
17. DISTRIBUTION STATEMENT (of the abstract entered in Block 20, if different from Report)		
18. SUPPLEMENTARY NOTES *Now at Litton Industries, Woodland Hills, California.		
19. KEY WORDS (Continue on reverse side if necessary and identify by block number) CNTD (Controlled Nucleation Thermochemical Deposition), Silicon carbide, Elevated temperature, Weibull analysis, furnace design, Aluminum Nitride, Structural AlN, Electrical and Thermal properties, IR transmission, Residual stress analysis, surface finish.		
20. ABSTRACT (Continue on reverse side if necessary and identify by block number) The report describes the development of a CNTD process for silicon carbide. Following earlier work on resistance-heated substrate, attempts were made to develop a furnace process for CNTD SiC. High temperature flexure testing of SiC-coated graphite bend bars showed that the CNTD SiC was superior to other conventional SiC materials over the whole range of temperatures tested. Problems were encountered in attaining uniformity and repeatability of the material. All deposits tested showed a two-phase		

DD FORM 1 JAN 73 1473

EDITION OF 1 NOV 65 IS OBSOLETE

SECURITY CLASSIFICATION OF THIS PAGE (When Data Entered)
Unclassified

structure of Si and SiC. Highly variable compressive surface stresses were observed by XRD techniques. Attempts to develop a CNTD process for AlN were not successful, However, grain refinement and improvement in physical properties were achieved when AlN deposits were "doped" with Si. The electrical and thermal properties of CVD AlN were comparable to other AlN materials. The IR transmittance characteristics were found to be inferior, possibly due to impurities in the deposit.

TABLE OF CONTENTS CONTINUED

A.2	Parametric Investigation	92
A.2a	Equipment Adjustments.	92
A.2b	Deposition Parameters.	97
A.2c	General Materials Character- ization.	101
A.3	Alloying Experiments	105
B.	Characterization of Electrical, Thermal and IR Properties	111
B.1	Equipment and Procedures	116
B.2	Electrical Properties.	118
B.3	Thermal Conductivity Measurements	123
B.4	IR Transmission.	125
B.5	Acid Etch Tests.	126
C.	Summary of AlN Work.	127

APPENDIX A

Deposition Run Conditions for CNTD SiC and CVD AlN	129
---	-----

APPENDIX B

A Report On the Study of the Effect of Surface Finish of Graphite Substrates On the TRS of Uncoated and SiC-Coated Bend Bars	142
---	-----

APPENDIX C

X-Ray Diffraction Determination of the Surface Residual Stress and Elastic Properties of β -SiC Coatings on Graphite Substrates.	151
---	-----

APPENDIX D

Aluminum Nitride Thermochemistry	168
REFERENCES	174

LIST OF FIGURES

<u>NUMBER</u>	<u>DESCRIPTION</u>	<u>PAGE</u>
Figure 1	Schematic Of A Typical Flow Control Panel For SiC Deposition	7
Figure 2	Calculation Of Flexure Strength Of Composite Beam By The Method Of Equivalent Section	10
Figure 3	Loading Configurations In Flexure Tests	11
Figure 4	Scanning Transmission Electron Micrograph Of CNTD SiC Deposit Showing The Extremely Fine-Grained Microstructure	16
Figure 5	Scanning Transmission Electron Micrograph Of CNTD SiC	17
Figure 6	Schematic Of SiC Deposition Apparatus Showing Radiant (Furnace) Heating Arrangement.	20
Figure 7	Fractographs Of SiC Deposited In A Furnace	22
Figure 8	Schematic Of SiC Deposition Apparatus Using Silicon Halide Disproportionation Scheme	26
Figure 9	Fractographs Of Silicon Deposited In The Silicon Disproportionation System	29
Figure 10	Schematic Of SiC Deposition Apparatus Showing Resistance Heating Arrangement	32
Figure 11	Fractographs Of SiC Deposited On Resistively Heated Graphite Substrate Using Propane and MTS	38
Figure 12	Structure Of CNTD SiC.	39
Figure 13	Variation Of Hardness Of CNTD SiC Deposited On Resistance-Heated Graphite As A Function Of Silicon Content Of The Deposit	41

LIST OF FIGURES
CONTINUED

<u>NUMBER</u>	<u>DESCRIPTION</u>	<u>PAGE</u>
Figure 14	Schematic Of The Slotted-Top Furnace Design	44
Figure 15	Schematic Arrangement Of The Depo- sition Chamber For SiC Deposition Using The Slotted-Top Furnace	45
Figure 16	Longitudinal Section Of The Slotted Wall Graphite Furnace Used In SiC Deposition	47
Figure 17	Longitudinal Cross-Section Through The "Flower Pot" Furnace Showing The Arrangement Of Individual Segments Allowing Variable Spacing To Control Gas Flow.	49
Figure 18	Flexure Strength Of CNTD SiC As A Function Of Test Temperature	54
Figure 19	Flexure Strength Of CNTD SiC As A Function Of Temperature In Compar- ison To Siliconized SiC Materials. . .	55
Figure 20	Flexure Strength Of CNTD SiC As A Function Of Temperature In Compar- ison To Sintered SiC Materials	56
Figure 21	Flexure Strength Of CNTD SiC As A Function Of Temperature In Compar- ison To The Hot-Pressed SiC Materials.	57
Figure 22	Weibull Plot Of Room Temperature, 3-point Flexure Strength Data (Strain Rate = 0.15 mm/min) On CNTD SiC Deposited On Graphite	60
Figure 23	Weibull Plot Of 600°C, 4-point Flexure Strength Data (Strain Rate = 0.5 mm/min) On CNTD SiC Deposited On Graphite	61
Figure 24	Weibull Plot Of 1000°C Flexure Strength (4-point) Data For CNTD SiC Deposited On Graphite	62

LIST OF FIGURES
CONTINUED

<u>NUMBER</u>	<u>DESCRIPTION</u>	<u>PAGE</u>
Figure 25	Weibull Plot Of 1200°C, 4-point Flexure Strength Data At Different Strain Rates For CNTD SiC Deposited On Graphite	63
Figure 26	Weibull Plot Of 1370°C, 4-point Flexure Strength Data At Different Strain Rates For CNTD SiC Deposited On Graphite	64
Figure 27	Weibull Plot Of 1370°C Flexure Strength Data (4-point, 0.5 mm/min Strain Rate) For CNTD SiC Deposited On Graphite	65
Figure 28	Weibull Plot Of 1370°C, 4-point Flexure Strength Data (Strain Rate = 0.05 mm/min) For CNTD SiC Deposited On Graphite.	66
Figure 29	Elastic Modulus As A Function Of Temperature For Various SiC Materials	73
Figure 30	Normalized High-temperature Flexure Strength Of CNTD SiC On Graphite Bend Bars As A Function Of Excess Silicon (Furnace Deposits) .	74
Figure 31	Variation Of Hardness Of CNTD SiC Deposited On Graphite As A Function Of Excess Silicon (Furnace Deposits) .	76
Figure 32	Comparison Of The Variation Of Hardness As A Function Of Excess Silicon For CNTD SiC Made On Resistance-Heated And Radiation-Heated Graphite .	78
Figure 33	Residual Stress In A Flat Plate Of CNTD SiC Deposited On SiC ₆ Graphite Substrate	81
Figure 34	Residual Stress In A 12.7 mm Diameter Cylinder Of CNTD SiC ₆ Deposited On SiC Graphite Substrate	82

LIST OF FIGURES
CONTINUED

<u>NUMBER</u>	<u>DESCRIPTION</u>	<u>PAGE</u>
Figure 35	Residual Stress In A 38.1 mm Diameter Cylinder Of CNTD SiC Deposited On SiC ₆ Graphite Substrate.	83
Figure 36	Schematic Of AlN Deposition Apparatus Using Radiant (Furnace) Heating Method	91
Figure 37	Effect Of Increasing NH ₃ /AlCl ₃ Ratio On The Microstructure Of AlN.	100
Figure 38	Crystal Morphologies Of CVD AlN Deposits	102
Figure 39	Columnar Crystal Habit On The Fracture Surface Of A Typical AlN Deposit. The Substrate Is A Molybdenum Filament.	103
Figure 40	Deposit Of AlN Showing A Non-Homogeneous Incorporation Of Silicon "Dopant"	108
Figure 41	Microstructure Of Silicon-doped AlN Deposit Electrolytically Etched In A CrO ₃ /HF Solution, Showing The Banded Structure Of AlN.	109
Figure 42	Fractographs Showing The Effect Of "Doping" On The Crystal Morphology	113
Figure 43	X-Ray Elemental Dot Maps For Silicon-Doped AlN Deposit.	114
Figure 44	X-Ray Line Scan Through The Cross-Section Of CVD AlN "Doped" With Silicon Showing The Distribution Of Al, Si and Residual Chlorine In The Deposit	115
Figure 45	Schematic Of AlN Deposition Apparatus sing Induction Heating.	117

LIST OF FIGURES
CONTINUED

<u>NUMBER</u>	<u>DESCRIPTION</u>	<u>PAGE</u>
Figure 46	Electrical Conductivity Of CVD AlN As A Function Of Frequency And Temperature	119
Figure 47	The Variation Of Dielectric Constant As A Function Of Frequency And Temperature For CVD AlN	120
Figure 48	The Variation Of Loss Tangent As A Function Of Frequency And Temperature For CVD AlN	121
Figure 49	Schematic Arrangement Of Apparatus Used For The Measurement Of Electrical Properties Of CVD AlN . . .	122
Figure 50	Variation Of Thermal Conductivity With Temperature Of Various AlN Materials	124
Figure B-1	Effect Of Surface Finish On The Flexure Strength Of Uncoated Graphite Bend Bars	146
Figure B-2	Effect Of Substrate Surface Finish On The Flexure Strength Of CNTD SiC Coating	148
Figure C-1	Change In The (311) Lattice Spacing Of CNTD SiC As A Function Of Applied Stress	159
Figure D-1	Change In The Free Energy Of Formation As A Function Of Temperature For Reactions In The Aluminum Crucible In The CVD Of AlN. .	169
Figure D-2	Change In The Free Energy Of Formation As A Function Of Temperature For Reactions In The Gas Phase And Deposition Chamber In The CVD Of AlN	170
Figure D-3	Change In The Free-Energy Of Formation As A Function Of Temperature Of Secondary Reaction Products In The CVD Of AlN	172

LIST OF TABLES

<u>NUMBER</u>	<u>DESCRIPTION</u>	<u>PAGE</u>
Table 1	Properties Of Silicon Carbide Deposited In A Conventional Furnace.	21
Table 2	Properties Of Silicon Deposited By Disproportionation.	28
Table 3	Silicon Carbide Deposited On Resistively Heated Substrates.	34
Table 4	Flexure Strength Data For CNTD SiC	51
Table 5	Chemical Analysis Of CNTD SiC Samples.	69
Table 6	Carbon Residue Analysis.	70
Table 7	Excess Silicon In CNTD SiC Samples Flexure Tested At Various Temperatures	72
Table 8	Surface Residual Stress In CNTD SiC Deposit As Measured By XRD	80
Table 9	Correlation Of Deposition Conditions With Properties Of CNTD SiC.	85
Table 10	Coefficients Of Thermal Expansion For Various Substrate Materials	95
Table 11	Results Of X-Ray Diffraction	98
Table 12	Effect Of Oxygen Additions On The Properties Of CVD AlN	106
Table 13	Effect Of Silicon Additions On The Properties Of CVD AlN	110
Table 14	Effect Of Aluminum Addition On The Properties Of CVD Si ₃ N ₄	112
Table A-1	Deposition Parameters For CNTD SiC Using SiCl ₄ And MTS As Silicon Sources	130
Table A-2	Deposition Parameters For CNTD SiC Using Propane and MTS.	132

LIST OF TABLES
CONTINUED

<u>NUMBER</u>	<u>DESCRIPTION</u>	<u>PAGE</u>
Table A-3	Deposition Parameters For CNTD SiC Using C ₃ H ₈ and CH ₄ As Carbon Sources .	134
Table A-4	Deposition Parameters For AlN - Initial Experiments	136
Table A-5	Deposition Parameters For AlN	137
Table A-6	Deposition Parameters For AlN - Oxygen Dopant Study.	139
Table A-7	Deposition Parameters For AlN - Silicon Dopant Study	140
Table A-8	Deposition Parameters For AlN - Low Pressure Deposition Study	141
Table B-1	Strength Of SiC Deposited On SiC ₆ Graphite Bend Bars With Different Surface Finishes	149
Table C-1	Diffractometer Parameters	153
Table C-2	Surface Residual Stress β -SiC Coated Graphite	162
Table C-3	Repeat Residual Stress Measurements - Beta Silicon Carbide	164

SECTION I

INTRODUCTION

This final Technical Report covers work conducted under AFOSR Contract F49620-79-C-0041 during the period 15 January 1979 to 15 January 1981. This work was concerned with two materials: vapor deposited SiC and AlN. The work on SiC consisted of an investigation of the effects of the CNTD (Controlled Nucleation Thermochemical Deposition) ^{1,2} process on the microstructure and physical properties of the resulting material.

The SiC investigation was part of an extended effort which actually began in March 1977. Under AFOSR sponsorship (Contract No. F49620-77-0086) we carried out a series of experiments during the period which ended 15 December 1978. We explored the characteristics of the CNTD SiC process, previously developed at San Fernando Laboratories. This first effort began by establishing a suitable set of operating conditions for reproducible CNTD SiC deposition in the simplest experimental system. The program was then expanded into a more systematic exploration of the sensitivity of the CNTD SiC mechanism to the operating conditions, followed by attempts to fundamentally improve the process. At the end of the program CNTD SiC material was being consistently deposited with high strength, hardness, and fracture toughness. Furthermore, we achieved a better understanding of the fundamental mechanism of the CNTD process and were able to define its operating limits for the simple experimental system that was used.

The effort described in this report was aimed at extending CNTD SiC process from the relatively simple method of deposition on resistively heated tungsten filaments (used in the first program) to a more useful method of deposition on substrates heated in a furnace by radiation. The first year of this latter study began with three main objectives: (a) to determine the operating parameters for CNTD SiC production in a furnace, (b) to examine alternative chemical systems in order to further understand the CNTD mechanism as it relates to SiC, and (c) to eliminate the influence of substrate on strength measurements by using graphite substrates.

The first year's effort provided a somewhat more complete knowledge of the required operating conditions. Primarily we gained an understanding of the importance of a proper balance between the gas and substrate temperatures. However, we did not deposit CNTD material similar to that obtained on tungsten filaments.

During the second year, a furnace CNTD SiC process was established with the aid of results from an internal SFL-sponsored development program. We then devoted our attention to characterizing the material produced by this process.

The results of various tests showed that, although the material had superior mechanical properties, they were also highly variable. We found that the deposit contained varying amounts of free silicon and also had considerable compressive residual stresses.

We were unable to establish the exact relationship between the variable material properties and the deposition conditions. It was clear that the CNTD SiC furnace process was extremely sensitive to operating parameters and that we had not achieved adequate control over the process at the conclusion of this program.

The AlN investigation had two goals. First, we sought to develop a CNTD process for AlN and to characterize the resulting material and the second, we attempted to develop a method for vapor depositing an AlN material which would have good electro-optical characteristics. We believed that the properties required for each application differed considerably. For instance, a highly oriented crystal structure in conjunction with the best attainable chemical purity is required for optical uses. CNTD material, on the other hand, would be strong, fine grained, and noncolumnar. To achieve this, we attempted the addition of selected species in order to enhance the interruption of columnar crystal growth through the formation of a second phase.

We did not produce a CNTD AlN material. However, we were successful in making some very fine grained AlN deposits with the aid of competing AlN and Si_3N_4 deposition reactions. These materials were characterized by SEM techniques.

We also attempted to deposit some highly pure and oriented AlN material for possible electro-optic applications. We could not make the deposits sufficiently pure. The

principal contaminants were found to be chlorine and oxygen in all samples.

We carried out measurements of thermal and electrical conductivities and also of infrared transmission characteristics of the AlN deposits. The results reflected the fact that the deposits contained significant amounts of impurities.

One of the sources of contamination of the deposits was clearly the gas delivery system. We did not, however, attempt to refine the process since electro-optical AlN was not the major concern of the development program.

SECTION II-A

CVD SYSTEMS

A CVD system contains two important subsystems: a heating system and a vaporizing system.

The type of heating is limited, in part, by the characteristics of the substrate material and in part, by the characteristics of the deposit. Vaporizing systems are designed for, and constrained by, the type of reactant gases required.

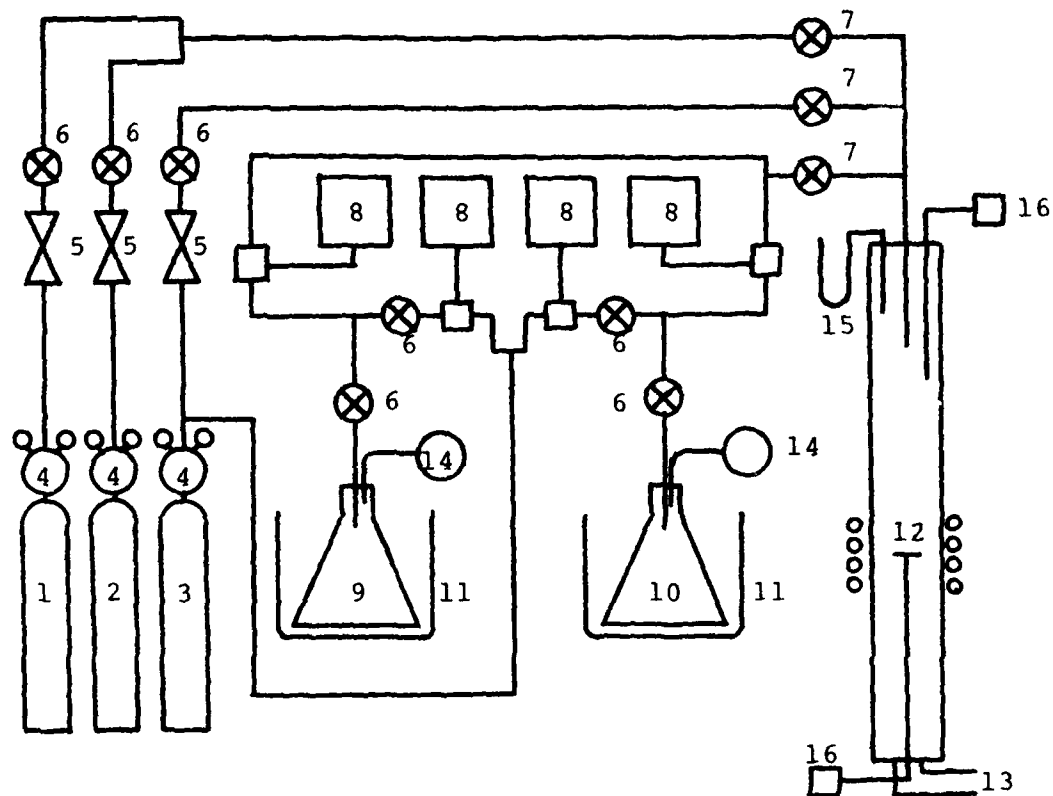
Heating techniques for CVD can be chosen from a wide variety of available methods ranging from IR radiation and electron beam bombardment, to simple internal resistance. During this investigation three methods were used: induction heating, internal resistance heating, and radiant heating. Induction heating and resistance heating are used widely and are fundamentally related. Resistance heating involves passing a current through the substrate specimen, while induction heating causes eddy currents to circulate within the substrate through induction coupling. The primary advantage to both methods is their ability to heat the substrate without heating the container walls. Both methods are limited to fairly conductive substrate materials with simple geometries. Radiant heating involves heating the substrate by radiation from the hot furnace walls. This technique is not limited to simple substrate geometries. Also, it is more suitable for large scale production. There

are, however, difficulties arising from deposition on the furnace walls, or on the containment vessel, and from problems of managing the gas temperature.

There is also a wide variety of techniques for the production of volatile reactants. Reactants can be supplied directly as gas from pressurized cylinders, vaporized from condensed phases, or created in-situ by chemical reaction. During the work reported herein, all three general techniques were used. Figure 1 illustrates a CVD system for silicon carbide deposition.

Silicon carbide deposition requires the delivery of hydrogen and carrier gases (argon or nitrogen), which are metered directly from pressurized cylinders, and also of silicon compounds, such as silicon tetrachloride or methyltrichlorosilane (MTS), which must be vaporized from a liquid. Liquids were vaporized using a sealed "boiler" vessel. By maintaining a suitable temperature in the "boiler" the reactant vapor pressure can be held high relative to the carrier line. The reactant vapor can then be injected under positive pressure into a flow of inert carrier gas and carried into the deposition chamber as a dilute vapor.

The AlN deposition system involved yet another method of producing volatile reactants using an in-situ chemical reaction. One of the reactants in the AlN system, gaseous AlCl_3 , is produced by "burning" solid aluminum granules in HCl gas at about 450°C . Gaseous AlCl_3 is then carried to the deposition



Legend

- | | |
|--------------------|--------------------------------|
| (1) Hydrogen | (9) MTS Boiler |
| (2) Hydrocarbon | (10) SiCl_4 Boiler |
| (3) Argon/Nitrogen | (11) Constant Temperature Bath |
| (4) Regulators | (12) Deposition Zone |
| (5) Rotameters | (13) To Vacuum Pump |
| (6) Metering Valve | (14) Pressure Gauge |
| (7) Shut-off Valve | (15) U-Tube Manometer |
| (8) Mass Flowmeter | (16) Temperature Indicator |

FIGURE 1: SCHEMATIC OF A TYPICAL FLOW CONTROL PANEL FOR SiC DEPOSITION.

area where it is mixed with ammonia gas, which is metered directly from pressurized cylinders.

Figure 1 represents a typical gas flow system for the production of silicon carbide. Hydrogen, hydrocarbon, and argon/nitrogen gases are dispensed through standard borosilicate glass rotameters with pressure gauges and needle valves for maintaining constant metering pressure. We introduced Hastings Mass Flow meters in the place of rotameters in order to obtain greater accuracy and control over flow rates. Silicon bearing species (MTS or SiCl_4) are introduced using argon or nitrogen as a carrier gas. The boiler temperature is maintained by immersion in a constant temperature bath. The flow of silicon species is determined by measuring the difference between the flow of the carrier gas alone and the flow of carrier gas plus active species (MTS or SiCl_4).

Various types of deposition chambers were used during the course of experiments described herein. These are described in detail within those sections of the text dealing with specific experiments.

Vacuum exhaust was supplied by a chilled water aspirator pumping system and a 15 hp Sihi water ring vacuum pump.

II-B Characterization of Materials

Various techniques have been used in the course of this program to evaluate and characterize the materials fabricated. Unless otherwise specified within subsequent sections, these characterization techniques were performed as described below.

II-B.1 Flexure Tests

Most of the mechanical tests performed routinely at SFL were performed on a table mounted mechanical testing machine made by the Comten Corp., St. Petersburg, FL. Three-and-four-point flexure fixtures were used which incorporated sintered tungsten carbide load pins. Various span lengths were used depending on the available specimen dimensions. Both mechanical and hydraulic load cells were used.

Through most of the experimental program the standard deposition substrate was graphite bar (of rectangular cross section) having dimensions 2.5 mm x 5.1 mm x 76 mm. Rod shaped samples deposited on 1.6 mm diameter graphite filaments were also tested.

The coated graphite test specimen then becomes a composite beam composed of a high modulus outer shell filled with a low modulus core.

The analysis of the flexure failure stress for such a beam can be made by mathematically converting the composite beam to a homogeneous beam made of any of the constituent materials comprising the original beam. Thus, when it is of interest to determine the strength of the coating

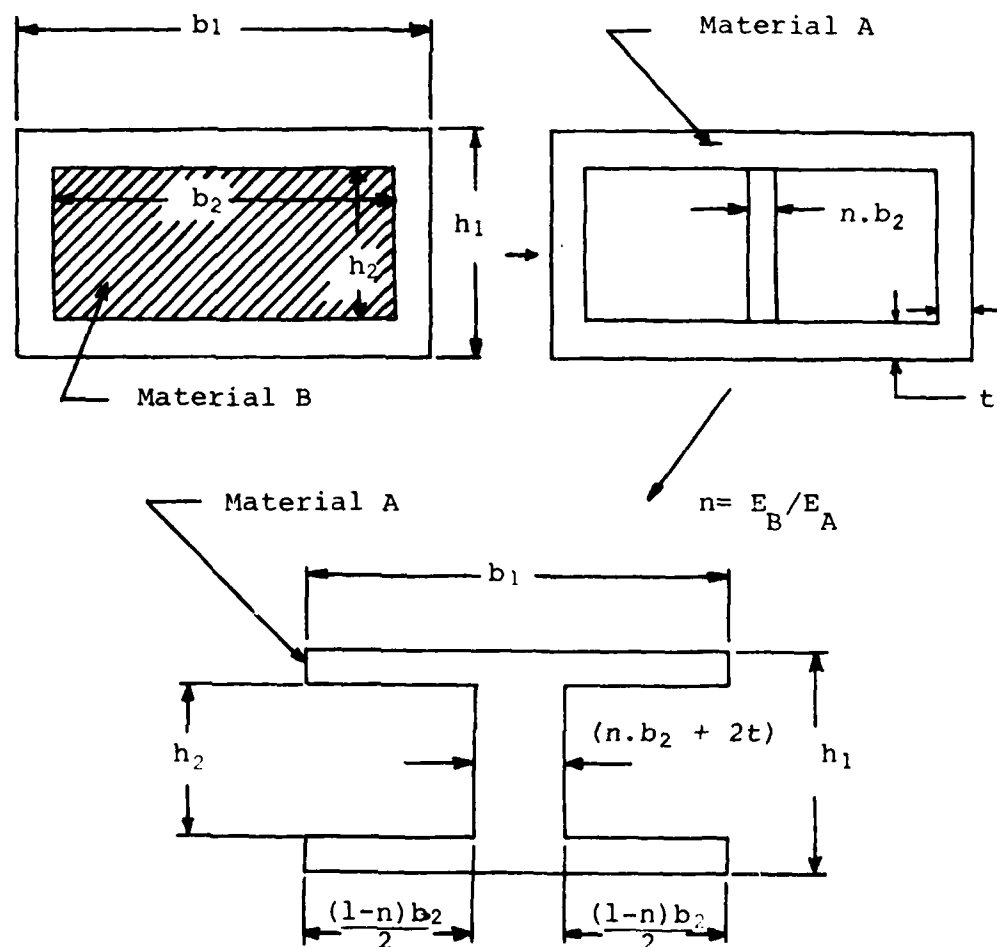
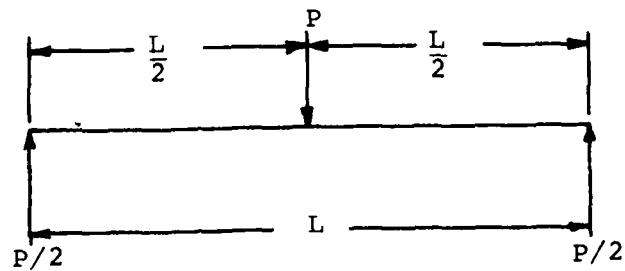
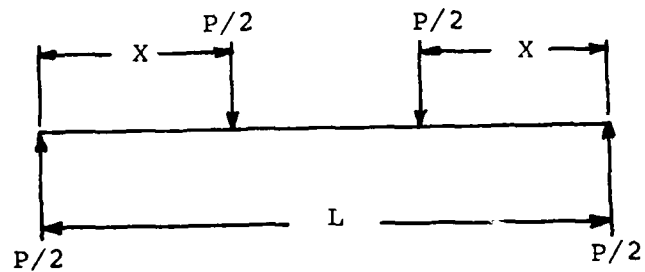


FIGURE 2: CALCULATION OF FLEXURE STRENGTH OF COMPOSITE BEAM BY THE METHOD OF EQUIVALENT SECTION.



(a) 3-point flexure



$$X = L/3 \text{ or } L/4$$

(b) 4-point flexure

FIGURE 3: LOADING CONFIGURATIONS IN FLEXURE TESTS.

of material A on a bar of material B, the composite beam is converted to a beam of material A by the method of equivalent sections ⁽³⁾. In this method, the cross section of the substrate (B) is replaced by an equivalent section of the coating such that at a given magnitude of axial strain, the forces developed in the substrate and the equivalent section of the coating are equal. Then the entire section can be treated as a single homogeneous material. The equivalent section is generated by changing the dimension of the substrate in the direction parallel to the neutral plane.

For a given axial strain e , the force developed on the substrate is $F_s = e.E_s.A_s$. At the same point in the coating, the force is $F_c = e.E_c.A_c$. For $F_s = F_c$, we have $E_c.A_c = E_s.A_s = nE_cA_s$ where $n = E_s/E_c$. Thus the area of cross section of the coating to replace an equivalent area of the substrate is $n.A_s$.

For a bend bar of rectangular cross section as shown in Figure 2 the area of the substrate ($A_s = b_2.h_2$) is transformed into an equivalent area of the coating by changing b_2 to $n.b_2$. Then, the moment of inertia of the equivalent cross section which becomes an "I" beam, is given by

$$I = \frac{b_1 h_1^3 - (1-n) b_2 h_2^3}{12}$$

Then, for a three point flexure (center-point loading) test (Figure 3)

$$TRS = \frac{3PLh_1}{2\{b_1 h_1^3 - (1-n) b_2 h_2^3\}}$$

It is assumed in the above equation that the failure occurs in the center of the span. When the failure occurs elsewhere, the flexure formula is modified to

$$TRS = \frac{3Ph_1 (L-2x)}{2\{b_1h_1^3 - (1-n) b_2h_2^3\}}$$

where x is the distance between the central loading pin and the point of fracture, the expression for the four-point flexure test is

$$TRS \text{ (4-point)} = \frac{3Pah_1}{b_1h_1^3 - (1-n) b_2h_2^3}$$

where a can be L/3 (1/3 - four point) or L/4 (1/4 - four point), as shown in Figure 3.

II-B.2 X-Ray Diffraction

Phase identification was performed on a G.E. XRD-5 diffractometer using Ni filtered copper K α radiation. A diverting slit of 3 $^\circ$ and a medium resolution Soller slit with a 0.2 $^\circ$ scatter slit were used. Surface preparation was typically not a problem. As-deposited surfaces usually yielded adequate spectra. Coarsely faceted specimens were subjected to light grinding to obtain a relatively smooth, flat surface.

II-B.3 Scanning Electron Microscopy (SEM) and Energy Dispersive Analysis of X-Rays (EDAX)

San Fernando Laboratories has an AMR model 1200A scanning

electron microscope and has access to a Cambridge Stereo-Scan Model S4-10 instrument at the University of Southern California. SEM investigations were usually limited to unetched, as-deposited surfaces and unetched fracture surfaces. A gold/palladium layer ($\sim 200 \text{ \AA}$) was sputtered onto the specimens to provide a conductive surface.

EDAX analysis of qualitative and semiquantitative chemical composition was performed on a Tracor Northern EDAX system attached to the Cambridge SEM.

II-B.4 Microprobe Analysis

In addition to EDAX, we obtained chemical composition information through microprobe analysis, which was supplied by Scanning Electron Analysis Laboratory (SEAL) of Los Angeles. SEAL uses an ETEC Model R1 SEM, equipped with an Autoscan Crystal Spectrometer.

II-B.5 Microhardness and Fracture Toughness

These properties were determined with the aid of a Leitz Miniload Microhardness tester using a Vickers diamond indenter. Hardness was measured at loads ranging from 100 to 500 g. A few fracture toughness values were calculated from the measurement of the length of cracks generated by indentation. This technique is described by Evans and Charles.⁴

SECTION III

SIC INVESTIGATION - RESULTS AND DISCUSSIONS

III-A First Year's Efforts

The silicon carbide program of preceding years⁵ produced material having very high strengths, of the order of 2070 MPa (300 ksi) at 1300° to 1400°C.⁶ Figures 4 and 5 show two different TEM micrographs which illustrate the grain structure of this material. These micrographs were supplied by S. Dutta of NASA Lewis Research Center, Cleveland, Ohio.

The micrographs demonstrate the fine-grained structure of the CNTD SiC. The longest crystallite dimension apparent in Figure 4 is about 60 nm or 600 Å; the shortest about 10 nm or 100 Å. A homogeneous microstructure with such a small grain size is quite remarkable and undoubtedly responsible for the extraordinary strength of the material. (Fine structure apparent within individual crystallites is an artifact caused by overlapping crystallites, a Moire pattern⁷).

These results encouraged attempts to translate the process from the internal resistance heating method into the potentially more useful furnace heating method.

Three experimental efforts were conducted during the first year of the contract in support of CNTD silicon carbide research.

1. An initial attempt was made to translate the CNTD SiC process from the method of internal resistance heating



FIGURE 4: SCANNING TRANSMISSION ELECTRON MICROGRAPH
OF CNTD SiC DEPOSIT SHOWING THE EXTREMELY
FINE-GRAINED MICROSTRUCTURE; 200,000X.
(COURTESY OF DR. SUNIL DUTTA, NASA LEWIS
RESEARCH CENTER, CLEVELAND, OHIO).

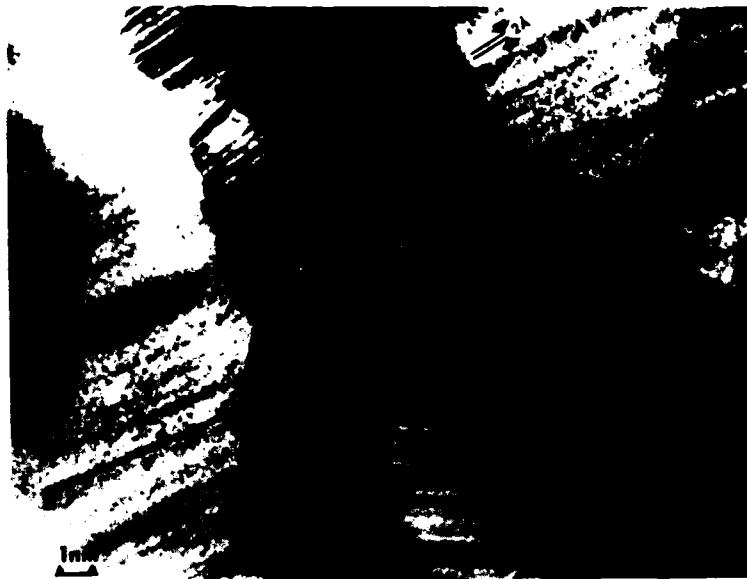


FIGURE 5: SCANNING TRANSMISSION ELECTRON MICROGRAPH OF CNTD SiC; 1,000,000X. THE FINE STRUCTURE WITHIN THE VARIOUS GRAINS APPEARS TO BE MOIRE FRINGES. (COURTESY OF DR. SUNIL DUTTA, NASA LEWIS RESEARCH CENTER, CLEVELAND, OHIO).

into a more useful method of furnace heating. We used methyltrichlorosilane as the precursor for SiC.

2. In parallel with these first attempts at a furnace process, we conducted a series of experiments using a fundamentally different deposition chemistry than that previously used. In these experiments we explored the utility of a furnace deposition technique based on silicon chloride disproportionation chemistry.

When the two efforts above using the furnace process did not succeed in producing CNTD SiC on graphite, we repeated the resistance technique using graphite rods. This last effort succeeded in once more producing strong CNTD material and, in so doing, provided some valuable insight into the importance of the gas temperature to the CNTD SiC process.

III-A.1. Furnace Process Attempts

The initial silicon carbide furnace investigation was carried out using the methyltrichlorosilane (MTS)/H₂ chemical system. The operating parameters were held within the following ranges:

Total chamber pressure:	250-350 torr.
MTS:	500-800 cc/min.
Hydrogen:	300-2500 cc/min.
H ₂ /MTS:	0.5-3.0
argon:	1430-4145 cc/min.

Gas preheat temperature : 650-690°C

Substrate temperature : 1050-1125°C

A total of 21 runs were conducted using the conventional furnace design shown in Figure 6. TABLE A-1 (APPENDIX) lists deposition conditions for these runs.

These initial experiments consisted of depositing SiC on UT-22 (Ultra Carbon Corp.) graphite substrate bars (2.5 mm x 5.1 mm x 89 mm) in a furnace. The furnace set-up illustrated in Figure 6 consists of an inductively heated graphite tube surrounded by a quartz chamber. A clam shell heater was used to control the preheat temperature of the gas stream which was monitored with a thermocouple located 127 mm above the furnace cap. The temperature of the furnace was monitored with an optical (disappearing filament) pyrometer. Argon, hydrogen and methyltrichlorosilane (MTS) were introduced through an injector located at the top of the furnace.

Deposition rates of 0.13 mm - 9.18 mm/hr. were achieved. Table 1 presents some properties of deposits made in the furnace. There was a wide scatter in the hardness values with results ranging from 1900 to 4600 VHN. Strength values also varied significantly, ranging from 95 MPa (14 ksi) to 635 MPa (92 ksi) in room temperature tests.

Figure 7 shows fractographs of two typical specimens of SiC deposited in a furnace using MTS/H₂ system. Figure 7b illustrates a fracture surface of SiC material with the columnar growth habit commonly observed in CVD work. Here

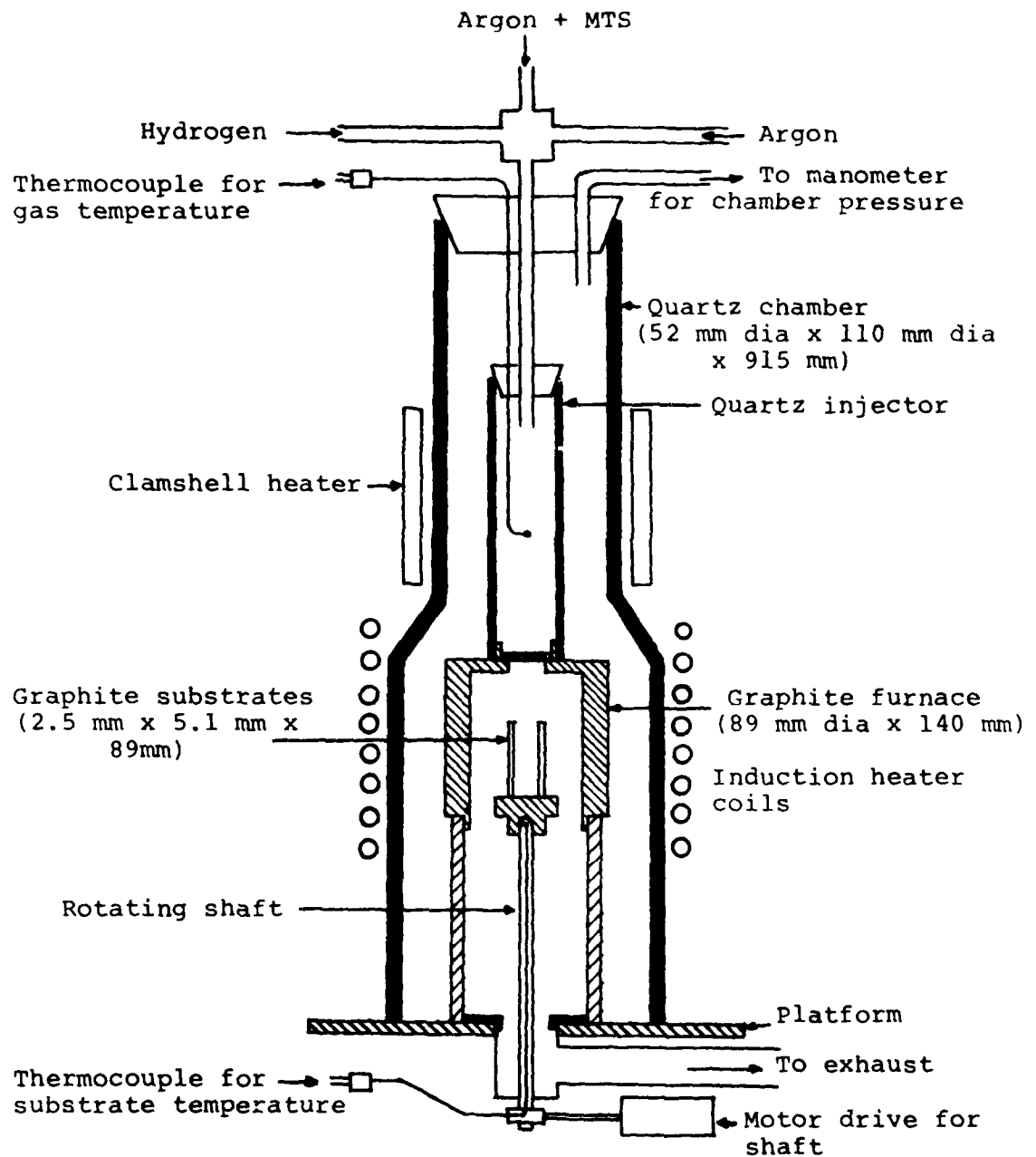


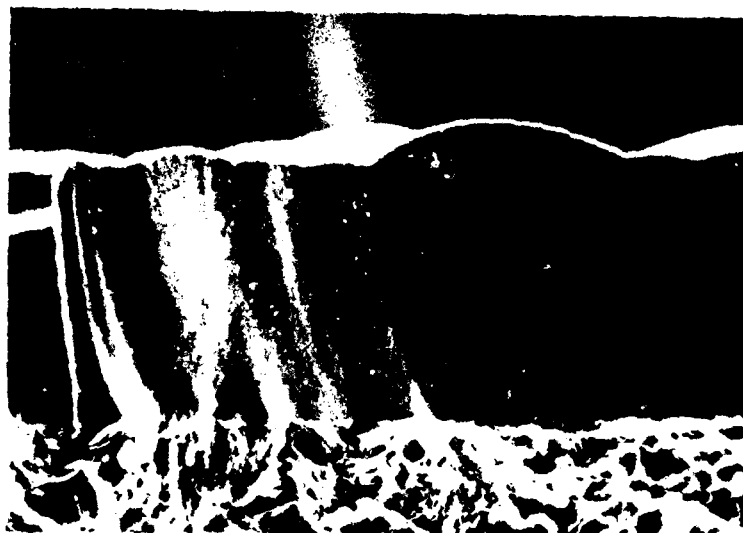
FIGURE 6: SCHEMATIC OF SiC DEPOSITION APPARATUS
SHOWING RADIANT (FURNACE) HEATING
ARRANGEMENT.

TABLE 1
PROPERTIES OF SILICON CARBIDE DEPOSITED
IN A CONVENTIONAL FURNACE

RUN NO.	SUBSTRATE	H ₂ /MTS	VICKERS HARDNESS	ROOM TEMPERATURE Flexure Strength	
				MPa	ksi
540	UT-22	0.5	-	269	39
561	UT-22	0.5	1920*	186 & 159	27 & 23
562	UT-22	0.5	2900	490 & 448	71 & 65
564	UT-22	0.5	3200	634	92
566	UT-22	0.5	4230	620	90
662	UT-22	3.0	3600	123	18
663	UT-22	3.0	-	>97	>14
664	UT-22	3.0	3300	123	18

*as measured with a 200 gram weight, all other samples were measured with a
500 gram weight.

(A)



(B)



FIGURE 7:

FRACTOGRAPHS OF SiC DEPOSITED IN A FURNACE.

(A) PHOTOGRAPH SHOWING "CONICAL SUPER-
STRUCTURE"; 400X

(B) PHOTOGRAPH SHOWING COLUMNAR CRYSTAL
HABIT; 400X

roughly columnar grain boundaries separate relatively large (~100 μ m) single crystal grains. Figure 7a, however, shows quite a different crystal growth habit which appeared during the furnace experiments. Roy Rice of the Naval Research Laboratory in Washington, D.C. first brought this "conical" growth pattern to our attention.⁸ After characterizing several coated graphite specimens of our furnace deposited SiC, he attributed the relatively low bend strength (~345 MPa average bend strength) to the presence of this conical structure. Just as shown in Figure 7a, fracture surfaces were delineated by these conical structures, and a rough correlation was found between the size of these growth cones and measured bend strength. Measured fracture energy was also low (~7 J/m²) compared to other SiC materials (~20-30 J/m²), and contrary to expectations, showed a rough proportional correlation with flaw sizes observed on bend test failures. Rice noted that these observations might point to effects caused by residual stresses.

This conical growth phenomenon was further examined at SFL. High magnification SEM micrographs of coating surface topography revealed that the top surface of each cone appeared to consist of very fine grains of about 0.2-0.3 μ m. The growth cones thus appeared to be a "super-structure" of associated fine crystallites.

A conical "super-structure" of small crystallites is a well known phenomenon in the vapor deposition of pyrolytic

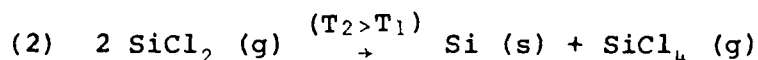
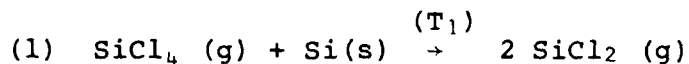
carbon^{9,10}. When conditions are suitable, the balance between the surface nucleation rate and the crystal growth rate can become dominated by surface nucleation. Such deposition produces fine oriented crystallites (~200 to 300 Å equiaxed) which grow upon one another, to reproduce a conical super-structure about substrate surface asperities.

A similar phenomenon has been seen before in CVD SiC and has been related to high deposition rates and to high (super-saturated) active gas concentrations¹¹. Rice's observation that residual stresses might explain some of his results is supported by the earlier work which shows the conical super-structure to be closely associated with residual stresses⁹.

The major difference in the two sample runs shown in Figure 7 was that the former was deposited at the H₂/MTS ratio of 0.5, while the latter was run at the ratio of 3.

III-A.2 SiCl₂ Disproportionation

While the initial attempts to develop a CNTD SiC furnace process were in progress, we conducted a parallel effort to test a fundamentally different deposition chemistry. This effort was undertaken by analogy to another CNTD material, CNTD TiB₂. CNTD TiB₂ is deposited from a partially reduced titanium chloride and BCl₃. The analogous method for SiC involves a reaction of SiCl₂ with a carbon compound such as methane. This SiCl₂ is produced in-situ by the partial reduction of SiCl₄ with elemental silicon.⁵ The reactions are:



The deposition parameters were held within the following ranges:

Total chamber pressure:	230-360 torr
SiCl ₄ :	300-500 cc/min.
argon:	500-1500 cc/min.
methane:	50-100 cc/min.
substrate temp:	885-1100°C

A total of 21 runs were conducted. Deposition rates of 0.05 - 0.13 mm/hr were observed. See Table A-1 for details of deposition conditions.

The silicon disproportionation experiments were carried out in a furnace using a graphite crucible as shown in Figure 8.

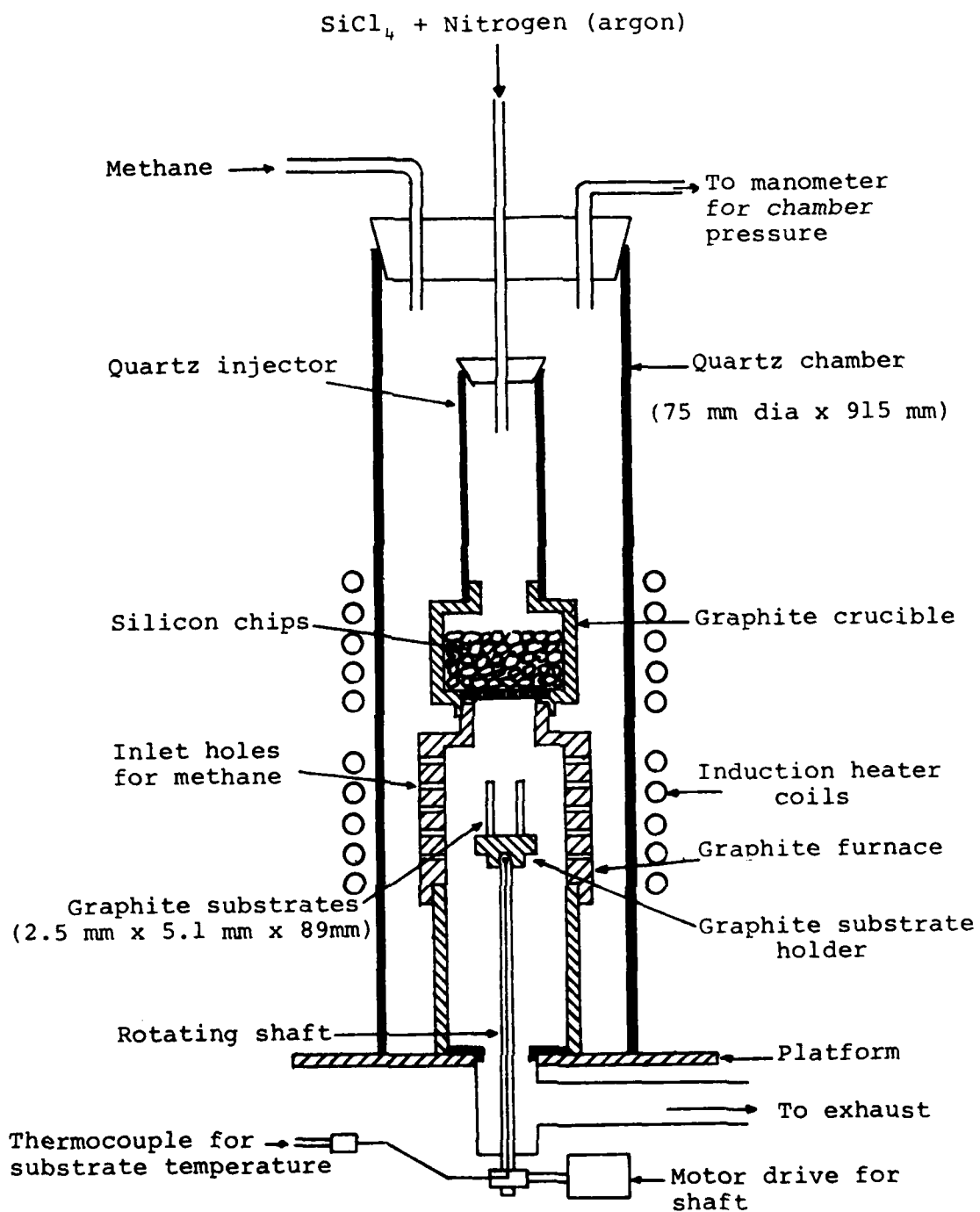


FIGURE 8: SCHEMATIC OF SiC DEPOSITION APPARATUS USING SILICON HALIDE DISPROPORTIONATION SCHEME.

SiCl_4 and a carrier gas were passed over hot semiconductor grade silicon chips in order to produce partially reduced chlorosilanes. Carbon was added to the reactant stream in the form of methane through holes located at the top of the graphite furnace.

The deposits varied from a loose, noncoherent, powdery material ranging in color from yellow to grey, to a few coherent deposits greyish in color. The coherent deposits resulted when the temperature difference between reaction (1) and (2) was 350° or greater. Table 2 provides test results on this material.

Vickers hardness of these samples was between 850 and 934 HV_{500} . Flexure strength was measured on one sample at 268 MPa (39 ksi). Typical values for elemental silicon are: Vickers hardness of 750 HV_{500} and flexure strength of 62 MPa (arc-cast 99.84% silicon)¹².

The addition of methane to the system (Table 2, runs #549 and 552) resulted in deposits characterized by hardness of 1062 and 1100 HV_{500} , and room temperature flexural strength of 352 MPa (51 ksi). Ratios of SiCl_4 /methane varied from 6.7 to 10.0. The addition of methane was not successful in making SiC.

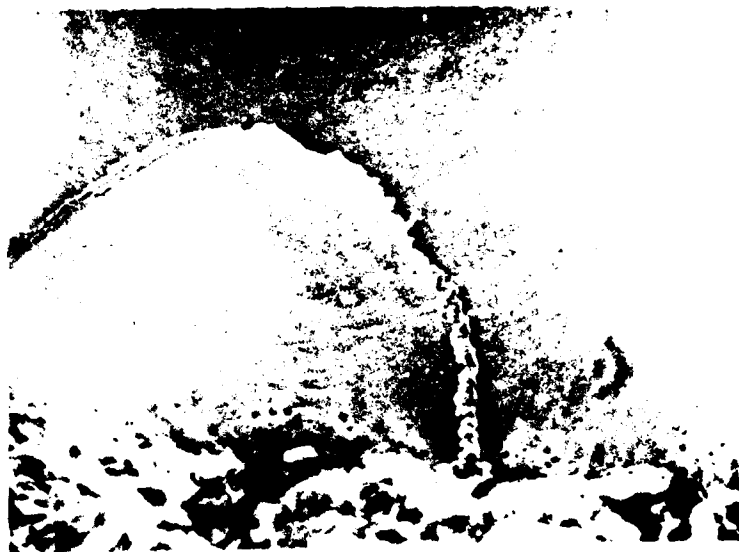
The specimens from the silicon disproportionation study showed considerable porosity on the fracture surface as shown in Figure 9. Figure 9a shows the material made without any carbon source. A string of voids near the substrate can be

TABLE 2 PROPERTIES OF SILICON DEPOSITED BY DISPROPORTIONATION

RUN NO.	SUBSTRATE	$\text{SiCl}_4/\text{CH}_4$	VICKERS HARDNESS	FLEXURE STRENGTH MPa (ksi)
546	UT-22	-	850	269 (39)
549	UT-22	10.0	1100	-
552	UT-22	6.7	1062*	352 (51)
560	UT-22	-	934	-

* As measured with a 300 gram load; all other hardness values determined with a 500 gram load.

(A)



(B)

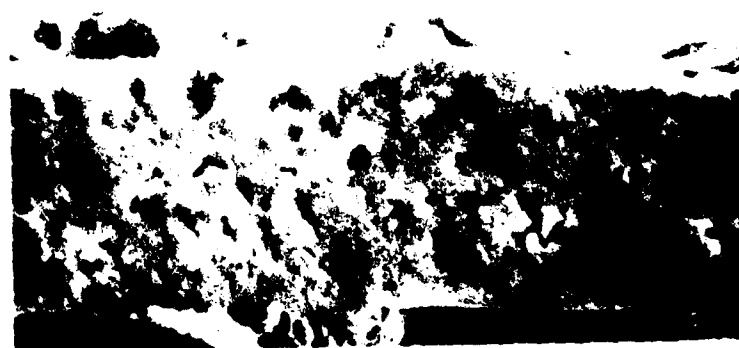


FIGURE 9:

FRACTOGRAPHS OF SILICON DEPOSITED IN THE
SILICON DISPROPORTIONATION SYSTEM.

(A) WITHOUT ADDITION OF METHANE; 500X

(B) WITH ADDITION OF METHANE; 1000X

seen. Porosity is also associated with the bead-like feature. XRD data showed that the material was mostly silicon with some traces of SiO_2 . The material of Figure 9b was made with $\text{SiCl}_4/\text{CH}_4 = 6.67$ and showed variation in color and composition along the length of the specimen. The bottom one-third of the deposit was tan colored and consisted mostly of SiO_2 with only traces of $\beta\text{-SiC}$. The rest of the samples were black in appearance, and showed mainly silicon and SiO_2 peaks on XRD scan. When the surface was polished and run again on a diffractometer, only silicon peaks were observed. This observation suggests that significant oxidation of the surface occurred during the run, and further indicates the presence of oxygen or water contamination.

We were surprised by the near absence of SiC in these deposits. Indications of possible contamination might offer an explanation. However, since the microstructure and resulting strength of the silicon deposits were so poor, we decided against further investigation. Instead, we decided to reproduce high strength SiC by internal resistance heating methods.

III-A.3 Deposition on Resistance Heated Graphite

Having encountered difficulty with furnace heated deposition methods, a series of experiments was conducted using resistance heated graphite rods in place of the tungsten filaments which were used as substrates in previous resistance work. By replacing the tungsten filaments (0.5 mm)

with graphite rods (~2 mm) we sought to accommodate critics who had questioned whether a relatively strong tungsten core might influence our flexural strength measurements. At the same time, we sought to increase the size of our specimens. These experiments once again produced strong CNTD material.

The third phase of the SiC work was accomplished using the experimental system shown in Figure 10. The main deposition chamber was a 75 mm dia. quartz tube. The graphite substrate (2 mm dia. x 152 mm long rod, UT-22) was resistively heated using a current of about 30-40 amps at 1-10 volts. During deposition the current was constantly adjusted to control the substrate temperature. Argon, hydrogen, silicon and carbon bearing gases were introduced, through an injector, at the top of the chamber. The mass flow rates of reactants were obtained by means of standard borosilicate glass rotameters. A clam shell heater was used to regulate the preheat temperature of the reactant stream, which was monitored by a thermocouple about 13 mm from the substrate. The substrate temperature was again measured with a pyrometer. In all, a total of 44 runs were accomplished. Deposition conditions are given in Table A-1, Appendix A. HLM graphite substrates were used in the initial work until a suitable graphite substrate with a closer match of coefficient of thermal expansion (CTE) was available.

We expected that the mismatch of thermal expansion characteristics between the HLM and the SiC coating would

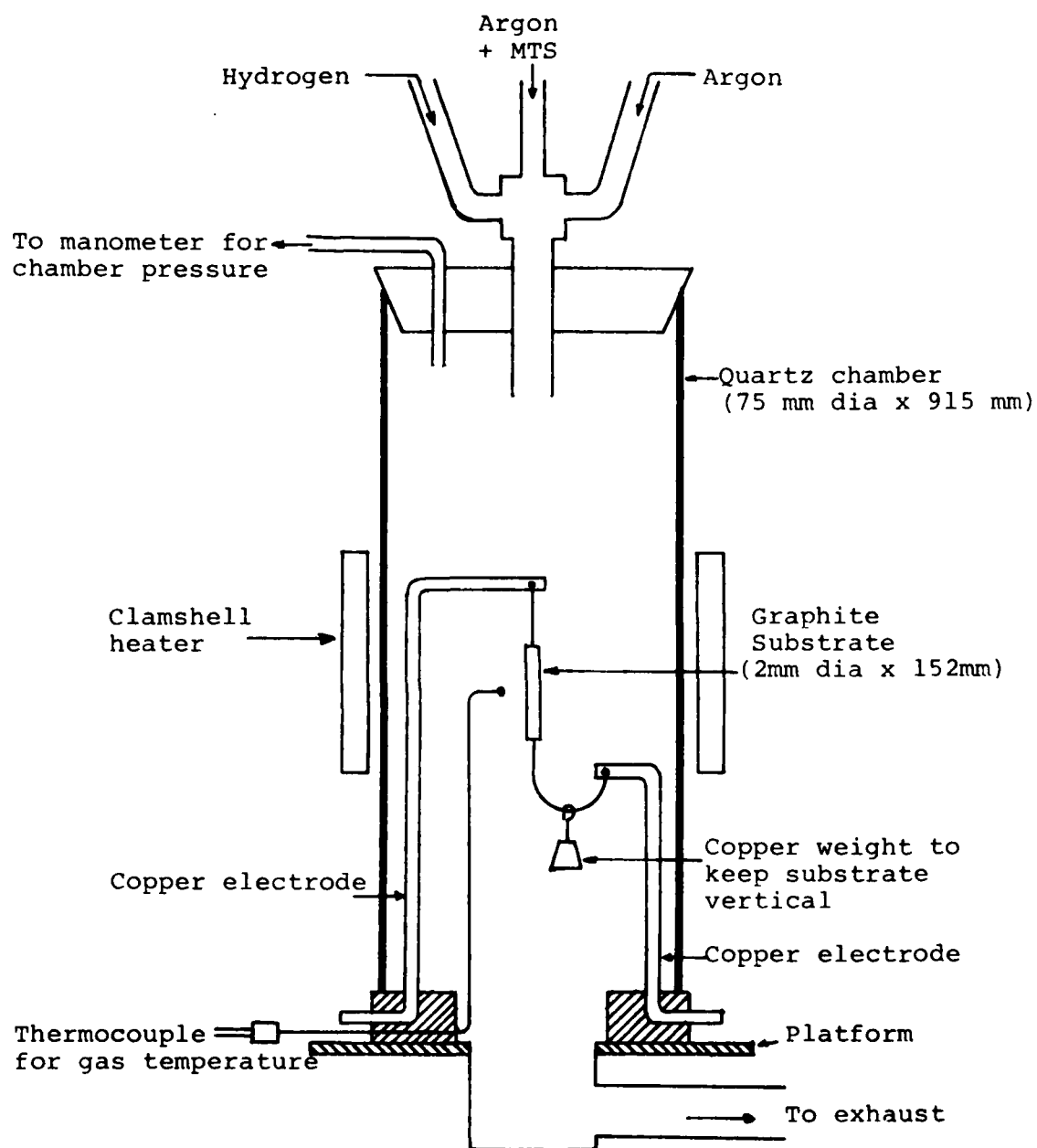


FIGURE 10: SCHEMATIC OF SiC DEPOSITION APPARATUS
SHOWING RESISTANCE HEATING ARRANGEMENT.

induce a room temperature tensile stress of about 1000 MPa (145 ksi) and in the SiC deposited at 1100 to 1200°C.

This series of runs was conducted using the following operating parameters:

Total chamber pressure:	230 torr
MTS:	250 cc/min
Hydrogen:	3375 cc/min
Argon:	1000 cc/min
Gas preheat temperature:	555-880
Substrate temperature:	1115-1200°C

The above run conditions were modeled after the early SiC work on tungsten filaments. Deposition rates varied from 0.13 mm to 0.43 mm/hr.

Fracture cross sections of these deposits were glassy in appearance without visual indications (to 120X magnification) of conical growth boundaries. Table 3 (runs #670 to 677) gives the results. Hardness values varied from 1100-1800 HV₅₀₀. These low values indicate the presence of free silicon, which was verified by XRD. Four point flexure strengths varied from 170 MPa to 421 MPa (25 to 61 ksi). These low values were expected in view of the large residual tensile stress present.

The addition of propane to the system in conjunction with altering the hydrogen/MTS ratio (Table 3, runs #679-682) succeeded in raising the hardness of the material to the range 2500-4190 HV₅₀₀. It seems apparent that the

TABLE 3 SILICON CARBIDE DEPOSITED ON RESISTIVELY HEATED SUBSTRATES

Run No.	SUBSTRATE	H ₂ / MTS	H ₂ / METHANE	H ₂ / PROPANE	MTS / METHANE	MTS / PROPANE	DEPOSIT THICKNESS microns	VICKERS HARDNESS	ROOM TEMPERATURE FLEXURE STRENGTH MPa	ROOM TEMPERATURE FLEXURE STRENGTH (ksi)
670	HLM	13.5	-	-	-	-	-	1566	172	(25)
671	HLM	13.5	-	-	-	-	152	1480	193	(28)
672	HLM	13.5	-	-	-	-	-	1100	193	(28)
673	HLM	13.5	-	-	-	-	-	1100	241	(35)
674	HLM	13.5	-	-	-	-	229	1100	421	(61)
675	HLM	13.5	-	-	-	-	203	1400	-	-
676a	HLM	6.7	-	-	-	-	-	1504	-	-
677	HLM	6.7	-	-	-	-	229	1800	200	(29)
678	HLM	6.7	-	-	-	-	152	1480	421	(61)
679	HLM	6.7	-	42.0	-	6.25	203	2500	345	(50)
680	HLM	13.5	-	84.4	-	6.25	152	2150	331	(48)
681	HLM	13.5	-	42.0	-	3.12	229	4190	462	(67)
682	HLM	18.0	-	56.2	-	3.12	203	3700	359	(52)
683	SP-2020	13.5	-	56.2	-	4.17	838	2350	586	(85)
684	SP-2020	15.0	-	62.5	-	4.17	784	2750	1310	(190)
685	SP-2020	15.0	-	62.5	-	4.17	1067	1900	1366	(198)
686	SP-2020	15.0	-	62.5	-	4.17	1651	-	966	(140)
687	SP-2020	15.0	-	62.5	-	4.17	1321	2040	745	(108)
688	SP-2020	15.0	-	62.5	-	4.17	1092	-	676	(98)
690	UT-22	15.0	13.9	-	.93	-	965	1300	614	(89)
691	UT-22	15.0	10.4	-	.69	-	1524	1400	431	(62)
692	UT-22	15.0	6.8	-	.45	-	1549	2038	662	(96)
695	UT-22	15.0	3.8	-	.25	-	1829	2500	1428	(207)
696	UT-22	15.0	5.4	-	.36	-	1930	2475	1317	(191)
697	UT-22	15.0	6.8	-	.45	-	1651	-	614	(89)
699	UT-22	15.0	8.3	-	.56	-	-	2500	676	(98)
701	UT-22	-	-	VARIABLE	-	-	-	2200	-	-
702	UT-22	15.0	195.3	62.5	13.00	4.17	-	2000	897	(130)
703	UT-22	15.0	195.3	62.5	13.00	4.17	1600	-	276	(40)
704	UT-22	-	-	VARIABLE	-	-	76	3000	-	-
705	UT-22	15.0	-	-	-	-	-	1420	514	(75)
707	SP-2020	15.0	-	-	-	-	-	1250	276	(40)
708	SP-2020	15.0	-	-	-	-	-	-	69	(10)

TABLE 3 SILICON CARBIDE DEPOSITED ON RESISTIVELY HEATED SUBSTRATES

Run No.	SUBSTRATE	H ₂ / MTS	H ₂ / METHANE	H ₂ / PROPANE	MTS/ METHANE	MTS/ PROPANE	DEPOSIT THICKNESS microns	VICKERS HARDNESS	ROOM TEMPERATURE FLEXURE STRENGTH MPa (ksi)
709	SP-2020	15.0	-	112.5	-	7.50	737	2800	138 (20)
710	SP-2020	15.0	-	-	-	-	-	1090	159 (23)
711	SP-2020	18.0	-	-	-	-	-	1500	117 (17)
712	SP-2020	15.0	-	62.5	-	4.17	-	2800	303 (44)
									400 (58)

carbon provided through the addition of propane reacts with the excess silicon thereby producing harder material. Deposition rates of 0.25 to 0.40 mm/hr were achieved.

The acquisition of graphite substrate, Stackpole 2020 which was more thermally compatible with SiC at elevated temperature (CTE of Stackpole 2020: $4 \times 10^{-6}/^{\circ}\text{C}$) enabled accurate strength measurements to be performed. The results of runs #683 to 688 in Table 3 show strength values of 585-1365 MPa (85-198 ksi). The hardness varied from 1900 to 2750 HV₅₀₀.

In an effort to examine alternative carbon sources, methane was used instead of propane (runs #690-699, Table 3). During this series of experiments operating parameters were maintained as listed below:

Total chamber pressure:	230 torr
MTS:	250 cc/min
Hydrogen:	3750 cc/min
Argon:	1000 cc/min
Methane:	360-1000 cc/min
Gas preheat temperature:	-800-900 ^o C
Substrate temperature:	1230-1260 ^o C

The deposits were characterized for hardness and room temperature flexural strength. The hardness varied from 1300-2500 HV₅₀₀ and the strength varied from 430 to 1430 MPa (62 to 207 ksi). The gas preheat temperature was shown to be a critical factor affecting the resultant material:

temperature above 850°C produced material with strength greater than 690 MPa (100 ksi). The deposition occurred at a rate of 0.25 mm to 0.58 mm per hour.

We expected that the addition of another carbon source (e.g. methane or propane) would result in a more complete carburization of silicon and thereby yield a harder or stronger material. The samples made on resistance heated graphite substrates were evaluated fairly extensively. These materials did not show any conical super-structure in the fractographs. In most cases a fine grained deposit was obtained, although strength varied over a wide range. The fractographs of the two samples from a set are shown in Figure 11. Figure 11a shows the sample made with $(\text{MTS}/\text{C}_3\text{H}_8) = 6.25$. A band of porosity is clearly visible. A decrease in the $\text{MTS}/\text{C}_3\text{H}_8$ ratio resulted in the elimination of porosity and an increase in hardness (see Figure 11b).

A better control and optimization of $\text{H}_2/\text{C}_3\text{H}_8$ and $\text{MTS}/\text{C}_3\text{H}_8$ ratios resulted in a better microstructure and higher strengths. Figure 12a shows the fractograph of a sample with a strength of 1366 MPa (198 ksi) and Figure 12b shows the etched cross section (5% CrO_3 with 10% HF, electrolytic at 70 °C and 5 volts). The finely banded structure of CNTD SiC is clearly visible. These samples showed low hardness values in the range of 1400-3000 HV_{500} . EDAX measurements revealed a wide range of elemental composition, with excess silicon in most specimens.

(A)



(B)

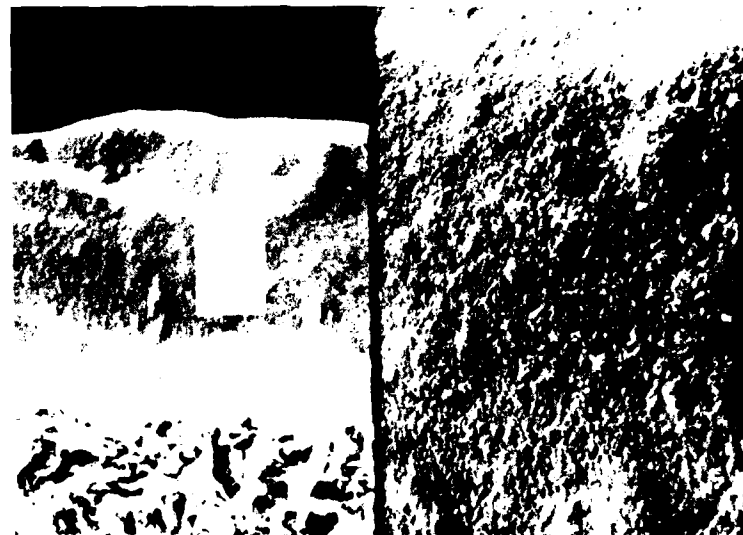


FIGURE 11: FRACTOGRAPHS OF SiC DEPOSITED ON
RESISTIVELY HEATED GRAPHITE SUBSTRATE
USING PROPANE AND MTS.

(A) PHOTOGRAPH SHOWING A LINE OF POROSITY,
 $\text{MTS}/\text{C}_3\text{H}_8 = 6.25$; 500X

(B) PHOTOGRAPH SHOWING THE FINE STRUCTURE
OF DEPOSIT, $\text{MTS}/\text{C}_3\text{H}_8 = 3.12$;
LEFT: 200X, RIGHT: 3000X

(A)



(B)

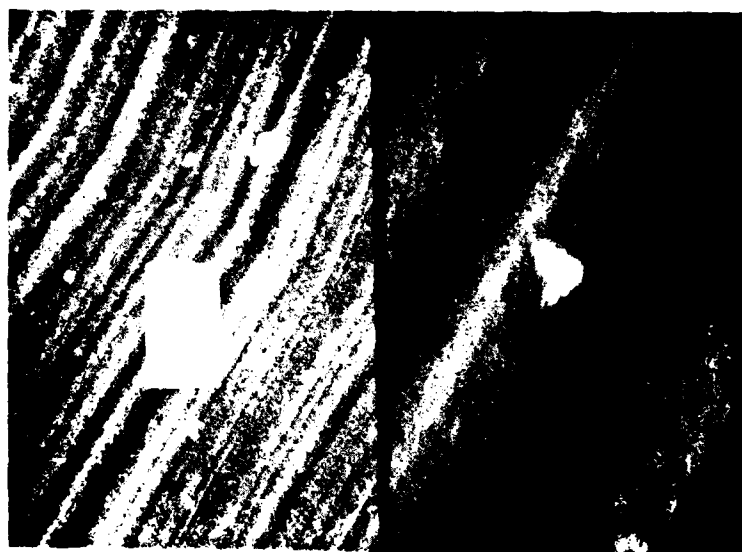


FIGURE 12:

STRUCTURE OF CNTD SiC

(A) FRACTOGRAPH OF HIGH STRENGTH SiC
DEPOSIT; 50X

(B) ETCHED CROSS-SECTION SHOWING FINELY
BANDED MICROSTRUCTURE;
LEFT: 2000X, RIGHT: 10,000X

We attempted to use the EDAX data to examine the relationship between the material's hardness and its silicon content. However, since the EDAX method cannot detect elements lighter than sodium, the carbon content of the specimens had to be inferred. The EDAX measurements gave us a value for the silicon and chlorine concentration within the specimens, and we assumed the balance of material to be carbon. With one major constituent of the material determined by implication, our measurements were highly dependent on the EDAX calibration procedure and somewhat questionable. (We calibrated against an HP α -SiC specimen assumed to be stoichiometric SiC).

Figure 13 portrays the relationship between excess silicon and microhardness for these specimens, where

$$\text{Excess Si (wt\%)} = \text{Measured Si (wt\%)} - \text{Implied C (wt\%)} \times 2.33 .$$

The smooth trend in hardness vs. silicon content that is shown in Figure 13 indicates the close relation between the two properties.

Although Figure 13 suggests that the presence of excess carbon tends to increase the hardness of the deposit, we find such a result difficult to believe. It is known¹³ that carbon is completely insoluble in SiC. Thus, the increase in hardness with excess carbon cannot be explained on the basis of solute hardening due to dissolved carbon. At the same time, we would expect the presence of a second phase of excess carbon or silicon to decrease the hardness. Since

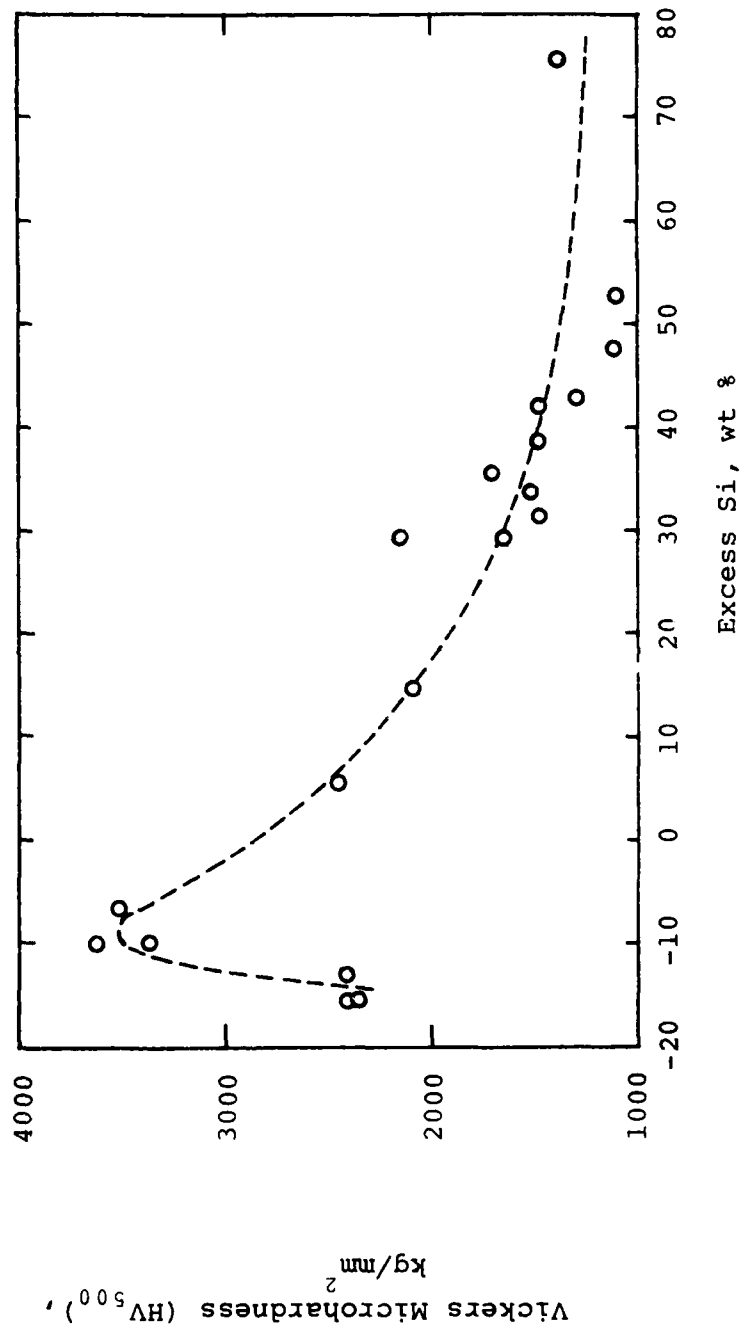


FIGURE 13: VARIATION OF HARDNESS OF CNTD SiC DEPOSITED ON RESISTANCE-HEATED GRAPHITE AS A FUNCTION OF SILICON CONTENT OF THE DEPOSIT.

our EDAX data might contain a systematic error, we believe that it is more likely that the hardness maximum is associated with the stoichiometric composition, and that Figure 13 therefore demonstrates the extent of systematic error involved in the elemental analysis by EDAX, where the concentration of light elements cannot be directly determined.

We could find no similar correlation between the composition and the flexural strength of the material. However, we did not consider our failure to find such a correlation too surprising since our strength measurements are inherently less accurate than measurements of microhardness, and the strength is much more sensitive to other factors, such as residual stress.

III-B Second Year's Effort

During the period of January, 1980 through January, 1981 our efforts were concentrated almost exclusively on the evaluation of SiC produced by a newly developed furnace process.

Near the end of the first year described above, we were actively engaged in another parallel effort under internal SFL sponsorship, which continued to explore the feasibility of a furnace process for CNTD SiC.

The internal R&D program was successful in February of 1980 and from that time until January of 1981, the AFOSR program described in this report was devoted entirely to producing test specimens and evaluating the SiC material

produced by the new furnace process.

III-B.1 Furnace Development

The development of San Fernando Laboratories furnace process for CNTD SiC began with the idea that previous attempts had failed because of an inability to control gas temperature within the furnace.

We attempted to solve the problem in two ways. First we tried to create an aerodynamic blanket of inert gas along the inner furnace wall in an attempt to provide an insulating layer between the active gases and the furnace wall. In this manner, we hoped to reduce heating of the active gases by conduction and convection from the furnace wall and still allow radiant heating of the part. Secondly, we tried to introduce cool diluent gas downstream from the intake end of the furnace and thereby keep the active gases from overheating as they passed through the furnace.

III-B.1a Slotted Top Furnace

Our first attempt took the form of the slotted top furnace shown in Figure 14. Figure 15 shows how the furnace was placed within the deposition chamber.

This design employed a top section which allowed inert nitrogen gas to be injected through three curved slots running nearly 360° around the outside area. Active gases would be injected throughout the center opening. We expected that the inert gas properly injected through these slots would form a laminar-flow aerodynamic blanket which would shield the

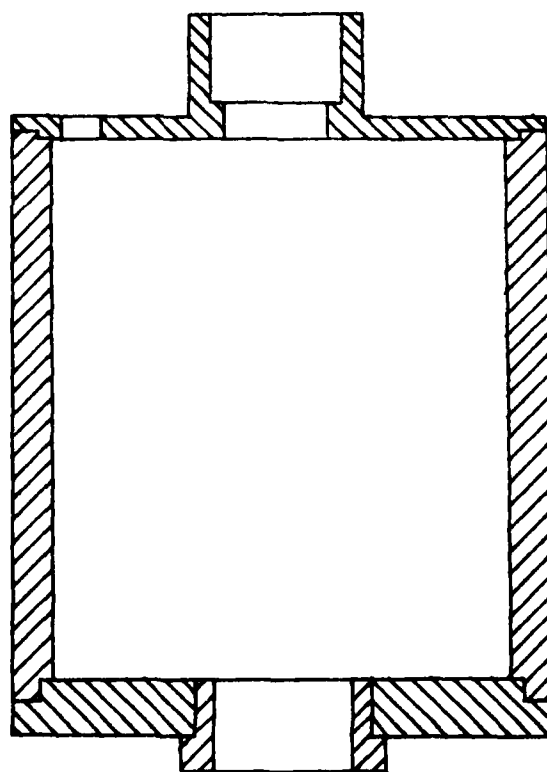
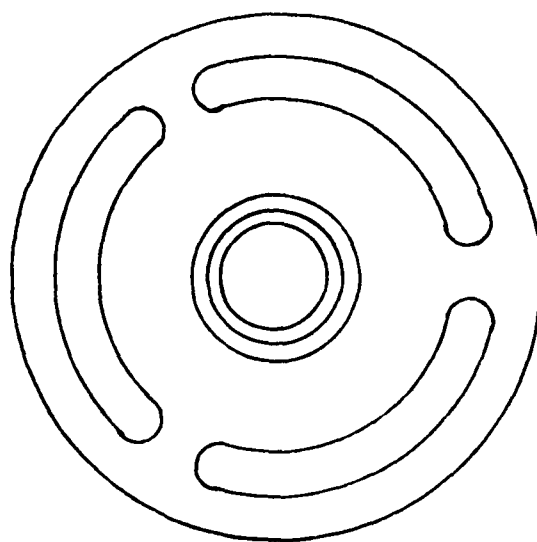


FIGURE 14: SCHEMATIC OF THE SLOTTED-TOP FURNACE DESIGN. THE TOP VIEW SHOWS THE ARRANGEMENT OF THE SLOTS.

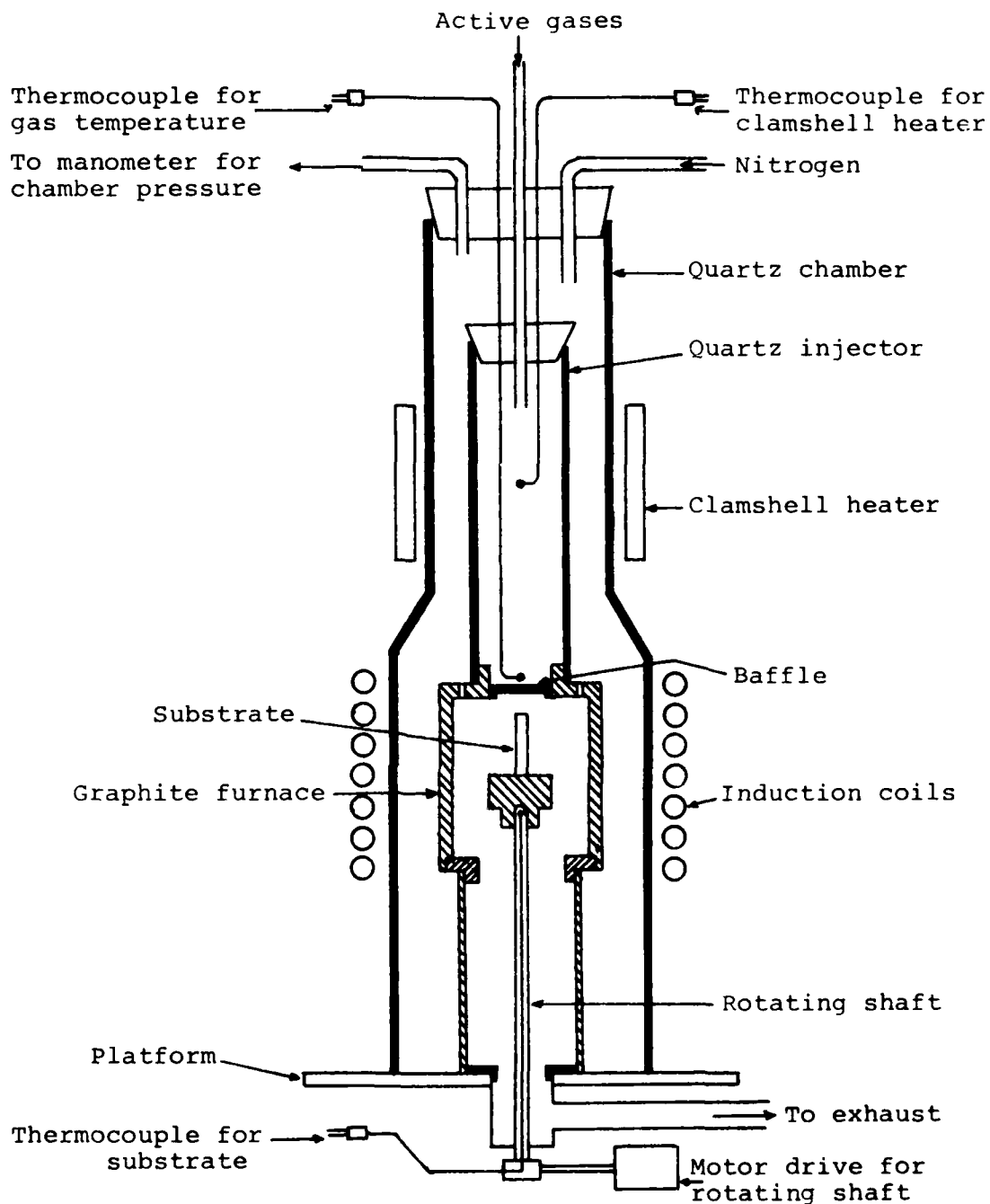


FIGURE 15: SCHEMATIC ARRANGEMENT OF THE DEPOSITION CHAMBER FOR SiC DEPOSITION USING THE SLOTTED-TOP FURNACE.

active gases from direct contact with the sidewall. We experienced both success and failure with this approach. The deposits formed in the slotted-top furnace were improved over previous furnace deposits. Fracture surfaces appeared similar to the strong material we had encountered with direct heating methods. No super-conical or columnar growth patterns were observed. Bend strengths of about 450 MPa typified these deposits with hardness values of about 2400.

We also, however, observed a large amount of SiC coating on the furnace walls, indicating that our hypothetical "aero-dynamic blanket" was not working very well.

These results did encourage us to try an improved design.

III-B.1b Slotted Wall Furnace

In the next design, we tried to accomplish our objectives by introducing N_2 through openings in the side of the furnace. We expected, in this way, to improve the cooling effect of nitrogen by introducing fresh gas downstream from the intake and also more effectively blanket the furnace walls.

Figure 16 illustrates this type of experimental furnace. Porous graphite felt was wrapped around the outside of the furnace to assure uniform nitrogen flow through the slots along the length of the furnace.

The material deposited in this furnace typically had a very good appearance by subjective examination of the fracture

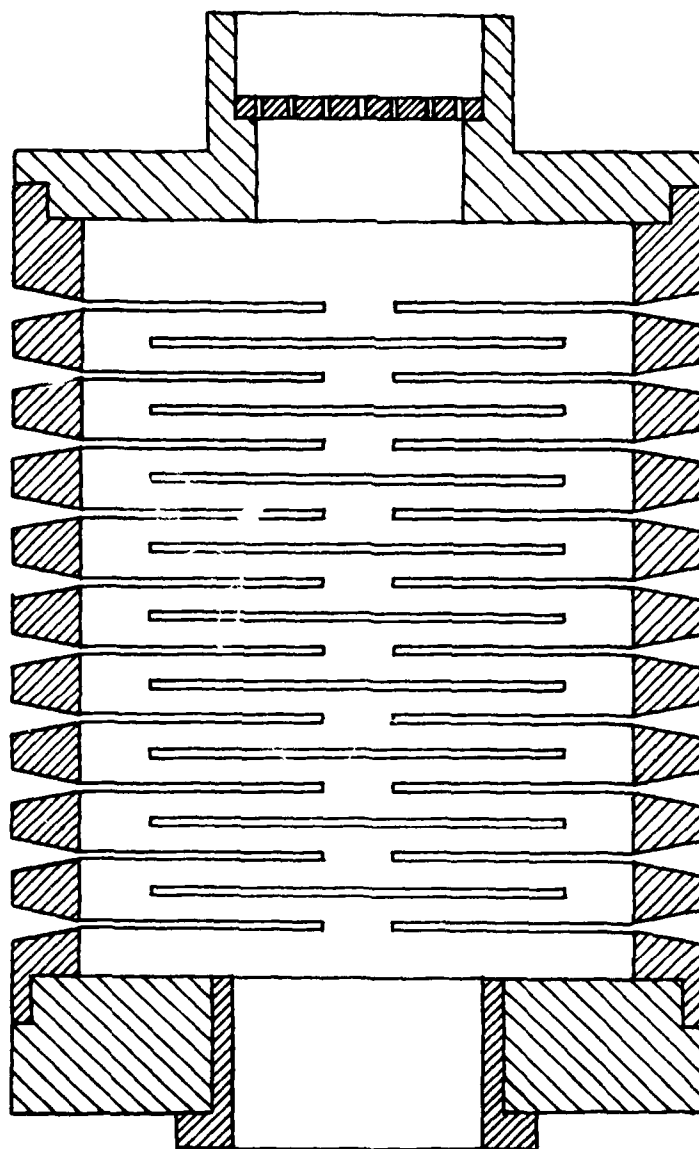


FIGURE 16: LONGITUDINAL SECTION OF THE
SLOTTED WALL GRAPHITE FURNACE
USED IN SiC DEPOSITION.

surfaces and had bend strengths in the range 725 to 825 MPa with hardness of about 2700 (HV₅₀₀).

We noticed that the walls of this furnace still plated heavily which plugged the slots after only two or three runs.

III-B.1c Flower Pot Furnace

Since the slotted-wall design had demonstrated some improvement, our third design represented a refinement of the same concept.

Figure 17 illustrates this design. We have labelled it the "Flower Pot Furnace," since it's constructed from a number of ring segments which fit together in a fashion similar to a stack of flower pots.

Two refinements over the slotted wall furnace are incorporated into the flower pot furnace. By using various sizes of spacers, the gaps between ring segments could be adjusted allowing some control over downstream injections. Also, ring segments were shaped to direct N₂ flow down along the inside wall of the furnace. (See Figure 17).

Results from this furnace seem to show that it achieved our objectives. Plating on the furnace wall was considerably reduced. More than twenty deposition runs were possible before SiC deposits on the furnace wall became troublesome.

The flower pot furnace has also produced the highest quality SiC material that we have ever made in a furnace. TRS values have ranged from 825 to 1372 MPa with hardness in the range 2700-3500 (HV₅₀₀).

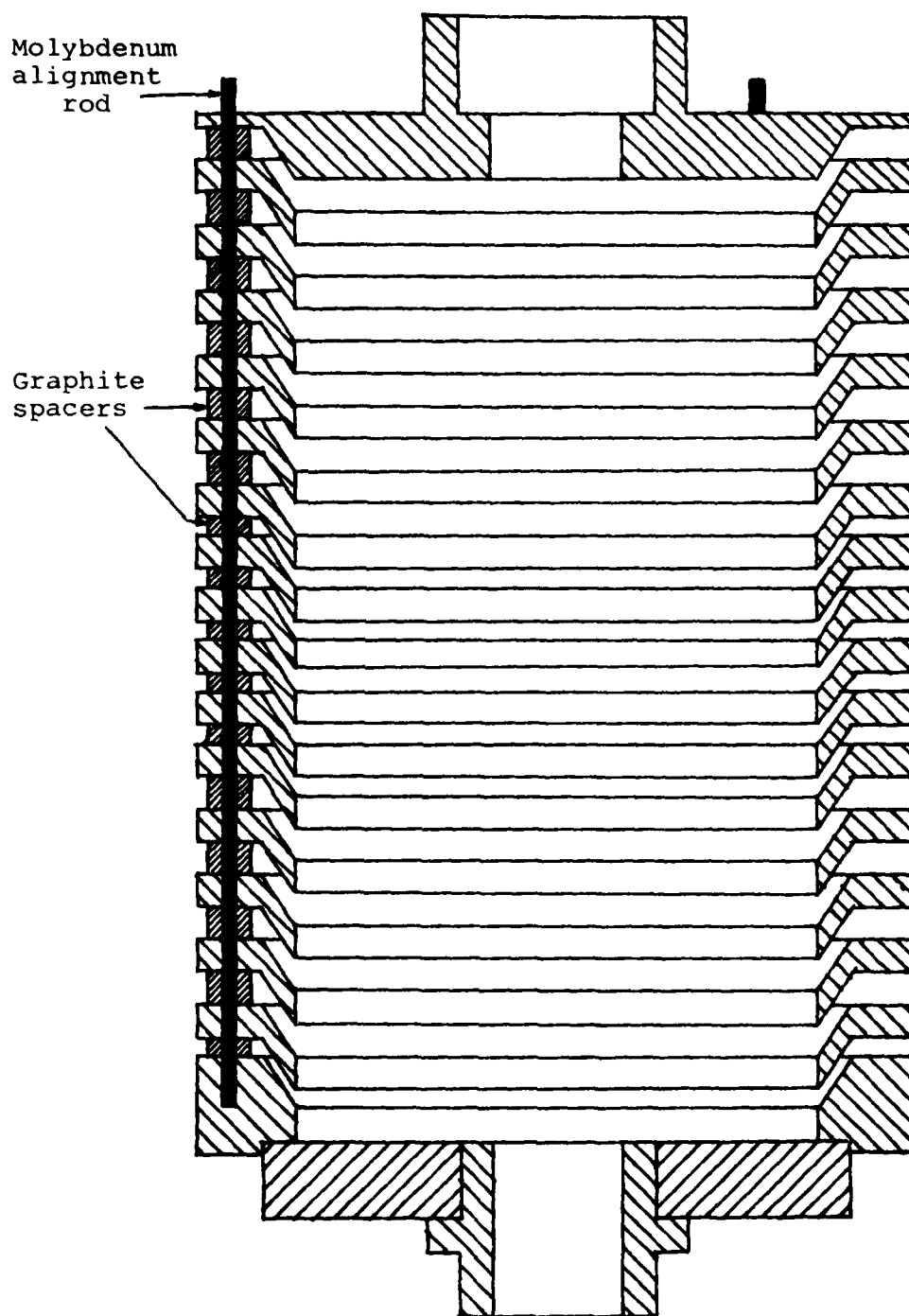


FIGURE 17: LONGITUDINAL CROSS-SECTION THROUGH THE "FLOWER-POT" FURNACE SHOWING THE ARRANGEMENT OF INDIVIDUAL SEGMENTS ALLOWING VARIABLE SPACING TO CONTROL THE GAS FLOW.

All of the SiC material characterized in the following sections was produced in a flower pot furnace similar to that shown in Figure 17.

III-B.2 Elevated Temperature Strength Testing

Table 4 presents data which were obtained from an elevated temperature testing carried out by Dr. J. Stiglich of San Fernando Laboratories. Bend bar specimens of graphite (2.5 mm x 5.0 mm x 76 mm) were coated with material in the flower pot furnace. (See Figure 17). Four-point bend tests were conducted under air atmosphere at elevated temperatures using a furnace designed by G. Quinn¹⁴ of AMMRC. Inside fixtures were made of HPSiC and the furnace was capable of a temperature up to 1500°C, heated by SiC "glow bar" resistance heaters. SiC extension rods penetrated the furnace walls and connected the furnace fixtures to the crosshead of an Instron universal test machine.

Figure 18 graphically displays the results. Room temperature data, which were obtained by three-point flexure, is shown adjusted by Weibull volume factor. Figures 19 through 21 display similar data obtained by IITRI¹⁵ for various SiC materials.

A comparison of Figure 18 with Figures 19 through 21 leads us to remark upon several important features.

We note that the CNTD SiC has relatively high strength; even better at high temperatures than the best bulk material available, Norton NC 203 HPSiC (See Figure 21). Also we note

TABLE 4: Flexure Strength Data for CNTD SiC

SPEC. #	MPa	ksi	Strain Rate
<u>3 pt. Flexure</u>			
1*	727.3	105.5	0.15 mm/min
2	728.4	105.6	0.15 mm/min
3	740.6	107.4	0.15 mm/min
4	781.2	113.3	0.15 mm/min
5	817.3	118.5	0.15 mm/min
6*	818.1	118.6	0.15 mm/min
7*	890.6	129.1	0.15 mm/min
8	894.7	129.7	0.15 mm/min
9	926.7	134.4	0.15 mm/min
10	1001.6	145.2	0.15 mm/min
11	1012.1	146.8	0.15 mm/min
12	1021.3	148.1	0.15 mm/min
13	1401.4	203.2	0.15 mm/min
14*	1073.8	155.7	0.15 mm/min
15	1097.4	159.1	0.15 mm/min
16*	799.4	115.9	0.15 mm/min
17*	1054.2	152.9	0.15 mm/min
<u>4 pt. Flexure 600°C</u>			
18*	470.6	68.2	0.5 mm/min
19	562.1	81.5	0.5 mm/min
20*	584.6	84.8	0.5 mm/min
21*	628.5	91.1	0.5 mm/min
22	643.7	93.3	0.5 mm/min
23*	645.7	93.6	0.5 mm/min
24	661.0	95.8	0.5 mm/min
25*	831.3	120.5	0.5 mm/min
<u>4 pt. Flexure 1000°C</u>			
26*	367.7	53.3	0.05 mm/min
27	417.9	60.6	0.5 mm/min
28	499.7	72.4	0.05 mm/min
29	537.3	77.9	0.05 mm/min

TABLE 4: Flexure Strength Data for CNTD SiC Continued

SPEC. #	MPa	ksi	Strain Rate
30	595.3	86.3	0.5 mm/min
31*	609.0	88.3	0.5 mm/min
32*	716.2	103.8	0.5 mm/min
33	748.8	108.6	0.05 mm/min
34*	783.2	113.6	0.5 mm/min
35*	887.4	128.7	0.05 mm/min
36	937.5	135.9	0.05 mm/min
<u>4 pt. Flexure 1200°C</u>			
37	533.5	77.4	0.5 mm/min
38	571.8	82.9	0.5 mm/min
39*	580.6	84.2	0.05 mm/min
40*	605.8	87.8	0.05 mm/min
41	615.7	89.3	0.05 mm/min
42	737.8	107.0	0.05 mm/min
43*	754.5	109.4	0.05 mm/min
44	797.7	115.7	0.05 mm/min
45*	842.1	122.1	0.5 mm/min
46	856.5	124.2	0.05 mm/min
47	868.3	125.9	0.5 mm/min
48*	1045.7	151.6	0.5 mm/min
49*	1136.1	164.7	0.5 mm/min
50	1214.0	176.0	0.05 mm/min
<u>4 pt. Flexure 1370°C</u>			
51*	358.0	51.9	0.05 mm/min
52	370.3	53.7	0.05 mm/min
53	393.7	57.1	0.5 mm/min
54	421.4	61.1	0.5 mm/min
55	456.9	66.3	0.05 mm/min
56	462.4	67.0	0.5 mm/min
57	473.0	68.6	0.5 mm/min
58	478.9	69.4	0.5 mm/min
59	490.6	71.1	0.05 mm/min

TABLE 4 Flexure Strength Data for CNTD

SPEC.#	MPa	ksi	Strain Rate
<u>4 pt. Flexure 1370°C</u> Continued			
60*	510.2	74.0	0.05 mm/min
61*	517.7	75.1	0.5 mm/min
62	537.9	78.0	0.05 mm/min
63	581.5	84.3	0.5 mm/min
64*	593.9	86.1	0.05 mm/min
65	719.0	104.3	0.05 mm/min
66	741.4	107.5	0.5 mm/min
67*	919.5	133.3	0.5 mm/min
68*	975.7	141.5	0.5 mm/min

*Specimens chosen for elemental analysis

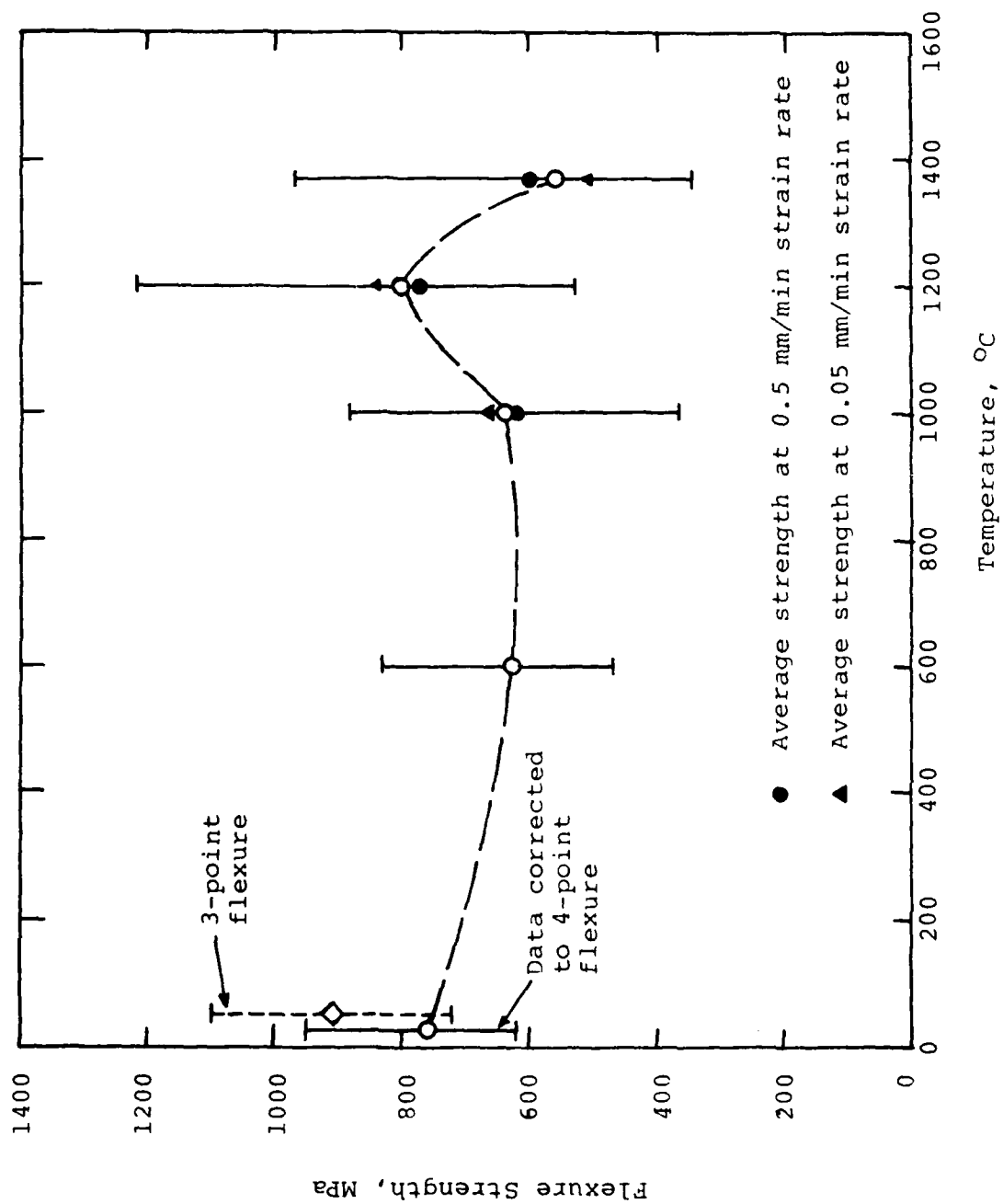


FIGURE 18: FLEXURE STRENGTH OF CHTD SIC AS A FUNCTION OF TEST TEMPERATURE

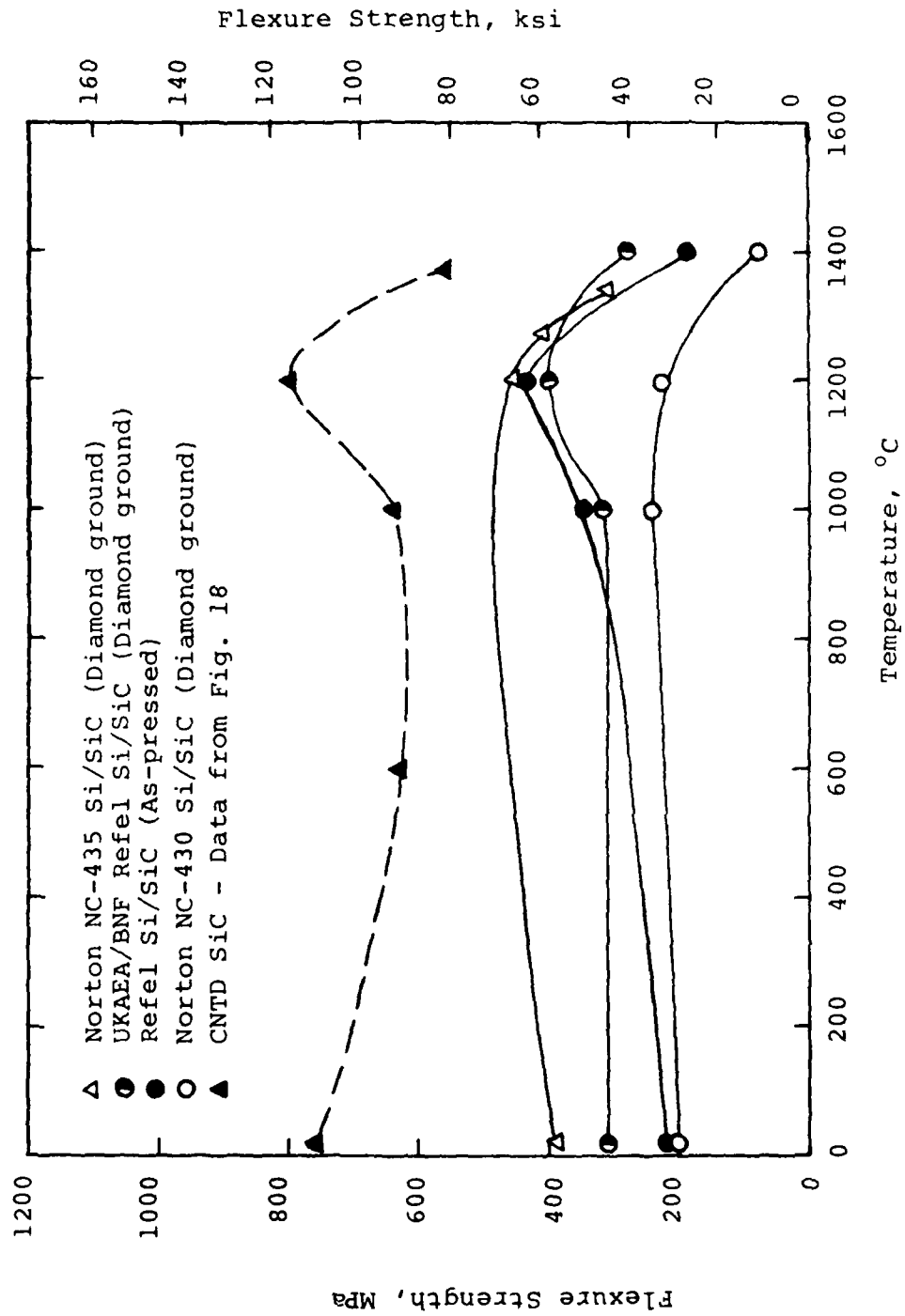


FIGURE 19: FLEXURE STRENGTH OF CNTD SiC AS A FUNCTION OF TEMPERATURE
IN COMPARISON TO SILICONIZED SiC MATERIALS (DATA FROM REF. #15).

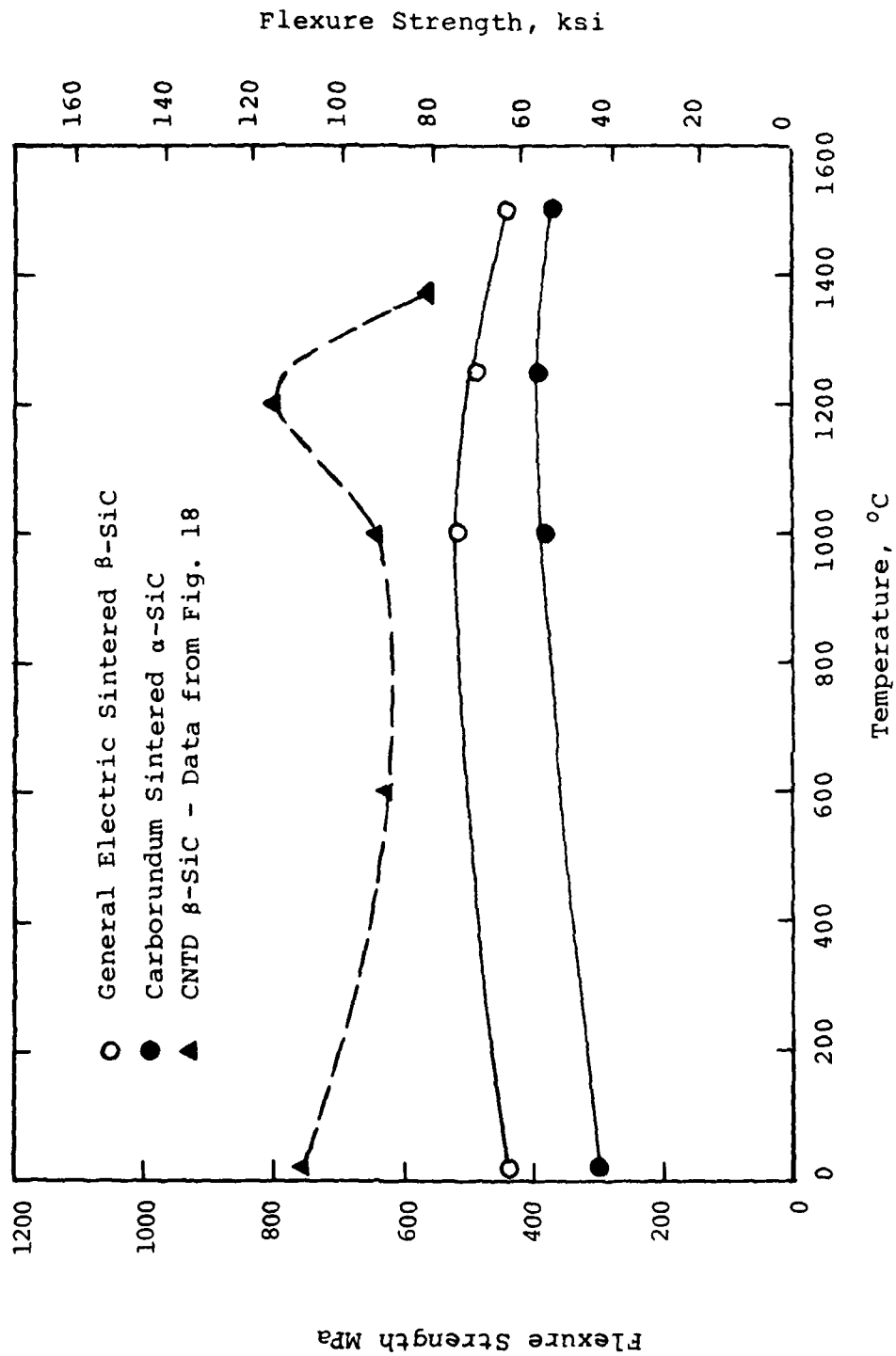


FIGURE 20: FLEXURE STRENGTH OF CNTD SiC AS A FUNCTION OF TEMPERATURE IN COMPARISON TO SINTERED SiC MATERIALS (DATA FROM REF. #15).

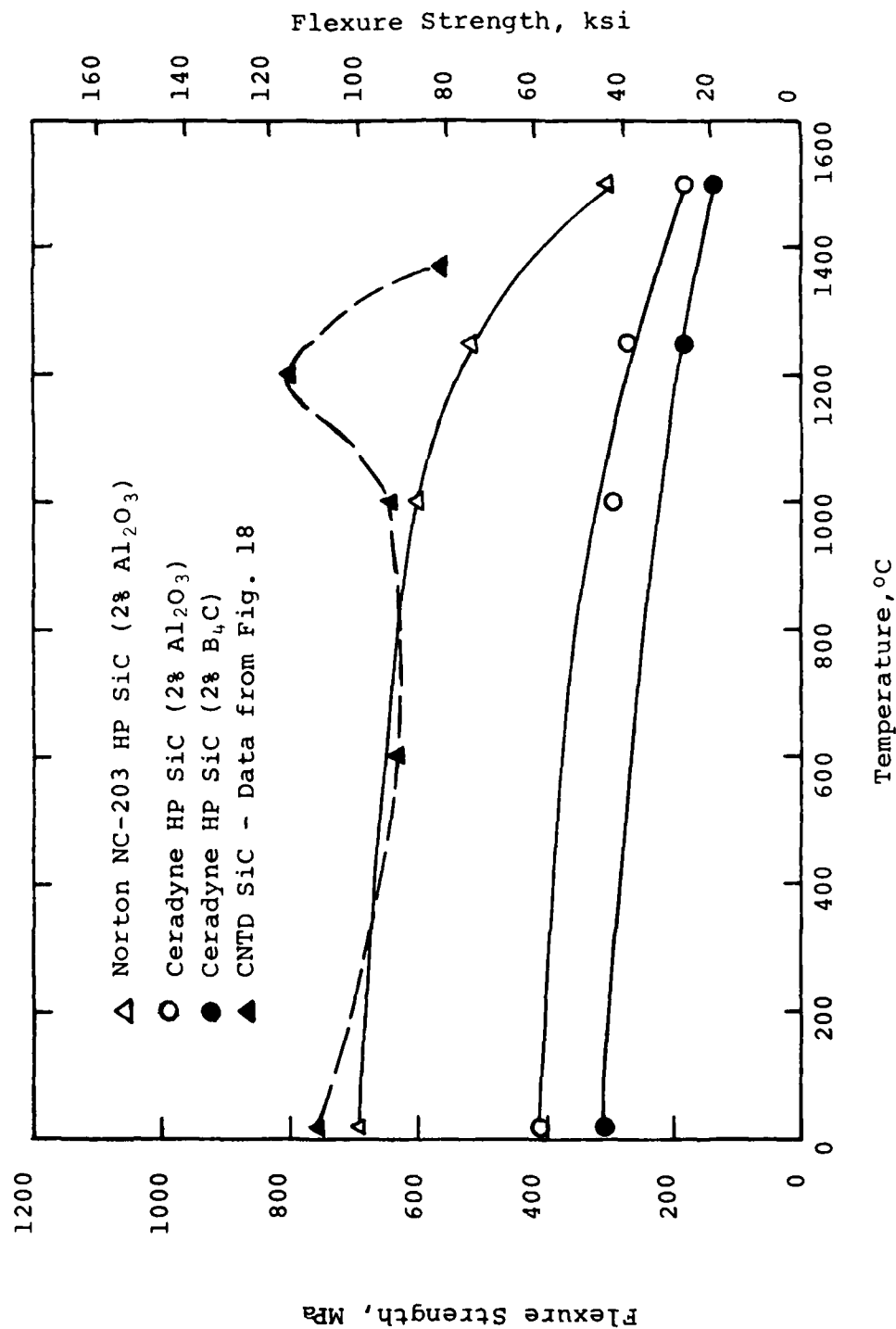


FIGURE 21: FLEXURE STRENGTH OF CNTD SiC AS A FUNCTION OF TEMPERATURE IN COMPARISON TO THE HOT-PRESSED SiC MATERIALS (DATA FROM REF. #15).

that the CNTD SiC appears somewhat stronger at 1200°C than at other temperatures. This behavior seems similar to that observed in the Si/SiC material and in the UKAEA/BNF REFEL material shown in Figure 19. In the light of elemental analysis data, which are presented in the next section, the similarity between the behavior of the CNTD SiC and that of the Si/SiC REFEL is interesting since both materials seem to contain excess free silicon.

The 1200°C maximum strength temperature is a temperature where softening of a second phase of silicon might lend a modicum of plasticity to the material and thereby impart some additional strength. We should also note, however, that 1200°C is just above the deposition temperature for the CNTD SiC and the relief of possible residual stresses is another factor which should be considered.

The large degree of variation in the data (large "scatter") is another feature of Figure 18 that should be mentioned.

We can assume that the scatter factor is, in part, due to material variations. However, we have found that our coated graphite test specimens themselves add a large uncertainty to the test method. The specimens are prone to acquire an unintentional trapezoidal cross section during the preparation of substrates, and, during deposition, edges tend to build thicker coatings than the flat surfaces. These two factors render the bend tests less reliable.

The statistical significance of these data is examined somewhat more carefully by the Weibull distribution analyses presented in Figures 22 through 28. Weibull analysis was performed by Dr. D. Kotchik of AiResearch, Torrance, California.

Care should be exercised when analyzing these figures. The data portrayed in them contain several inconsistencies which render some comparisons invalid or very risky. For instance, the room temperature data were obtained from three-point bend tests (38 mm span) at a crosshead speed of 0.15 mm per minute. The elevated temperature data, on the other hand, were all obtained in a four-point (major span 38 mm, minor span 19 mm) at cross head speeds of 0.05 mm per minute and 0.05 mm per minute.

Comparison of data from such a variety of sources is usually not strictly valid. Thus we should stress that the results portrayed in these figures should be taken as indicative only. Some conclusions would require that a great deal more data be generated in a more controlled, self-consistent manner.

There are several features shown in these figures which should be noted. First, we should underscore the low Weibull moduli which are shown by all the data sets.

A low Weibull modulus typically indicates large scatter. This scatter can result from one or more of several factors, viz. small sample population, errors in strength measurement

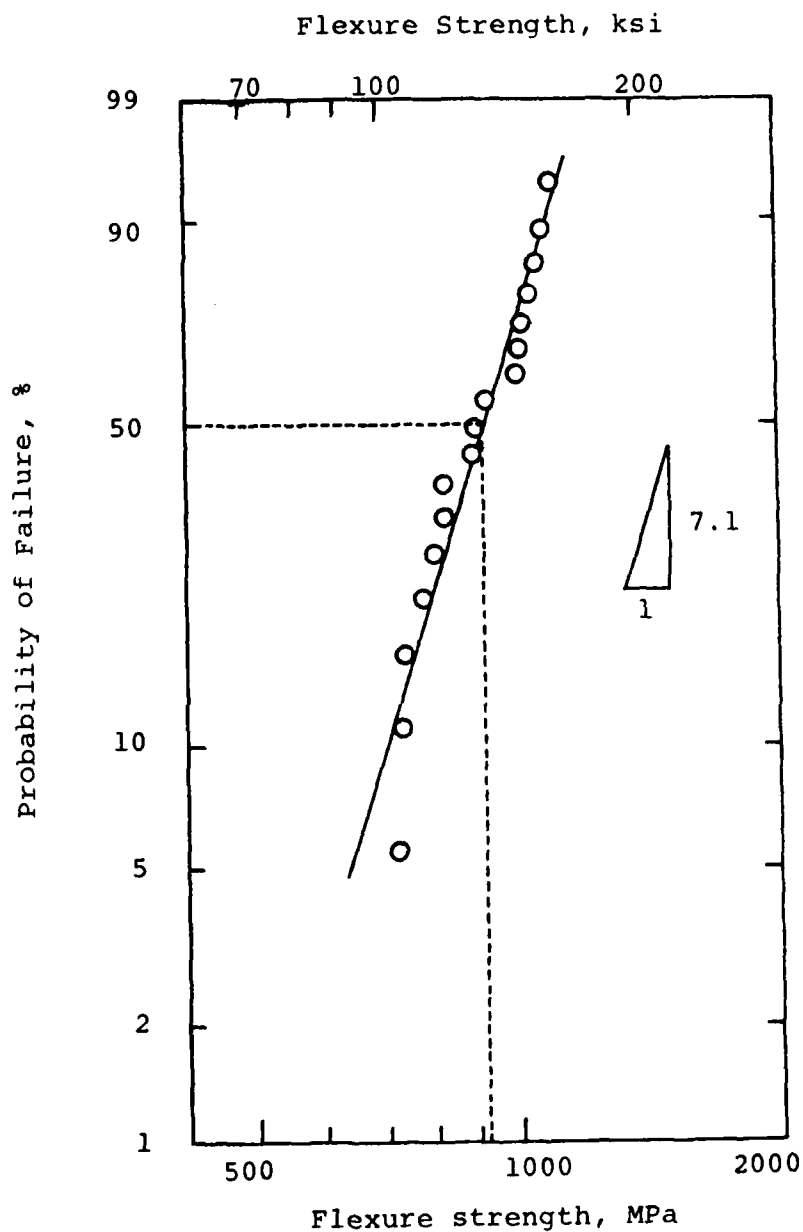


FIGURE 22; WEIBULL PLOT OF ROOM TEMPERATURE, 3-POINT FLEXURE STRENGTH DATA (STRAIN RATE = 0.15 MM/MIN) ON CNTD SiC DEPOSITED ON GRAPHITE.

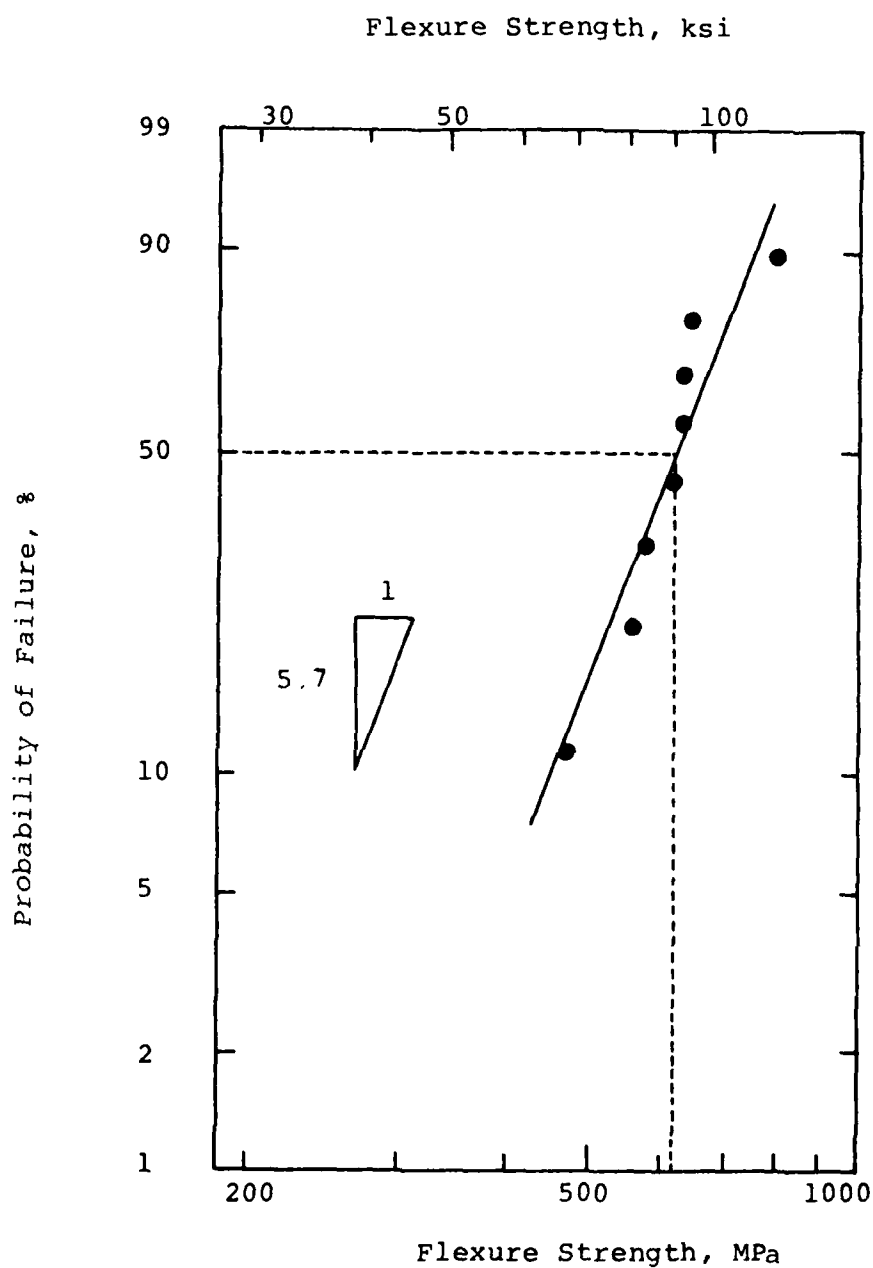


FIGURE 23: WEIBULL PLOT OF 600°C, 4-POINT FLEXURE STRENGTH DATA (STRAIN RATE = 0.5 MM/MIN) ON CNTD SiC DEPOSITED ON GRAPHITE.

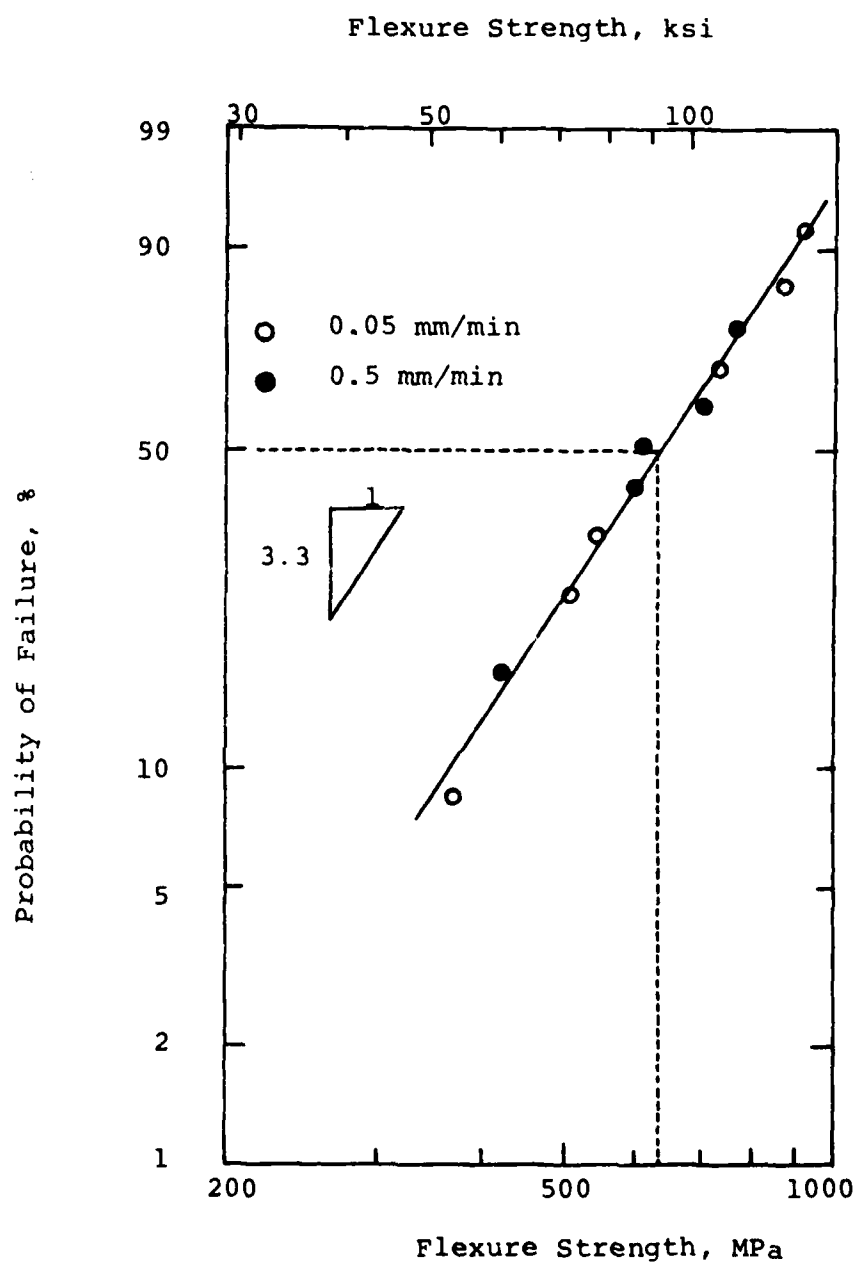


FIGURE 24: WEIBULL PLOT OF 1000°C FLEXURE STRENGTH (4-POINT) DATA FOR CNTD SiC DEPOSITED ON GRAPHITE.

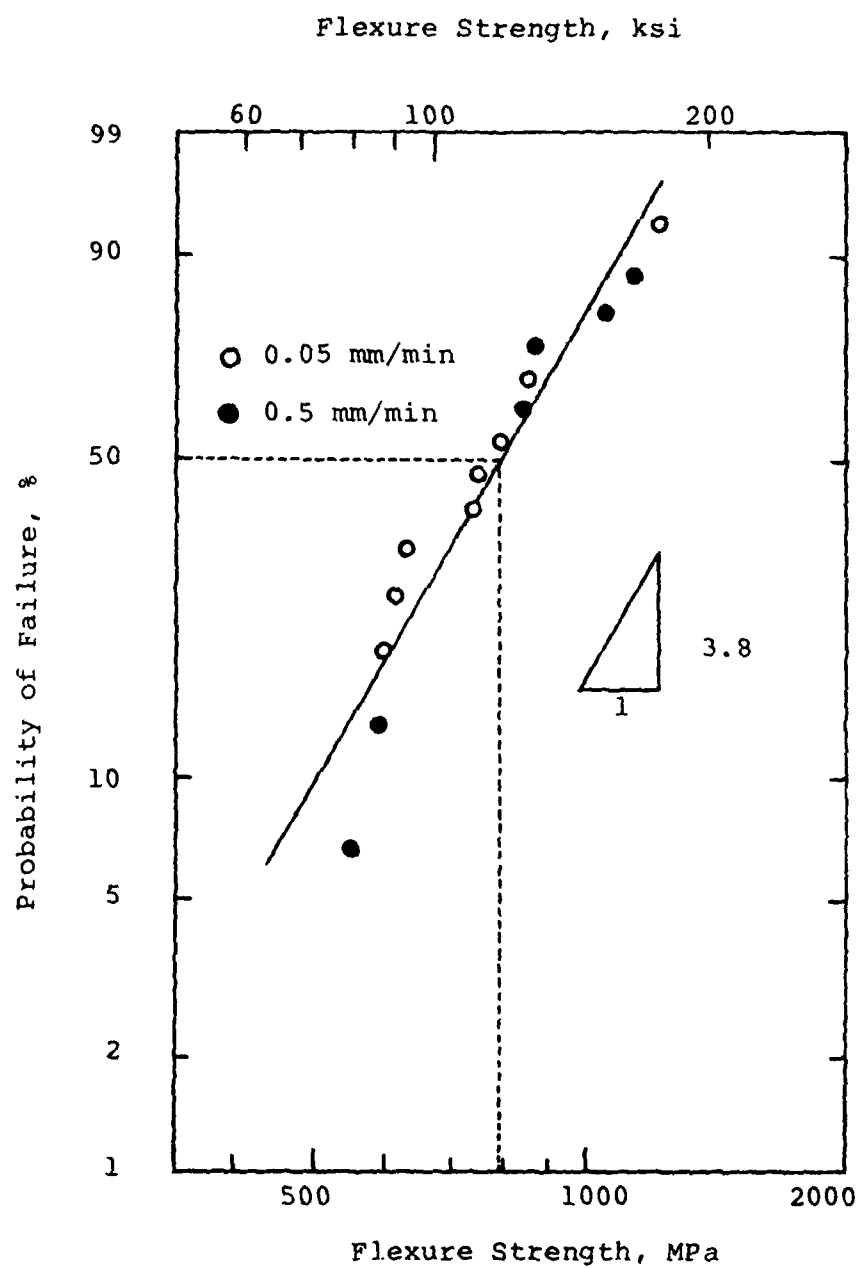


FIGURE 25: WEIBULL PLOT OF 1200°C, 4-POINT FLEXURE STRENGTH DATA AT DIFFERENT STRAIN RATES FOR CNTD SiC DEPOSITED ON GRAPHITE.

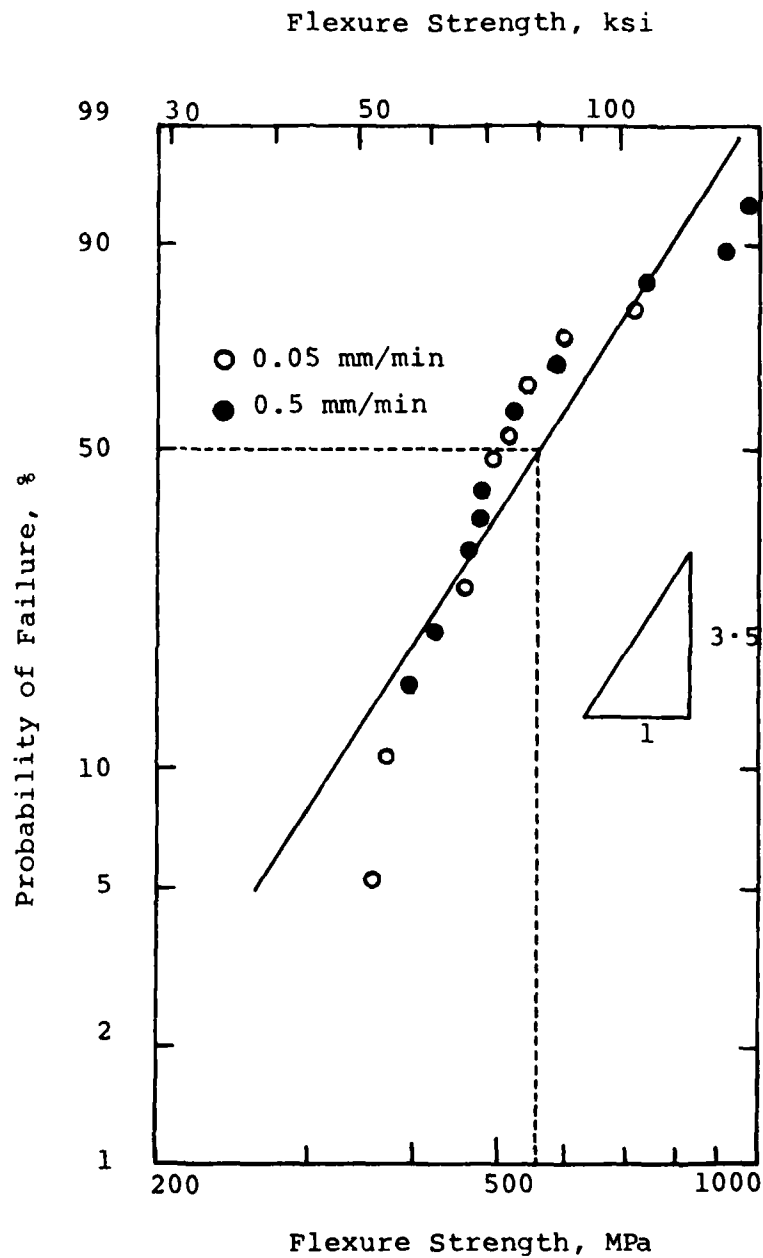


FIGURE 26: WEIBULL PLOT OF 1370°C, 4-POINT FLEXURE STRENGTH DATA AT DIFFERENT STRAIN RATES FOR CNTD SiC DEPOSITED ON GRAPHITE.

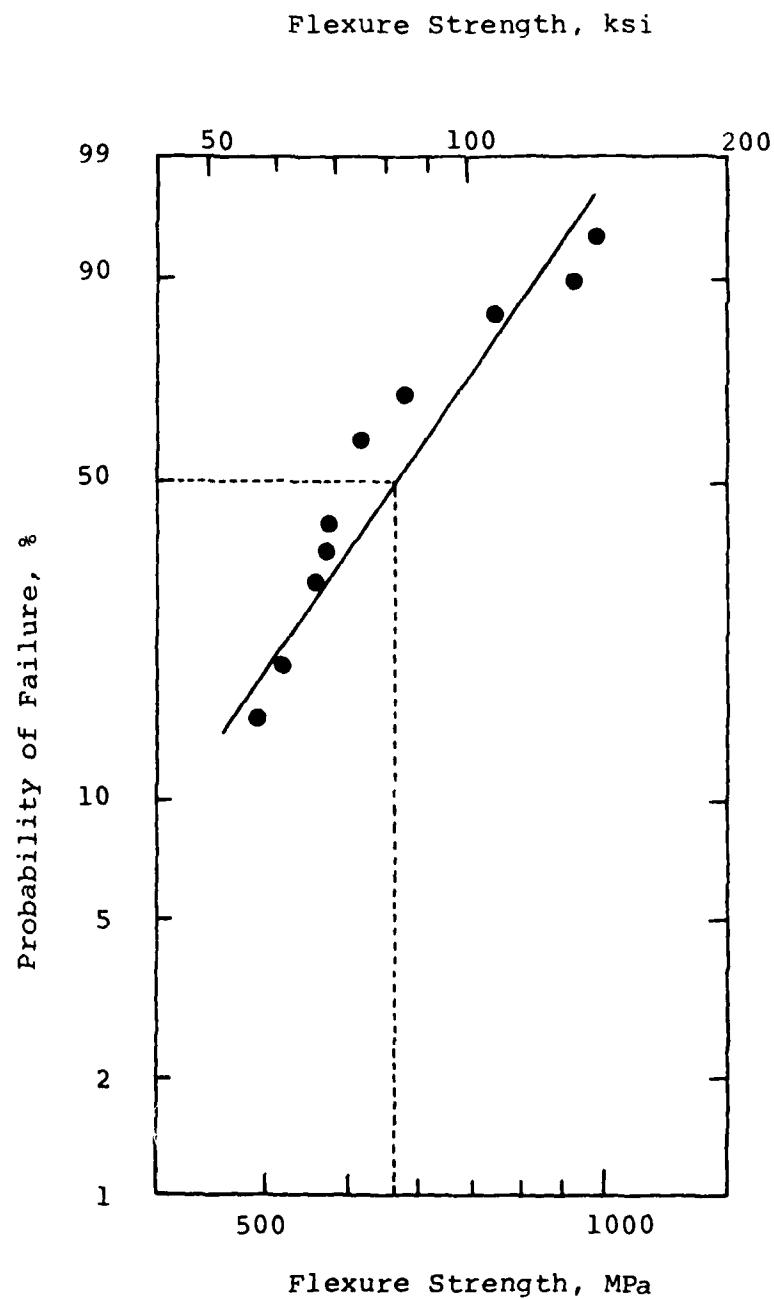


FIGURE 27: WEIBULL PLOT OF 1370°C FLEXURE STRENGTH DATA (4-POINT, 0.5 MM/MIN STRAIN RATE) FOR CNTD SiC DEPOSITED ON GRAPHITE.

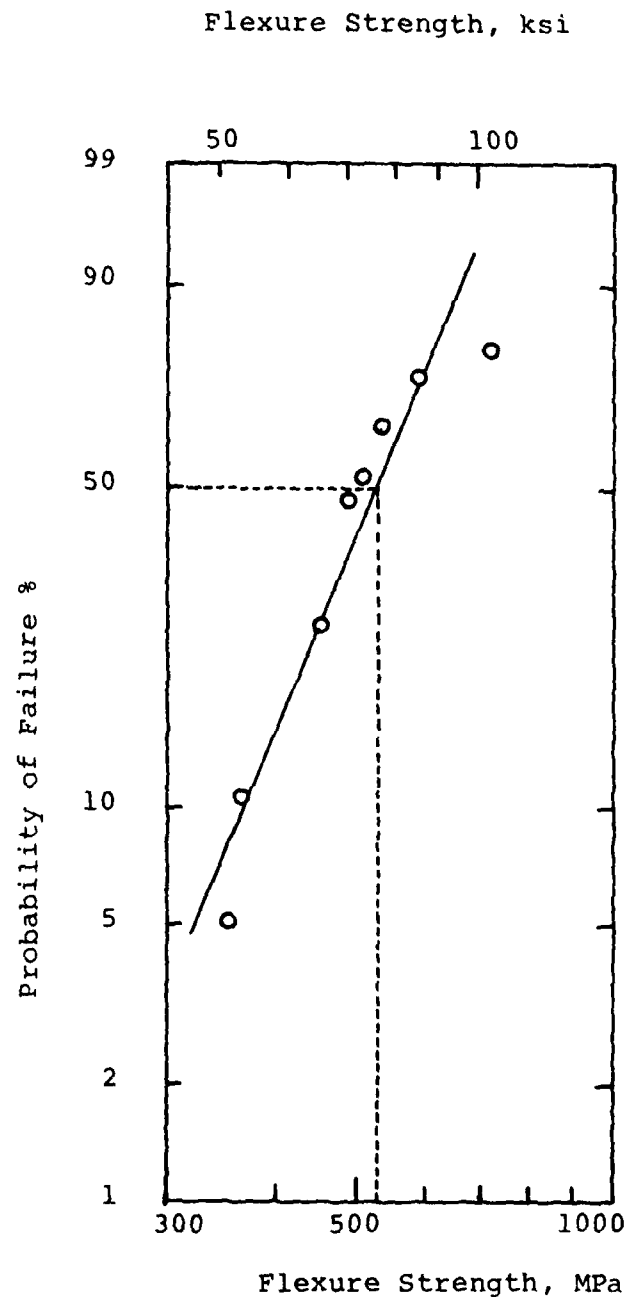


FIGURE 28: WEIBULL PLOT OF 1370°C, 4-POINT FLEXURE STRENGTH DATA (STRAIN RATE = 0.05 MM/MIN) FOR CNTD SiC DEPOSITED ON GRAPHITE.

as a result of sample alignment errors, or due to the effect of substrate surface finish, inherent material variation, etc. In the present case, the first two factors were clearly present. We examined the effect of surface finish of substrate on the strength. These results are included in Appendix B. The variation in the material properties is always a significant factor. In a CVD material, this factor is particularly significant when difficulties arise in controlling the local gas compositions in a reactor. We found this to be the case in our CNTD SiC deposits, as shown dramatically in the residual stress study described in Section III-B.4.

The 1370°C data (See Figure 26) did not fit a straight line plot very well. In fact, it appears as though a break exists near the middle of the data set. Such statistical behavior might indicate that two failure modes might exist within the data set.

Since Figure 26 illustrates data which were taken at two different crosshead speeds, we examined the two data sets separately. Figure 27 shows the 1370°C data that were obtained at a crosshead speed of 0.5 mm per minute and Figure 28 shows the 0.05 mm per minute data. Although the break in the data (near the 50 per cent level, or at about 483 MPa is still apparent in the 0.05 mm/min data, it is absent in the 0.05 mm/min data.

Our data set is far too small to allow us to draw any conclusion. Therefore, all we can say is that there might be two failure modes in the high temperature tests and that

the failure mode might be strain rate dependent. More carefully conducted high temperature tests would be necessary to draw firm conclusions.

Figure 28 illustrates how the two higher temperature data sets each separate into subsets when the data are separated on the basis of the two different crosshead speeds. As the temperature goes up the tests performed at the slower crosshead speed show a much lower mean strength relative to those performed at the faster crosshead speed.

Again, we have too little data and too much variance to allow us to draw a firm conclusion. However, if this observation were to prove real with additional test results then it would indicate the strong possibility of a slow crack growth phenomenon at the lower crosshead speed.

III-B.3 Elemental Analysis

Thirty specimens chosen from the group that were mechanically tested under the task described in Section III-B.2 were sent to a commercial analytical laboratory for elemental analysis. Those specimens chosen are indicated by an asterisk in Table 4. The test method was described by this laboratory as follows: "The analysis was performed in the following manner: The entire contents of each sample was ground in agate and ignited in a muffle furnace at 620°C overnight in excess air. The resulting ash was analyzed combustimetrically (coulometric titration) for carbon, gravimetrically for silicon and colorimetrically for chlorine."

TABLE 5: Chemical Analysis of CNTD SiC samples

Sample #	Test Temp., °C	Carbon (w/o) (Coulometric)	Silicon (w/o) (Gravimetric)	Chlorine (w/o) (Colorimetric)
1	R.T.	26.7	71.8	0.03
6	R.T.	26.9	68.7	0.18
7	R.T.	25.0	74.0	0.06
14	R.T.	24.9	74.7	0.11
16	R.T.	22.6	72.6	0.07
17	R.T.	23.5	72.9	0.16
18	600	22.4	74.9	0.17
20	600	25.9	74.0	0.06
21	600	26.5	69.7	0.14
23	600	26.5	73.5	0.08
25	600	27.7	69.3	0.39
26	1000	20.0	77.5	0.12
29	1000	26.6	71.9	0.11
31	1000	27.4	72.9	0.13
32	1000	27.0	72.6	0.13
34	1000	22.8	77.1	0.17
35	1000	25.7	75.4	0.08
39	1200	25.2	71.5	0.12
40	1200	26.4	71.4	0.41
43	1200	24.6	72.4	0.18
45	1200	21.2	77.1	0.05
48	1200	22.2	74.8	0.08
49	1200	25.7	73.6	0.07
51	1370	23.7	73.5	0.06
60	1370	26.1	70.7	0.05
61	1370	27.8	70.1	0.07
64	1370	20.1	80.4	0.05
67	1370	25.0	72.5	0.10
68	1370	24.2	74.4	0.07

The results of this analysis are given in Table 5. The ash content of the graphite substrate was determined to be about 4% of the total and a separate analysis of the graphite substrate showed its composition to be that listed in Table 6.

TABLE 6

Carbon Residue Analysis

C	ND	Mo	0.02%
Si	5.0%	Cr	0.02%
V	1.5%	Mn	0.02%
Ti	0.8%	Sr	0.02%
Fe	0.4%	B	0.008%
Al	0.1%	Cu	0.005%
Zr	0.1%	Mg	0.002%
Ni	0.05%	Ca	Balance

ND = Not Detected

The contribution of silicon from the graphite substrate to the total analysis of coated specimens was then 5% of 4%, or about 0.2%. We neglected this contribution and assumed all Si reported in Table 5 to be from the coating.

It is immediately apparent from Table 5 that all of the specimens contain an excess of silicon. Stoichiometric SiC has 70% silicon and 30% carbon by weight. None of the specimens tested had more than 28 w/o carbon.

If we assume that any free carbon that might have been present in these test specimens would have been oxidized and removed during their preparation for elemental analysis in

the same manner that the graphite substrate material was removed, then we can further presume that all the carbon detected is bound as SiC. The excess silicon content of a specimen will then be that amount of measured silicon beyond what is required to balance the measured carbon, or

$$(\text{Excess w/o Si}) = (\text{measured w/o Si}) - (\text{measured w/o C}) \times \frac{\text{At.wt.Si}}{\text{At.wt.C}}$$

Table 7 lists values of excess silicon for our test specimens.

In determining the excess silicon, we have neglected the presence of chlorine, since it is not clear exactly how it might be present in the sample. One possibility is that it could be present as a subhalide of silicon, such as $\text{SiCl}_{2.6}$.⁽²⁾ However, in the absence of any definitive evidence, we decided to neglect its presence. Calculations show that the error in the value of free silicon, as a result of this assumption, is negligible.

The bend strength data discussed in the preceding section can be normalized to remove the temperature dependence by plotting $\sigma(T)/E(T)$, instead of just σ values. If we assume that our material has an $E(T)$ as shown in Figure 29 (curve A) where the $E(25^\circ\text{C})$ measured by X-ray Diffraction has been extended as a function of temperature in a manner similar to the NC 203 HP αSiC , then Figure 30 illustrates $\sigma(T)/E(T)$ vs Excess Si for our CNTD SiC.

TABLE 7: Excess silicon in CNTD SiC samples flexure
tested at various temperatures

Sample#	Test temperature °C	Excess silicon w/o
1	R.T.	9.5
6	R.T.	6.4
7	R.T.	15.7
14	R.T.	16.6
16	R.T.	17.8
17	R.T.	18.1
18	600	22.6
20	600	13.6
21	600	7.9
23	600	11.9
25	600	4.7
26	1000	30.8
29	1000	9.8
31	1000	9.0
32	1000	9.6
34	1000	23.9
35	1000	15.4
39	1200	12.7
40	1200	9.8
43	1200	15.0
45	1200	27.6
48	1200	23.0
49	1200	13.6
51	1370	18.2
60	1370	9.8
61	1370	5.2
64	1370	33.5
67	1370	14.2
68	1370	17.9

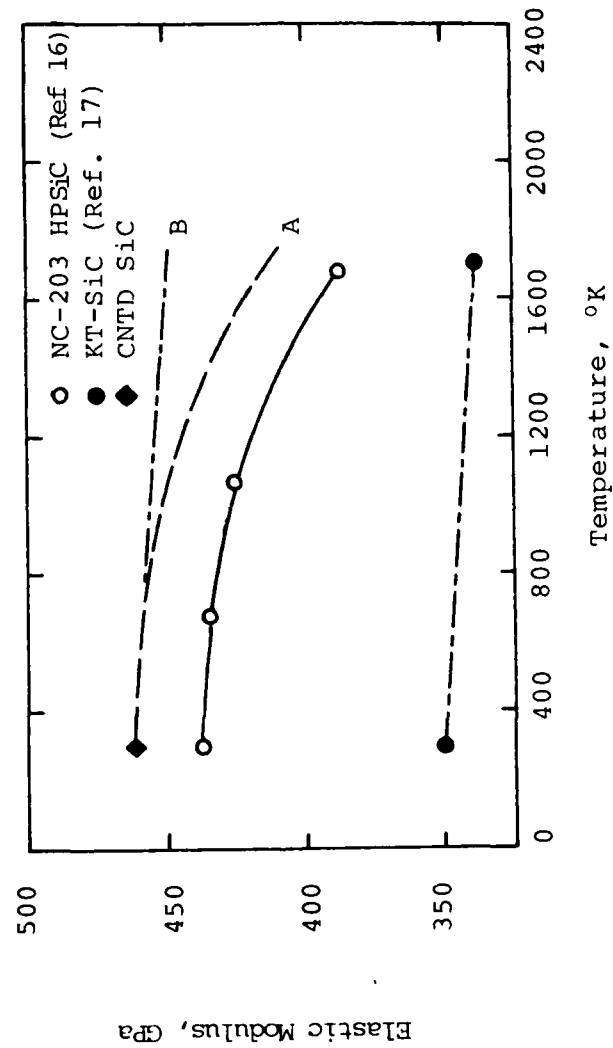


FIGURE 29: ELASTIC MODULUS AS A FUNCTION OF TEMPERATURE FOR VARIOUS SiC MATERIALS.

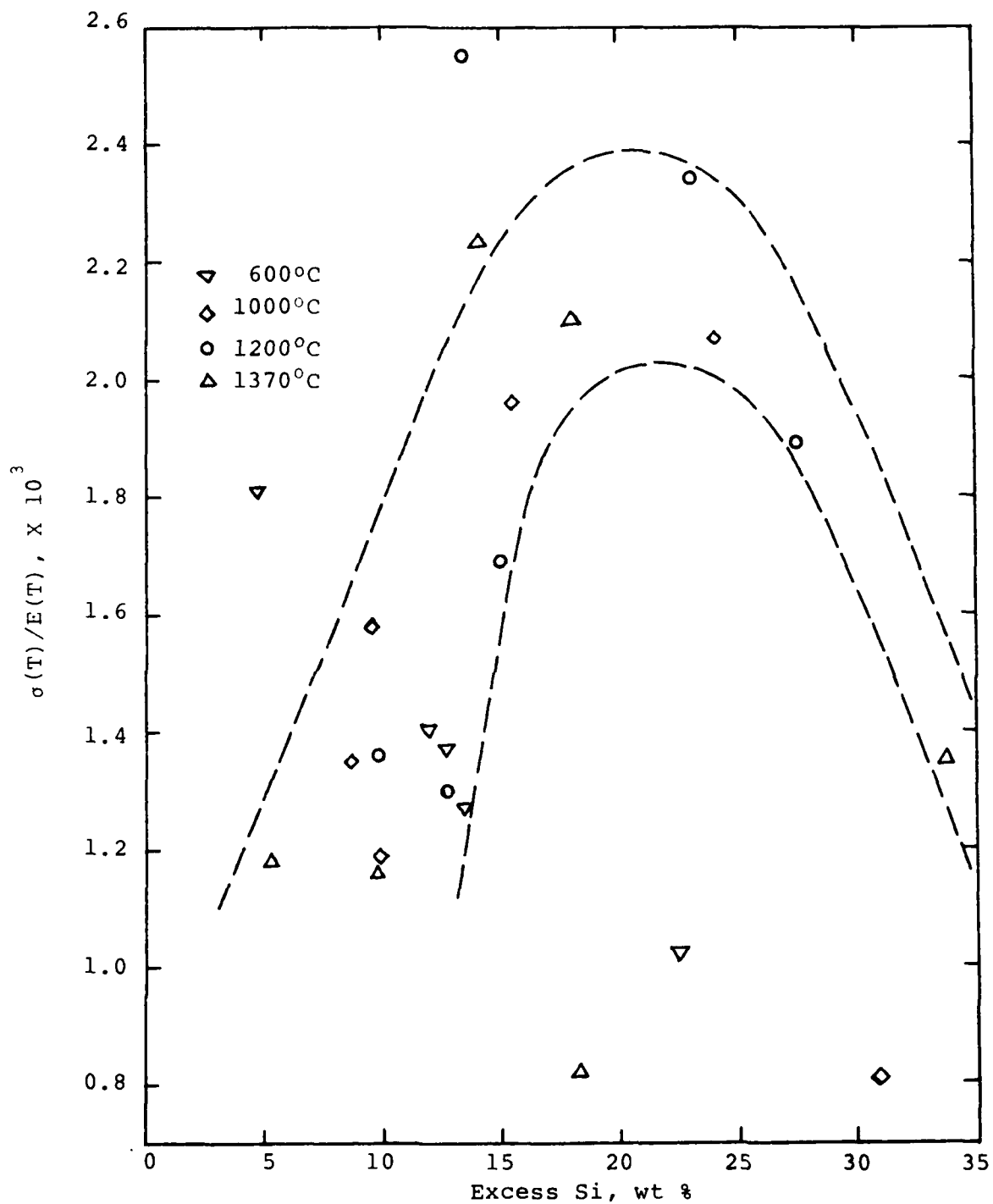


FIGURE 30: NORMALIZED HIGH-TEMPERATURE FLEXURE STRENGTH OF CNTD SiC ON GRAPHITE BEND BARS AS A FUNCTION OF EXCESS SILICON (FURNACE DEPOSITS).

Figure 30 must be viewed with extreme caution. The data might imply (as indicated by dotted lines) a maximum strength at about 20 w/o excess silicon. However, the degree of scatter is high and the statistical sample is relatively small. Therefore, this interpretation represents only our conjecture and cannot be taken as conclusive.

Also, we must emphasize that our assumption of a temperature dependence of E similar to NC 203 might not be valid. In fact, a two phase SiC/Si material made by Carborundum, KT-SiC, which has about 20 volume % of free Si, has an E vs T relationship of: ¹⁷

$$E = 351.5 - 1.6 \times 10^{-6} \times T (^{\circ}\text{C}) \text{ GPa}$$

The elastic modulus of the material is somewhat dependent on the free silicon content. Although the temperature coefficient of the E in the KTSiC is not significantly affected, the free Si content does affect the room temperature value. ¹⁷

Again, since our CNTD SiC is also a SiC/Si two phase material and might behave more like the KT-SiC (Curve B, Figure 29) than the NC 203, the relationship of strength to free Si content which is loosely indicated in Figure 30 cannot be accepted with assurance.

Figure 31 displays the relationship of the hardness of specimens to the excess silicon content. The dotted lines present a subjective judgment of the relationship between

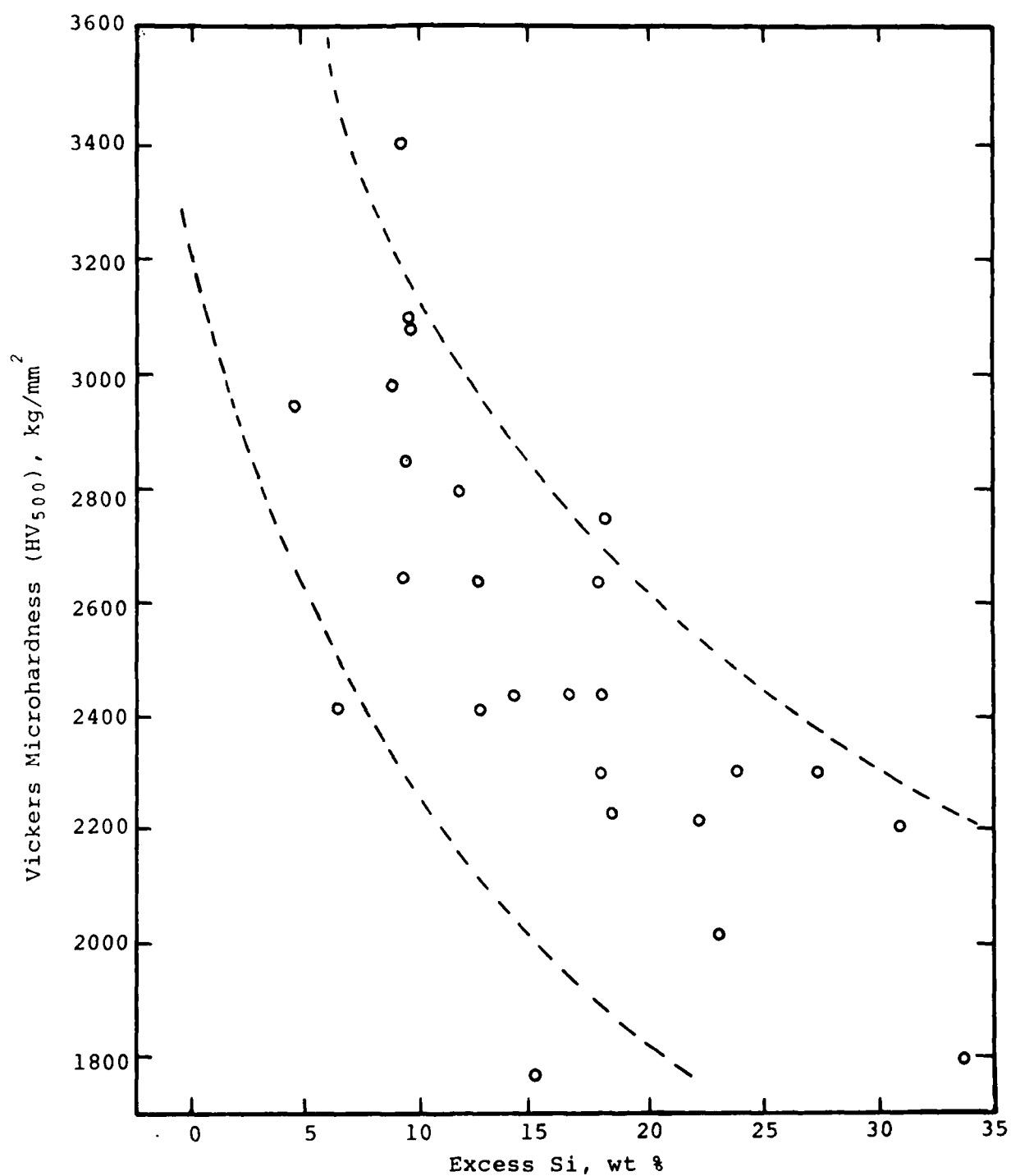


FIGURE 31: VARIATION OF HARDNESS OF CNTD SiC DEPOSITED ON GRAPHITE AS A FUNCTION OF EXCESS SILICON (FURNACE DEPOSITS).

hardness and silicon content. The Vickers Hardness values plotted in Figure 31 were obtained from companion specimens on which elemental analysis was performed. Our experience has shown that there is a variation of hardness of approximately $\pm 10\%$ between specimens deposited together. Therefore, errors of from ± 200 to ± 300 Vickers are present in these data. In fact, we note that this error figure is just about equal to the width of band which subjectively defines the behavior of the data in Figure 31.

We compared these data to those displayed in Figure 13 from the first year's work. As shown in Figure 32, the two sets of data compare quite well, as long as we assume that the hardness maximum of Figure 13 actually defines the stoichiometric composition for the resistance heated specimens. In other words, if we assume that the excess silicon data determined by EDAX was systematically wrong by about 10 wt %, then the two sets of data compare well. We believe that Figure 32 portrays the actual relationship between silicon content and the hardness of our deposit.

III-B.4 Residual Stress Measurements

The chemical vapor deposition process is known to introduce residual stresses into deposited material. Since residual stresses can significantly influence the mechanical properties of the deposit, we attempted to obtain some idea of the level of stresses residing in our deposits.

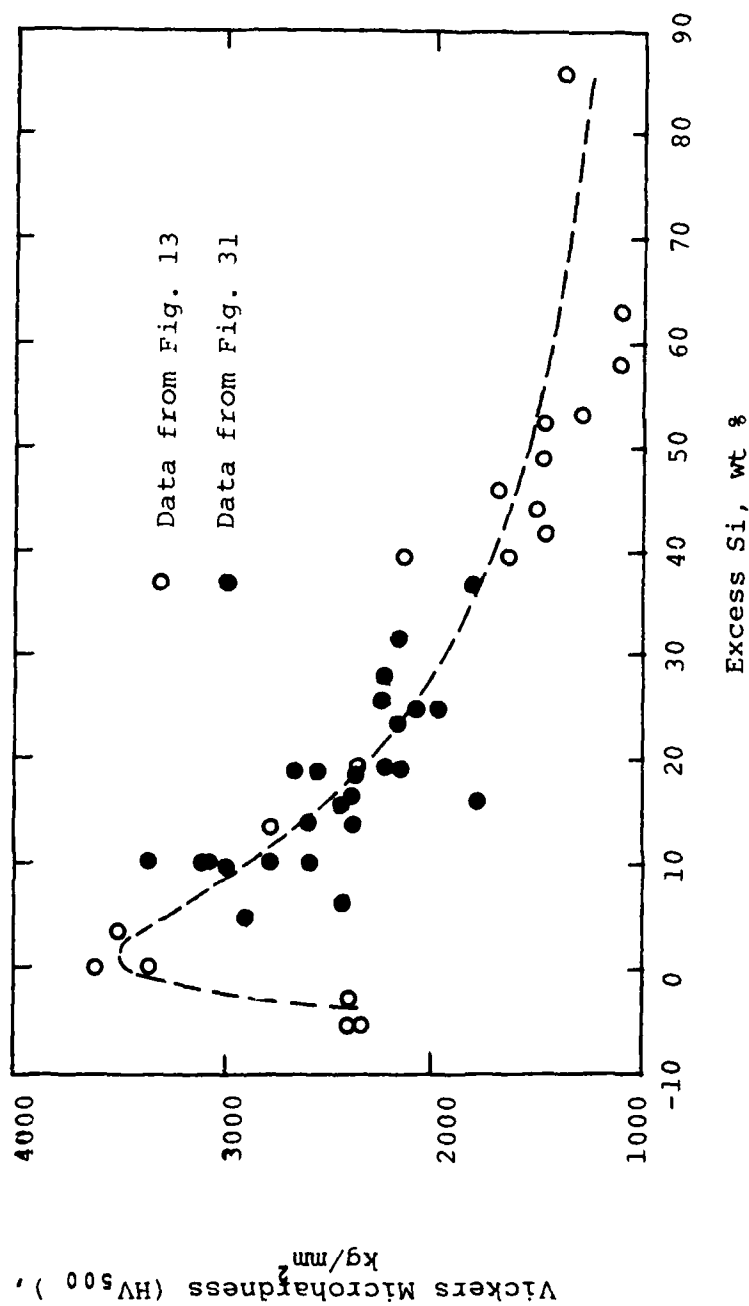


FIGURE 32: COMPARISON OF THE VARIATION OF HARDNESS AS A FUNCTION OF EXCESS SILICON FOR CNTD SiC MADE ON RESISTANCE-HEATED AND RADIATION-HEATED GRAPHITE.

Several specimens were sent to Lambada Research Inc., Cincinnati, Ohio for analysis of surface residual stresses by X-ray diffraction. The method is described in their report which is included as Appendix C. Their results are summarized in Table 8. These results are graphically portrayed in Figures 33, 34, and 35. Lambda Research reports ± 276 MPa error figure for these measurements. (See Appendix C).

The residual stress fields depicted in Figure 33 through 35 are surprising in several ways. The magnitude of the compressive stresses, which approach 2330 MPa is very high. The amount of spatial variation and associated high gradients are also surprising.

The most common source of stress in chemical vapor deposited coating is a disparity between the thermal expansion characteristics of the coating and the substrate. The stress fields produced by such disparity would vary smoothly and would not demonstrate the erratic variations that are shown in these figures. On a microstructural scale, however, other causes of residual stresses are inherent in the CVD process. These include:⁹

- 1) Surface tension forces of developing crystallites.
- 2) Lattice-mismatch stresses between neighboring crystallites.
- 3) Stresses introduced by diffusion phenomena and phase transformation phenomena.

TABLE 8: Surface Residual Stress in CNTD SiC
Deposit As Measured by XRD

Flat Sample

Location (mm, from center)	Residual Stress, MPa	
	Longitudinal	Transverse
0.0	-1795	-1276
2.5	-2330	-1241
5.1	- 10	- 600
7.6	- 917	-1634
10.2	-1108 (-1569)	- 669

() indicates repeat measurement.

12.7 mm dia. cylinder

Location (mm, from center)	Residual Stress, MPa	
	Longitudinal	Circumferential
0.0	-1062	-1800
5.1	- 634	-1117
10.2	- 196	- 821
15.2	- 965	- 903
20.3	-1490	- 924

38.1 mm dia. cylinder

Location (mm, from center)	Residual Stress, MPa	
	Longitudinal	Circumferential
0.0	- 88	-1469
5.1	-1214	-1655
10.2	- 497	-1069
15.2	-1360	-1048
20.3	- 903	- 290

Note: This table is reproduced from Appendix C.

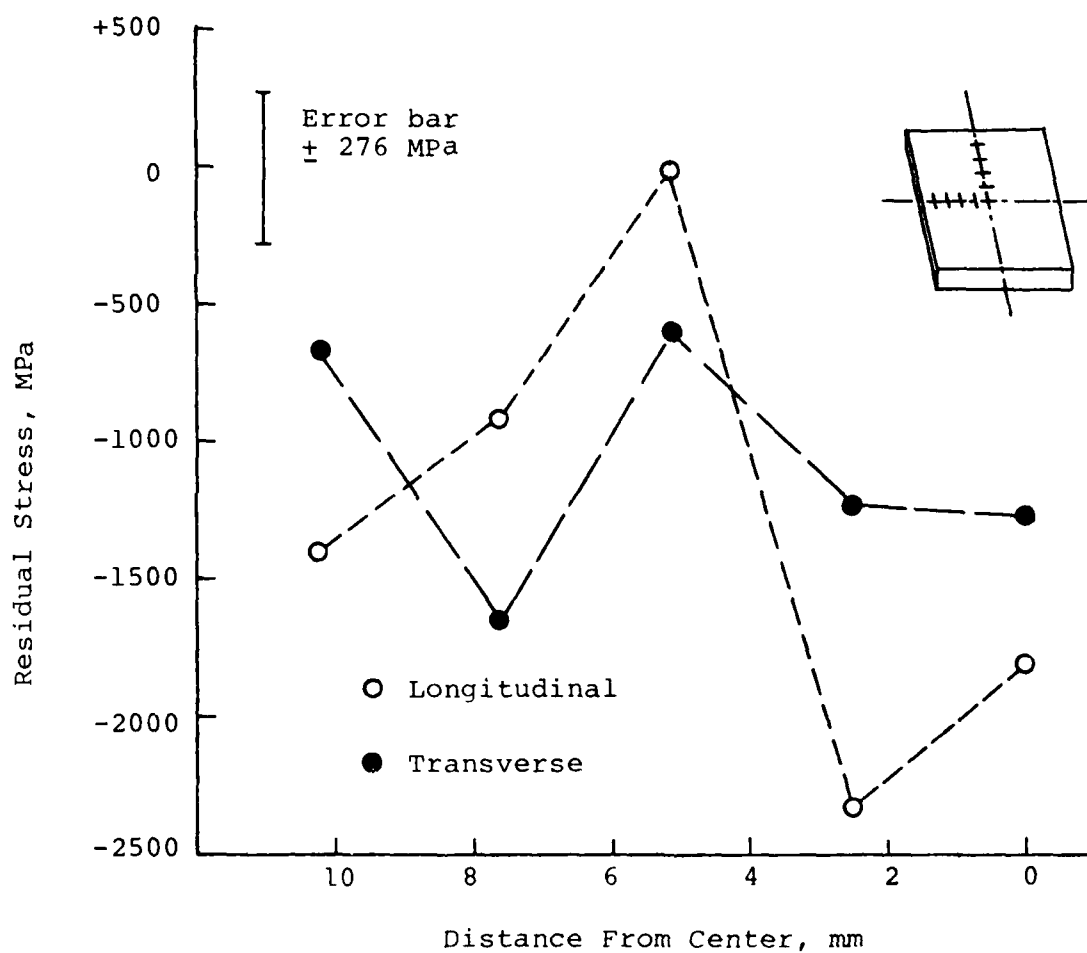


FIGURE 33: RESIDUAL STRESS IN A FLAT PLATE OF CNTD SiC DEPOSITED ON SiC₆ GRAPHITE SUBSTRATE.

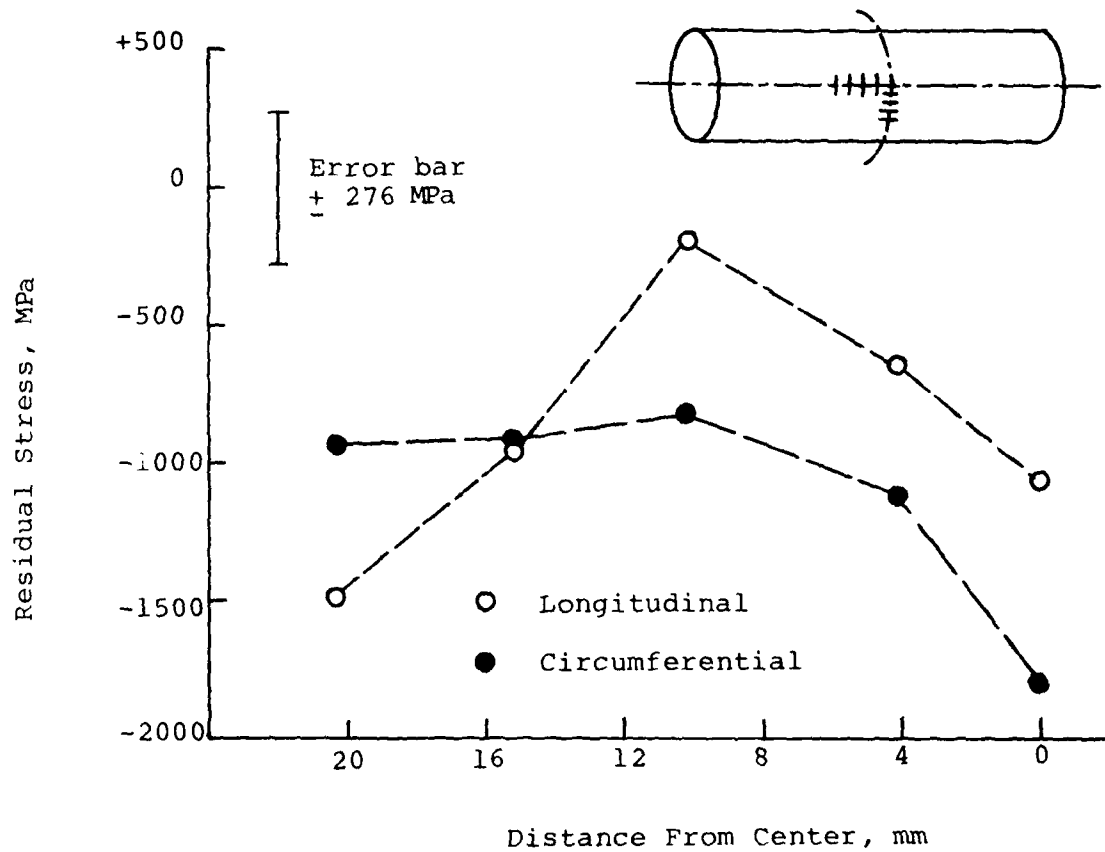


FIGURE 34: RESIDUAL STRESS IN A 12.7 MM DIAMETER CYLINDER OF CNTD SiC DEPOSITED ON SiC₆ GRAPHITE SUBSTRATE.

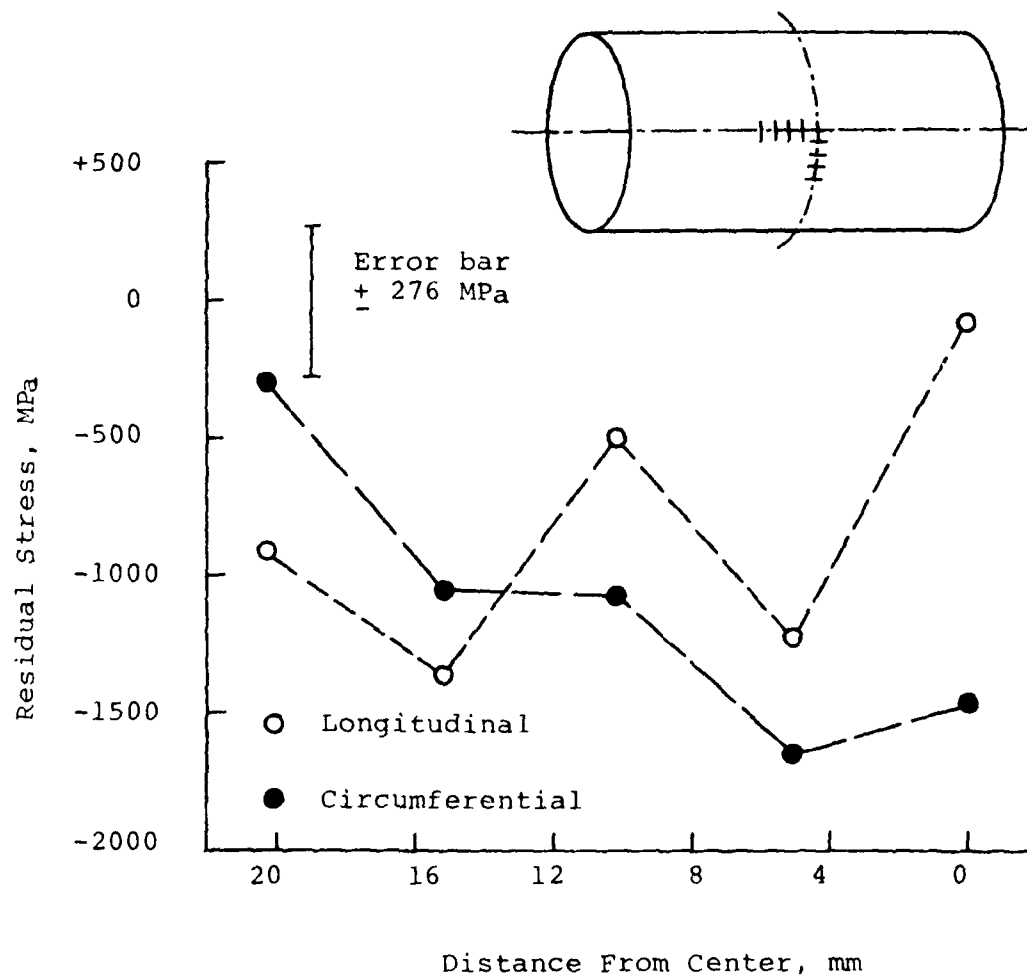


FIGURE 35: RESIDUAL STRESS IN A 38.1 MM DIAMETER CYLINDER OF CNTD SiC DEPOSITED ON SiC₆ GRAPHITE SUBSTRATE.

AD-A108 581

SAN FERNANDO LABS PACOIMA CA

F/G 11/6

INVESTIGATION OF THE CNTD MECHANISM AND ITS EFFECT ON MICROSTRU--ETC(U)

SEP 81 D G BHAT, R M PANOS

F49620-79-C-0041

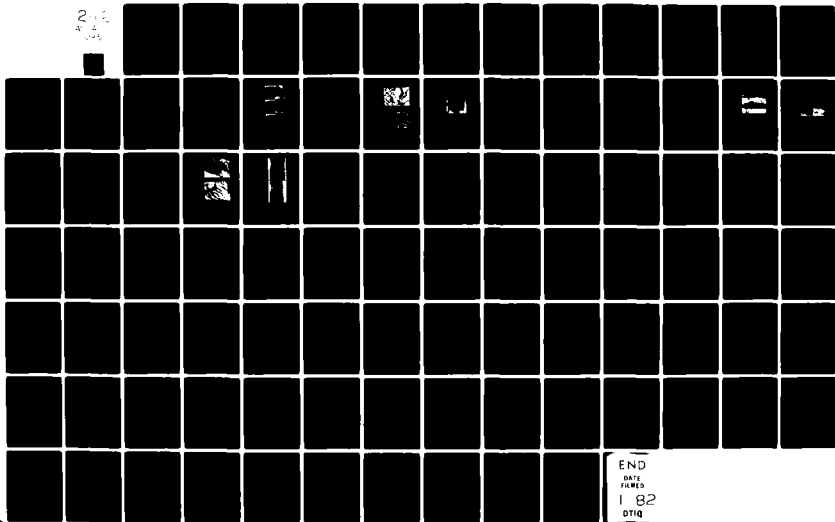
UNCLASSIFIED

AFOSR-TR-81-0748

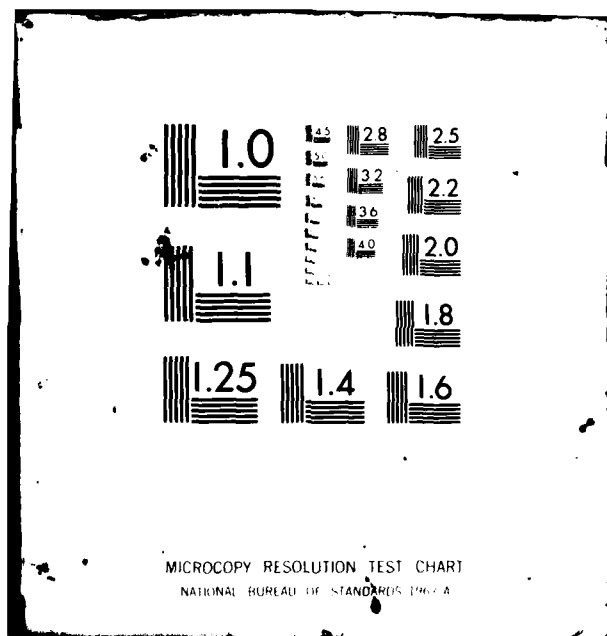
NL

2-11

4-11



END
DATE
FILMED
1 82
DTIC



- 4) Stresses introduced by occluded foreign matter; voids or inclusions.
- 5) Stresses introduced by anisotropy of crystallites.

Again, in a single phase homogeneous material, these stress-producing phenomena would be expected to produce macroscopic stress fields which would vary in a smooth and relatively slow manner across the specimen surface. In a two-phase material, however, several of these phenomena might yield quite erratically varying macroscopic stress fields, due to variations in local stoichiometry.

We suspect, in view of the evidence shown in Section III-B.3 above, that we have such a two phase material composed of SiC and Si microcrystals. We also suspect, in view of the wide variation in elemental analysis between specimens produced in the same deposition run that erratic variation in local chemical composition is possible in this material.

It would be interesting to try to correlate the local chemical composition and local residual stress level.

We did not attempt such an experiment due to the constraints of time and funds. Therefore, the cause of the large and erratic residual stresses that were observed must be discerned from various hypotheses.

III-B.5 Correlation with Run Conditions

Table 9 lists the conditions for deposition runs that were used to produce the specimens listed in Table 4.

TABLE 9: Correlation of Deposition Conditions with Properties of CVD SiC

Run #	Sample Identification (keyed to Table 4)	Flow rates of gases, ml/min					Excess Si, wt % From Table 7	$\frac{C(T)}{E(T)} \times 10^3$ Refer to Table 4	HV ₅₀₀ kg/mm ²
		MTS	SiCl ₄	Nitrogen					
				H ₂	Carrier	Blanket			
4488-464	1.56.58	600	250	11,500	38,400*	78,900*	9.5,-,-	1.6,1.1,1.1	3410
5016-376	2.18.26.27	600	225	10,000	22,600	36,400	-22.6,30.8 -	1.6,1.0,0.8,0.9	2200
4488-369	3.24.51.63	600	150	10,000	19,700	36,400	-,18.2,-	1.6,1.5,0.9,1.4	2740
4488-468	4.32	600	250	11,500	28,400	78,900*	-9.6	1.7,1.6	2630
5016-378	5.29.33.35	600	225	8,000	22,500	36,400	-9.8,-15.4	1.8,1.2,1.7,2.0	3100
4488-370	6.21.53.59	600	150	10,000	22,700	36,400	4,7.9,-,-	1.8,1.4,0.9,1.2	2410
5039-462	7	600	240	11,000	38,400*	78,900*	15.7	1.9	1990
4488-401	8.22.23.30	600	250	10,000	28,400	36,400	-,11.9,-	1.9,1.4,1.4,1.3	2790
4488-417	9.52.54.61	600	250	10,000	28,400	36,400	-,-,5.2	2.0,0.9,1.0,1.2	4085
4488-471	10.43.47	600	250	10,000	28,400	78,900*	-15.0,-	2.2,1.8,2.0	1775
5039-444	11.37.40	600	250	10,300	38,400*	88,900*	-,9.8	2.2,1.2,1.4	3080
5039-448	12.64.66	600	250	11,000	38,400*	73,900*	-33.5,-	2.2,1.4,1.8	1760
5039-461	13.20.49.50	600	250	11,500	38,400*	73,900*	-13.6,13.6,-	3.0,1.3,2.6,2.8	2725
5039-449	14.65.67.68	600	250	11,000	38,400*	78,900*	16.6,-14.2,17.9	2.3,1.7,2.2,2.3	2430
5016-374	15.38.41	600	250	10,000	28,400	36,400	-,,-	2.4,1.3,1.4	2290
5016-377	16.45	600	225	10,000	28,500	36,400	17.8,27.6	1.7,2.0	2290
5016-373	17.42	600	200	10,000	22,700	36,400	18.1,-	2.3,1.7	2620
5039-440	19	600	150	10,000	22,700	36,400	-	1.2	3200
5039-441	25.56.62	600	250	9,000	38,400*	88,900*	4.7,-,-	1.8,1.1,1.3	2940
4488-436	28.31	600	250	10,000	43,400*	98,900*	-9.0	1.1,1.4	2975
5039-450	34.36	575	250	10,000	38,400*	78,900*	23.9,-	1.8,2.1	2290
4488-437	39.44	600	250	10,000	43,400*	68,900*	12.7,-	1.3,1.9	2625
5039-462	46.48	600	250	11,500	38,400*	78,900*	-23.0	2.0,2.4	1990
4488-400	57.60	600	250	10,000	28,400	36,400	-9.8	1.1,1.2	2835

*Estimates. Flows exceed the capacity of flowmeters.

We examined the data listed in Table 9 and cursorily searched for any systematic relationship between the run conditions and the elemental composition, or the mechanical strength, of the coated specimens. We were surprised to be unable to find any such relationship. The apparent lack of any easily discernible pattern in these data demonstrates the intricacy and sensitivity of the process. Although it is possible that an elaborate regression analysis, which could account for interacting variables, might be able to find the relationships that elude us, we are not confident that our control over the individual process parameters is sufficiently tight to make any regression analysis worthwhile.

The process for CNTD SiC is obviously very sensitive to the process parameters; much more so than the ordinary CVD processes. Our control accuracy over individual process parameters ranges from $\pm 2\%$ for the active gas flows to $\pm 20\%$ for the high volume diluent nitrogen flows. Yet the free silicon content of CNTD SiC specimens varies from a value of 5% to 33% by weight; almost over an order of magnitude.

In short, we seem to have a complicated, multivariable process, which we do not yet know how to control well.

III-C Summary and Conclusions

San Fernando Laboratories has developed a furnace process capable of chemically vapor depositing a SiC material

microstructurally similar to the CNTD SiC material investigated under previous AFOSR Sponsorship.

We have characterized this material and found its mechanical properties to be superior on the average to any other SiC material available. We have also found it to have a very large degree of variability.

Elemental analysis has shown that the material contains an excess of silicon and since silicon has no solubility in SiC, this observation means that the CNTD SiC material produced by SFL's process is a two phase material of SiC and Si. The level of free Si was found to vary considerably with the earlier specimens varying from near stoichiometric to more than 70 wt % free silicon. Latter specimens seemed to stay within a range of from about 5 wt % to 30 wt % free silicon.

The paucity of our data and wide scatter within it, prevent us from drawing any statistically significant correlation between the free silicon content and other measured properties of the material. However, the simple knowledge that CNTD SiC contains free silicon leaves us with a strong suspicion that some functional relationship (such as the somewhat imaginative one, indicated in Figure 30) must exist between the free silicon content and the material's mechanical properties.

Through the course of this program we have learned that the CNTD SiC process requires the maintenance of a delicate balance between the gas temperature, the deposition

surface temperature, (surface reaction kinetics, surface diffusion rate, and crystal growth dynamics) and the active gas concentrations.

A rigorous control of the key process parameters, and greater understanding of the process and its sensitivity to all of its constituent variables will allow us to control the composition of deposited material.

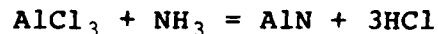
SECTION IV

AlN RESULTS AND DISCUSSIONS

The aluminum nitride research program was divided into two distinct efforts: (a) development of a strong CNTD structural AlN material and (b) characterizing the material as a potential electronic or electro-optical material. These efforts will be discussed separately. All run conditions for AlN deposition experiments are listed in Appendix A.

IV-A. Structural Material

We used two different approaches for the deposition of structural AlN material. One approach involved a parametric search for deposition conditions which would produce CNTD material using the basic chemical system:



The second approach involved the codeposition of a minor amount of second material which might interrupt grain growth and thereby promote grain refinement.

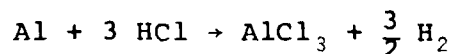
Although neither of these efforts were successful in producing a CNTD material, the codeposition experiments showed promise for future work. A significant grain refinement was achieved in AlN by causing a competitive deposition of small amounts of Si_3N_4 , and similarly in Si_3N_4 by causing a competitive deposition of small amounts of AlN.²⁰

IV-A.1 Equipment and Procedures

Figure 36 illustrates the deposition chamber which we used in these structural AlN experiments.

The AlN deposition apparatus was generally similar to that used in the SiC work described in Section III. The main difference between the two concerns the manner of supplying precursor gases. In the SiC process, precursor gases were introduced directly from pressurized containers or from vaporized pure liquids, while the AlN process required the in-situ generation of AlCl_3 .

Referred to as the "burner pot" or "aluminum pot", the AlCl_3 generator was a cylindrical quartz container located inside the vacuum chamber and just upstream from the deposition area. The burner pot had a porous graphite plug and was filled with granulated aluminum. A mixture of nitrogen and hydrogen chloride gas was passed through the pot to effect the following reaction:



Chlorine gas was specifically rejected as a reactant since it would react more exothermally and give us less control over the reaction.

Clamshell heaters supplied controlled heat to the burner pot and the gas mixing zone (Figure 36).

Deposition of AlN occurred downstream from the burner pot within a graphite furnace. The furnace was heated by induction using a 15 kw 3KHz motor-generator unit. Test

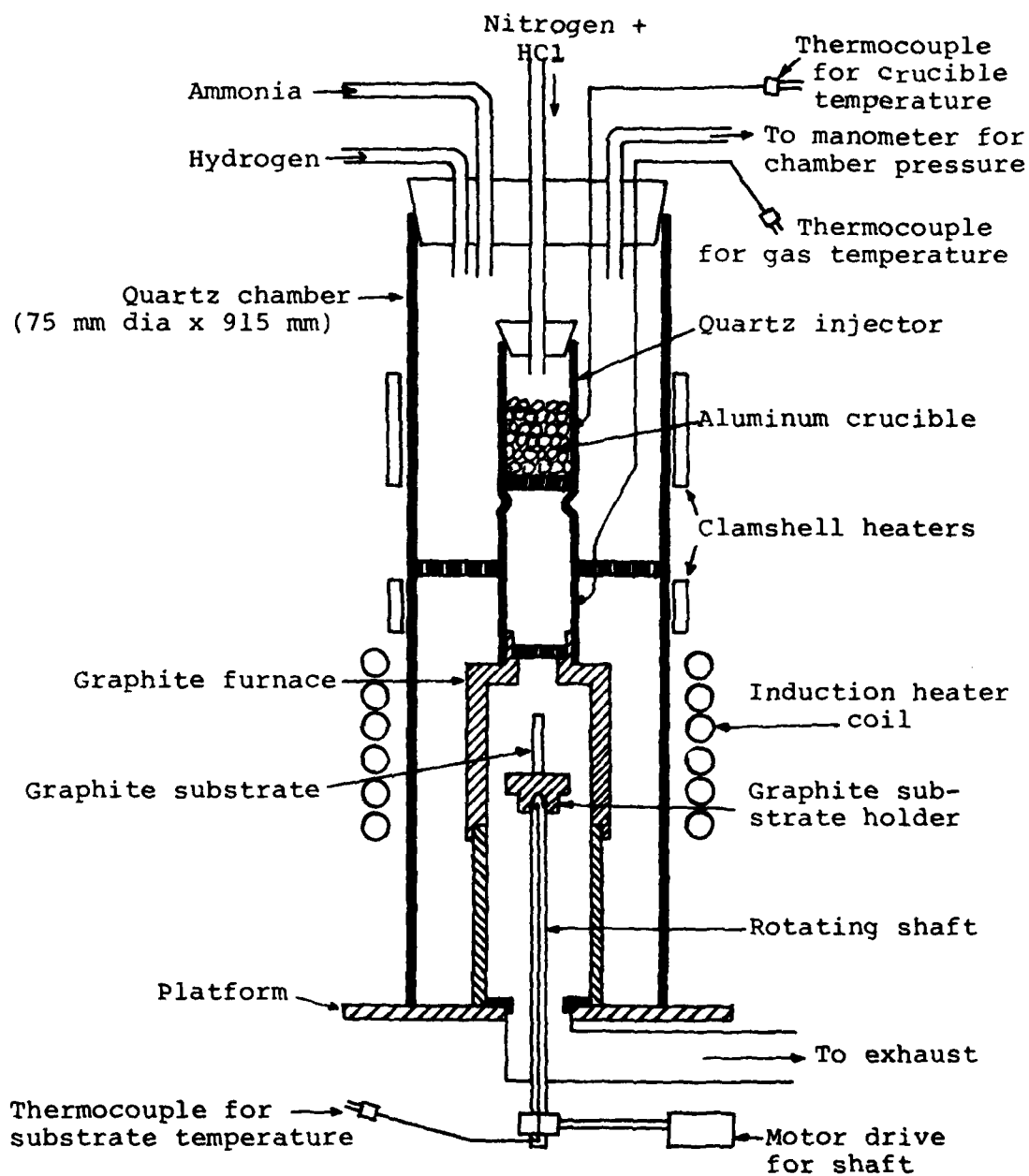


FIGURE 36: SCHEMATIC OF ALN DEPOSITION APPARATUS USING RADIANT (FURNACE) HEATING METHOD.

specimens were placed on a rotating stage near the center of the hot zone.

The apparatus was equipped with type K (chromel-alumel) thermocouples to monitor temperature of the burner pot, the gas mixing area, and the deposition stage. This set up was used for a part of the parametric investigation described in the following section.

IV-A.2 Parametric Investigation

Our efforts to develop a CNTD structural AlN material began with a parametric study of the most basic deposition chemistry. During this study we first examined the mechanics of the deposition equipment (AlCl_3 burner pot design, injector/mixer design, and a test specimen substrate search).

Following these mechanical adjustments, the deposition chemistry was systematically examined. The substrate temperature, the total pressure and the active gas ratios were examined.

IV-A.2a Equipment Adjustments

As discussed above, AlN deposition involves the in-situ generation of AlCl_3 by reacting aluminum metal with HCl. The efficient operation of this aluminum conversion process is extremely important to the AlN deposition. Unreacted excess HCl from an inefficient burner pot will react with ammonia to form Aluminum Ammonium Chloride contaminants.¹⁸

For an efficient aluminum burner pot we sought a proper balance between the pot temperature, the total pressure,

and the HCl concentration (HCl/diluent-gas flow ratio).

It is important to emphasize that we were restricted in many ways. If the conversion process should proceed too rapidly then local temperatures can rise sufficiently to fuse the aluminum granules and thereby restrict the continued flow of HCl through the pot. Furthermore, while the AlCl_3 conversion efficiency increases with increased pressure, the AlN deposition process proceeds more efficiently at lower pressures.

A suitable balance was found with the pot temperature maintained at about $425^\circ - 430^\circ\text{C}$ and the total pressure at about 50 torr. We made some attempts to operate at a higher pot temperature and pressure using an argon diluent flow through the pot, but these experiments only produced lower pot efficiencies and poorer AlN deposits.

Beyond the burner pot, the injector/mixer section must function properly. This section must be kept as short as possible, yet still achieve rapid and complete mixing of the AlCl_3 and NH_3 active gases. If the injector/mixer is made too long then lower temperature reactions are promoted and gas phase nucleation can result. If, however, it does not promote complete mixing, then a non-uniform active gas concentration results, local reaction rates become diffusion limited, and a non-uniform coating is produced.

The most important characteristic of the injector/mixer area is its temperature. This temperature should be as low as possible yet still high enough to maintain species

such as AlCl_3 and $\text{AlCl}_3 \cdot \text{NH}_3$ in the gas phase. We found that 450°C was the most appropriate temperature for this area.

A significant amount of attention was also devoted to a search for a suitable substrate material. The choice of substrate materials presented us with a dilemma. We needed a material with CTE close to AlN and also with mechanical properties suitable for bend testing.

The easiest and most reliable bend strength measurements are made using a relatively brittle substrate material with a low elastic modulus. During bend testing, a coated specimen made of such a material will develop the highest stresses in the coating (roughly by a factor equal to the ratio of elastic moduli) and failure of the coating will result in a catastrophic failure of the whole test specimen. Graphite would provide just such an ideal substrate if its thermal expansion characteristics were suitable.

At the time that these experiments were conducted, UT-22 had the closest CTE match with AlN of any graphite which we had available. (See Table 10). Our attempts to deposit on UT-22 (as well as HLM) graphite produced only cracked and spalled coatings. Strength measurements were impossible.

Another approach was to try to produce free-standing deposits of AlN for testing. In this case we attempted to deposit on to a single surface of a high CTE material and hoped that the substrate would shrink free upon cooling and leave the coating intact. Alumina and stainless steel

TABLE 10: Coefficients of Thermal Expansion for various substrate materials. ⁽¹⁹⁾

Material	CTE ($\times 10^{-6}/^{\circ}\text{C}$)
AlN	5.4 (to 1000 $^{\circ}\text{C}$)
Mo	5.6 (to 1000 $^{\circ}\text{C}$)
Sapphire (Al_2O_3)	8.3
UT-22 graphite (Ultra Carbon Corp.)	4.6
HLM graphite [†]	1.8/3.3
Stainless steel	19.5

[†] Anisotropic. Manufactured by Great Lakes Carbon Carbon Corp., Niagara Falls, N. Y.

were used with limited success. The coating usually developed microcracks, and was not suitable for strength measurements.

In principle, molybdenum substrates could allow us to deposit relatively thick coatings which might be tested as free-standing material by etching the substrate away. However, this is quite time consuming, and is impractical as a routine test. Molybdenum might also be used as a permanent substrate. Molybdenum closely matches AlN in CTE and produces adherent coatings with good integrity. However, measurements of coating strength are still very difficult to make on molybdenum substrates. Its mechanical properties are ill-suited for testing a thin AlN coating. Molybdenum has an elastic modulus close to that of AlN and its yield strength is nearly equal to the bend strength of AlN. However, it also has some ductility in contrast to AlN. These properties cause two problems during bend tests. The high substrate modulus produces high normal stress on the thin coatings at the load pins. Also, the relatively high strength and ductility of substrate would make the coating failure difficult to detect.

We attempted thick AlN deposits onto small diameter Mo filaments which might have solved the problem by approaching free standing AlN. However, residual stresses nearly always caused such specimens to crack and their surfaces were very bumpy which always presented problems during strength testing.

Thus, our bend tests proved unreliable and were not used as a guideline for AlN material development. Instead,

we relied on SEM evaluation of microstructure with some qualitative X-ray diffraction work. (See Table 11).

IV-A.2.b Deposition Parameters

The parameters most critical to the deposition process are generally the temperature and active gas concentration (pressure and mixture ratio). We began our search for CNTD conditions with an examination of the effects of these parameters.

The substrate temperature was examined in the range of 600°C to 1350°C. We found that the AlN deposition rate generally increased with temperature. Thermochemistry dictates that about 900°C (~1175°K) forms a lower limit below which a gaseous $\text{AlCl}_3 \cdot \text{NH}_3$ complex will be stable compared to AlN formation (See Appendix D). Generally, at any temperature from about 1000°C (1275°K) to 1300°C (1575°K) deposits would tend to become heterogenous and porous, with material nucleating in the gas phase and depositing as solid particulates.

Effects of total pressure on the deposit were less easily examined. While the deposition of AlN should be favored at lower pressures, the conversion of Al to AlCl_3 is more efficient at higher pressure. Calculations of the pressure effects on the aluminum conversion reaction suggested that reasonable efficiencies ($\geq 95\%$) could be obtained at 50 torr or greater. One experiment was conducted to ascertain the effect of higher pressures on the AlN deposit. The

TABLE 11 RESULTS OF X-RAY DIFFRACTION

Run No.	Substrate	
842	UT-22	Mixture of AlN and Al_2O_3 . The Al_2O_3 has a random orientation typical of powder. The AlN has a strong (110) orientation.
843	UT-22	AlN with a strong (110) orientation. Some $\alpha\text{Al}_2\text{O}_3$ is present.
844	UT-22	AlN with a strong (101) orientation. $\alpha\text{Al}_2\text{O}_3$ peaks present.
845	UT-22	AlN with a strong (101) orientation and strong (112) peak.
849	UT-22	AlN with a strong (112) orientation. Some $\alpha\text{Al}_2\text{O}_3$ present.
850	UT-22	AlN with a strong (112) orientation.
851	UT-22	AlN with a strong (112) orientation. Some impurity peaks of $\alpha\text{Al}_2\text{O}_3$ present.
853	UT-22	AlN with a strong (101) orientation.
854	UT-22	AlN with a strong (112) orientation. Strong (110) peak also present. $\alpha\text{Al}_2\text{O}_3$ peak present.
855	Sapphire	AlN with a strong (101) orientation. No impurities detected. A small residual compressive stress is indicated.
517	UT-22	AlN and Al_2O_3 . The material shows 2 equally strong peaks (101) and (103).
522	UT-22	AlN with a strong (101) orientation.
525	Molybdenum	AlN with a strong (103) orientation.
526	Molybdenum	AlN with a strong (103) orientation.
533	Molybdenum	AlN with a strong (103) orientation
533 A	Molybdenum	AlN with a strong (110) orientation
534	Molybdenum	AlN with a highly textured (110) orientation.
535	Molybdenum	AlN with a strong (103) orientation.

results of this experiment revealed that at higher pressures, NH_3 gas appeared to react with free HCl and AlCl_3 and formed aluminum ammonium chlorides which deposited on the graphite diffuser and stopped the flow of gas through the burner. The total pressure was then maintained at less than 100 torr through most of the program.

To this stage in our investigation we had characterized our specimens using microhardness, SEM, and a limited amount of XRD, EDAX and microprobe.

The EDAX consistently showed from 1.5 to 3.0 w/o chlorine content in our specimens. Microprobe revealed that the chlorine was usually associated with oxygen and XRD spectra showed the presence of $\alpha\text{Al}_2\text{O}_3$ and AlClO impurities.

Armed with these data we examined the effects of changes in the active gas ratio ($\text{NH}_3/\text{AlCl}_3$) on the deposit. As shown in Appendix D, AlCl_3 should react with NH_3 to form AlN above about 1000°C . We expected a high $\text{NH}_3/\text{AlCl}_3$ ratio to help reduce the oxygen and chlorine content by converting any AlClO that might form near the substrate.

We conducted several experiments of various $\text{NH}_3/\text{AlCl}_3$ ratios. Our results are portrayed especially well by one particular experiment in which the $\text{NH}_3/\text{AlCl}_3$ ratio was changed during the deposition.

The most significant result was the apparent relationship between the $\text{NH}_3/\text{AlCl}_3$ ratio and the deposit microstructure. Figure 37 shows three SEM micrographs of the

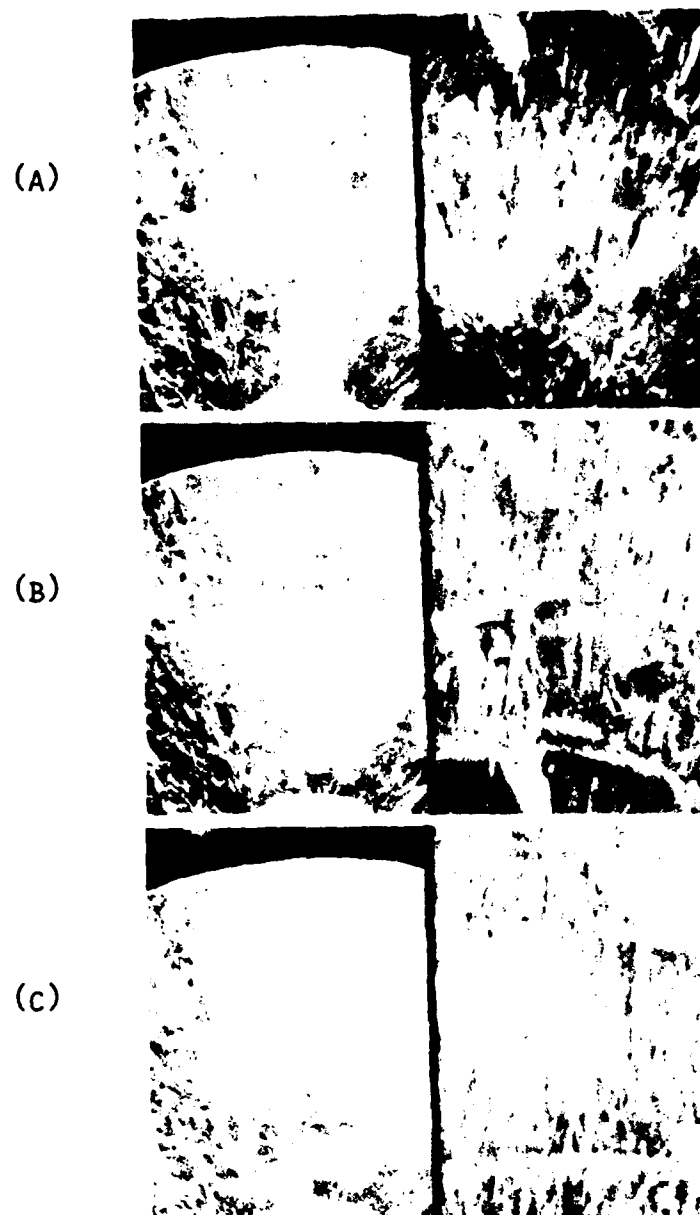


FIGURE 37: EFFECT OF INCREASING $\text{NH}_3/\text{AlCl}_3$ RATIO
ON THE MICROSTRUCTURE OF ALN;
LEFT: 80X, RIGHT: 400X.
(A) $\text{NH}_3/\text{AlCl}_3 = 0.75$, (B) $\text{NH}_3/\text{AlCl}_3 = 1.5$
(C) $\text{NH}_3/\text{AlCl}_3 = 2.25$

deposit which depict the fracture surface at three different locations within the deposit. From these micrographs it is evident that the apparent grain size decreased with increasing $\text{NH}_3/\text{AlCl}_3$. Clear bands of columnar fracture topography are evident which become finer away from the substrate where the ratio was increased. At the same time, the microhardness increased with increasing $\text{NH}_3/\text{AlCl}_3$ going from HV_{500} of 975 on the ID to 1900 near the OD. It seems that a higher $\text{NH}_3/\text{AlCl}_3$ ratio favors more complete conversion to AlN and also causes the balance between crystal growth rate and nucleation rate to shift toward greater nucleation.

IV-A.2.c General Materials Characterization

The core of our material characterization centered around SEM examination of the deposit. As mentioned above, the flexural strength measurements which we normally would have used as a guide, were unreliable and SEM examination served instead. Grain size had to be evaluated from SEM examination of exterior surfaces and cross sectioned fractured surfaces since we could not find suitable room temperature etchant to bring out the interior grain structure. We typically observed two types of surface topography, well-faceted crystallites and rounded, polycrystalline bumps. Examples of these surfaces are shown in Figure 38. Fracture surfaces usually appeared columnar such as that illustrated in Figure 39. The apparent grain size, judged from the features seen in both exterior surfaces and fracture surfaces

(A)



(B)

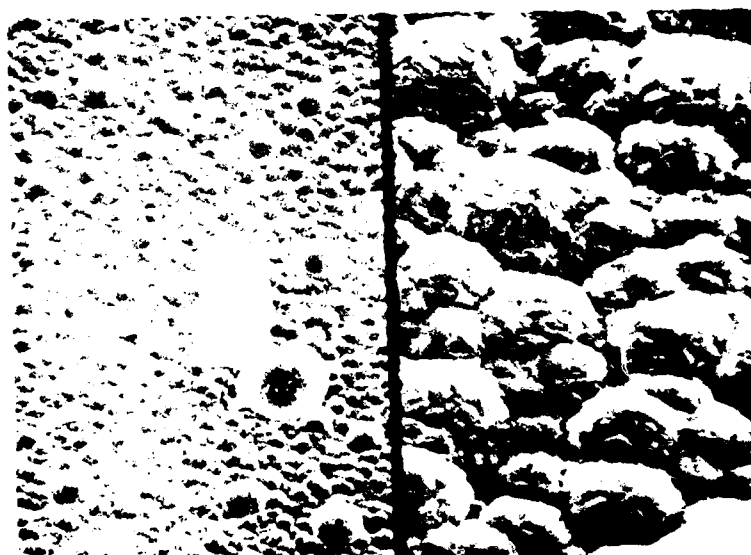


FIGURE 38:

CRYSTAL MORPHOLOGIES OF CVD ALN DEPOSITS

(A) WELL-FACETED CRYSTALLITES;
LEFT: 400X, RIGHT: 2000X

(B) ROUNDED CRYSTALLITES;
LEFT: 200X, RIGHT: 1000X

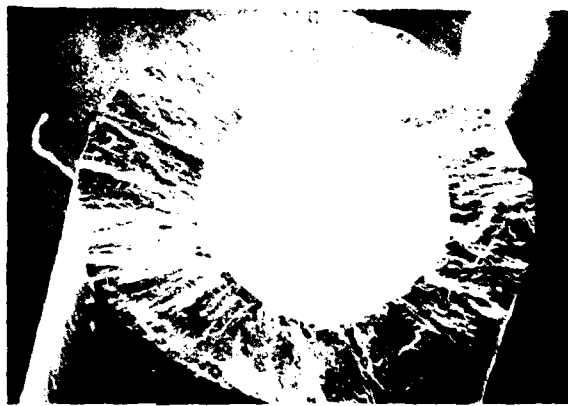


FIGURE 39: COLUMNAR CRYSTAL HABIT ON THE FRACTURE SURFACE OF A TYPICAL ALN DEPOSIT. THE SUBSTRATE IS A MOLYBDENUM FILAMENT; 40X.

were generally not very fine, most often characterized by dimensions greater than $10\mu\text{m}$.

We were unable, however, to establish any relationship between either the exterior surface morphology or the apparent grain size and the deposition parameters.

As noted above, some chemical analysis was conducted using EDAX and XRD. EDAX commonly detected chlorine in these deposits in levels of from 1.5 to 3.0 wt % and the XRD revealed Al_2O_3 and AlClO impurities in nearly all of the specimens which were examined. XRD also revealed some preferred orientation in the deposits. We commonly found the (110), (101) and (112) orientations somewhat preferred (crystalline planes oriented perpendicular to growth axis).

However, again we could find no consistent relationship between crystallographic orientation and deposition conditions.

Microhardness of the deposit was one of the major properties studied in relating process conditions to the material deposited. In the initial phase of the program, hardness was not measured because deposits were often too thin or cracked. However, when optimum conditions were established, the deposits consistently showed hardness values in the range of 1400 to 1700 HV_{500} . A few extreme values as high as 1950 HV_{500} and as low as 975 HV_{500} were also obtained. Increasing the $\text{NH}_3/\text{AlCl}_3$ ratio tended to increase the hardness of the deposit.

IV-A.3 Alloying Experiments

To this point in our investigation deposits had not shown the type of features which we associated with the CNTD mechanism (primarily microstructure). We therefore tried another approach. A series of experiments were conducted in which the AlN deposit was alloyed with another material such as Al_2O_3 or Si_3N_4 , through the introduction of oxygen or silicon respectively. We attempted, in these experiments, to ascertain if a solid solution of oxygen or silicon in AlN could be obtained or whether a binary deposit would result. In either case, we expected that some grain refinement would result due to the different kinetics of nucleation and growth of different species, i.e. each might disrupt the growth of the other.

The first experiments were carried out with the introduction of oxygen to the gas stream using either CO_2 , air, or H_2O . We sought to examine the effect of these additions on grain refinement. We found no effect of oxygen additions in any form on the grain structure of the deposit. Test results are given in Table 12.

We conducted a second set of alloying experiments in which we investigated the effects of codeposition of AlN and Si_3N_4 , first by adding small amounts of silicon to the AlN system (using trichlorosilane), and then by adding small amounts of aluminum trichloride to the Si_3N_4 system. These experiments produced much more interesting results than did

TABLE 12: Effect of oxygen additions on the properties of CVD AlN

Run #	Source of O ₂ *	Hardness HV ₅₀₀ (kg/mm ²)	+Chemical Composition, w/o				Remarks
			Al	N	Si	Cl	
639	CO ₂	1545	60.16	35.17	0.06	4.1	AlN with small amount of Al ₂ O ₃
640	CO ₂	1560	57.63	39.17	0.20	3.0	Major XRD peaks of AlN - minor peaks of Si, Si ₂ ON, SiO ₂ or Al ₂ O ₃
641	CO ₂	1495	56.43	39.96	0.00	3.6	AlN - one peak of α-Al ₂ O ₃ (XRD)
642	H ₂ O+ Air	1275	63.06	35.46	0.10	1.5	All peaks of AlN (XRD)
643	H ₂ O	-	Very thin deposit due to inefficient Al pot.				
644	H ₂ O	-	64.3	33.23	0.00	2.5	Major XRD peaks of AlN - small amounts of Al ₂ O ₃ may be present

* See Table A-6, Appendix A for deposition parameters.

+ Energy-dispersive analysis. Nitrogen by difference.

those concerning oxygen additions to AlN. A competitive deposition between AlN and Si_3N_4 was observed and found to produce significant grain refinement.

In the case of silicon additions to the AlN system, we found that the coating microstructure was quite sensitive to the deposition conditions. That the proper balance in deposition conditions should prove delicate is not too surprising since a balance was sought between two competing deposition chemistries, instead of just one. As one might expect changes in the substrate temperature and active gas ratios had significant effects.

Figure 40 illustrates a specimen which resulted from a deposition run in which the substrate temperature was allowed to shift. Several layers of quite varied morphology are evident.

Figure 41 demonstrates the kind of finely banded structure which could be achieved when an appropriate balance was maintained. The sample was etched in a CrO_3/HF electrolytic bath at 70°C for several minutes to delineate the banding. Bands appear fairly coarse near the substrate but get very fine towards the outer edge. Separation between bands near the outer edge was measured to be $\sim 0.2\mu\text{m}$. Since the CrO_3/HF should not have been so effective against Si_3N_4 , this refinement of structure and absence of columnar crystal habit suggested the possibility of competitive deposition of AlN and elemental silicon. Table 13 lists



FIGURE 40: DEPOSIT OF ALN SHOWING A NON-HOMOGENEOUS INCORPORATION OF SILICON "DOPANT"; 1000X.



FIGURE 41: MICROSTRUCTURE OF SILICON-DOPED ALN
DEPOSIT ELECTROLYTICALLY ETCHED IN A
 CrO_3/HF SOLUTION, SHOWING THE BANDED
STRUCTURE OF ALN;
LEFT: 1000X, RIGHT: 5000X

TABLE 13: Effect of silicon additions on the properties of CVD AlN

Run #	Source of Si*	Hardness HV ₃₀₀ ² kg/mm ²	+Chemical Composition w/o				Remarks
			Al	N	Si	Cl	
645	SiHCl ₃	1930	57.5	34.4	4.6	3.5	AlN with small amounts of Si ₃ N ₄ - Presence indicated by XRD
646	SiHCl ₃	1465	63.2	33.6	1.3	1.9	
647	SiHCl ₃	No analysis carried out					
648	SiHCl ₃	No analysis carried out					
649	SiHCl ₃	No analysis carried out					
650	SiHCl ₃	No analysis carried out					
651	SiHCl ₃	No analysis carried out					

* See Table A-7, Appendix A for deposition parameters.

+ Energy-dispersive analysis. Nitrogen by difference.

some other results of these experiments.

We also performed experiments in another region of relative concentrations, in which aluminum was added in small amounts to the Si_3N_4 deposition system. (See Table 14). A portion of this work, conducted under the auspices of Naval Air Command for the development of CNTD Si_3N_4 , was reported earlier.²⁶ The resulting grain refinement was even more pronounced than that which occurred with silicon additions to AlN. Figure 42 demonstrates the difference between the fracture surface of a normal, columnar Si_3N_4 deposit and that of a specimen produced by aluminum additions. Electron microprobe analysis provided a dramatic display of the competitive interplay between AlN and Si_3N_4 . Figure 43 shows two elemental distribution maps produced by microprobe, one of aluminum and one of silicon, taken of identical regions of a sample deposit. The important feature of Figure 43 is the complimentary distribution of aluminum and silicon which demonstrates the competitive nature of the deposition process. This feature is even more vividly displayed in Figure 44 by a line scan of the same region shown in Figure 43.

IV-B Characterization of Electrical, Thermal and IR Properties

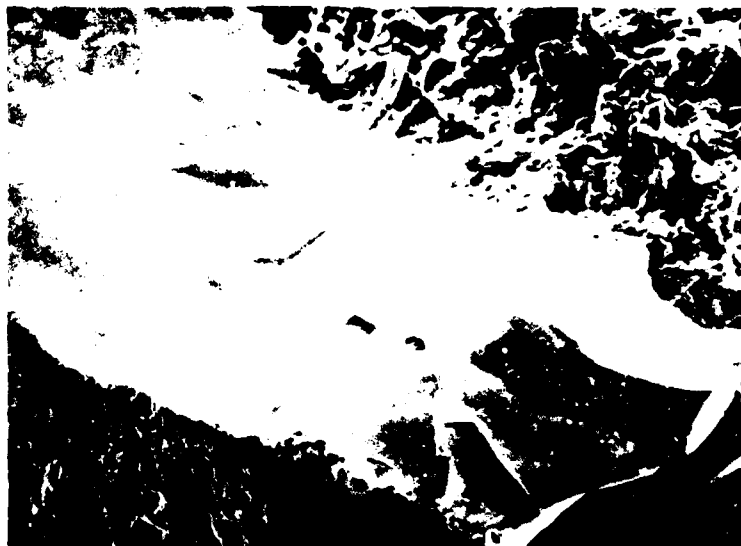
CVD AlN offers some significant potential for use in some electronic or electro-optic applications. A relatively high dielectric constant and concomitant high thermal conductivity offers a potential replacement for BeO in microwave

TABLE 14: Effect of aluminum addition on the properties of CVD Si_3N_4 *(20)

Run #	Pressure Torr	Substrate Temp. °K	Deposition Rate um/hr	HV kg/mm ² (Load)	K_C MPa·m	TRS MPa (ksi)	Remarks
652	65	1600	100	3255 (100)	-	376 (55)	Non-uniform deposit morphology from top to bottom, from the crystallites to coarse faceted crystals.
653	65	1625	-	2960 (200)	-	158 (23)	same as above.
654	65	1595	-	-	-	290 (42)	Glassy deposit with rounded domes and areas of faceted crystallites. Poor adhesion and integrity.
655	65	1590	-	3410 (100)	-	-	Fine grained deposit with rounded domes on the surface.
656	65	1590	-	2560 (500)	-	129 (19)	Amorphous type deposit with microcracks.
657	65	1585	250	2330 (500)	4.9	-	Translucent deposit with fine grained domes on the surface.
658	90	1595	-	2320 (200)	3.2	-	Dark shiny deposit with domes. Fracture surface appears glassy, non-columnar.
659	90	1590	-	-	-	-	Fine-grained, columnar deposit.
660	50	1420	-	-	-	-	Whitish amber deposit on top, dark at the bottom, appears glassy in fracture.
661	62	1425	-	-	-	-	same as above.

* See Table A-7, Appendix A for deposition parameters.

(A)



(B)

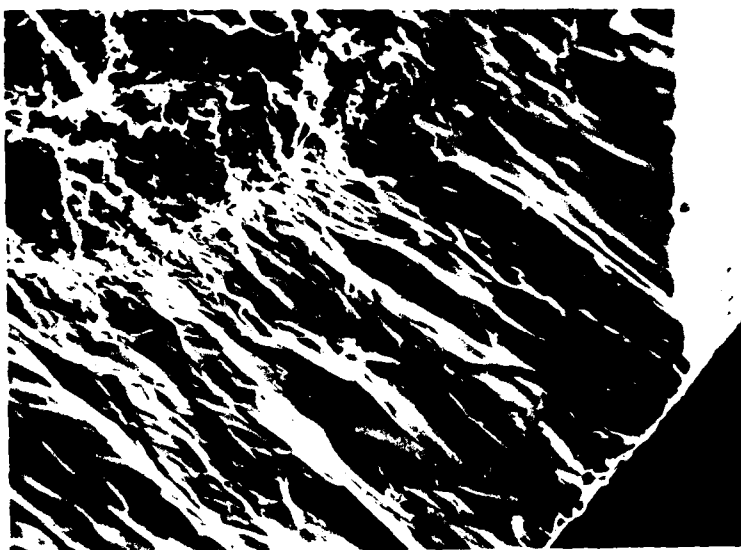


FIGURE 42: FRACTOGRAPHS SHOWING THE EFFECT OF "DOPING" ON THE CRYSTAL MORPHOLOGY.

(A) FINE-GRAINED, NON-COLUMNAR DEPOSIT OF Si_3N_4 "DOPED" WITH ALUMINUM; 200X

(B) TYPICAL CVD Si_3N_4 DEPOSIT SHOWING COLUMNAL CRYSTAL GROWTH; 200X

(A)



(B)

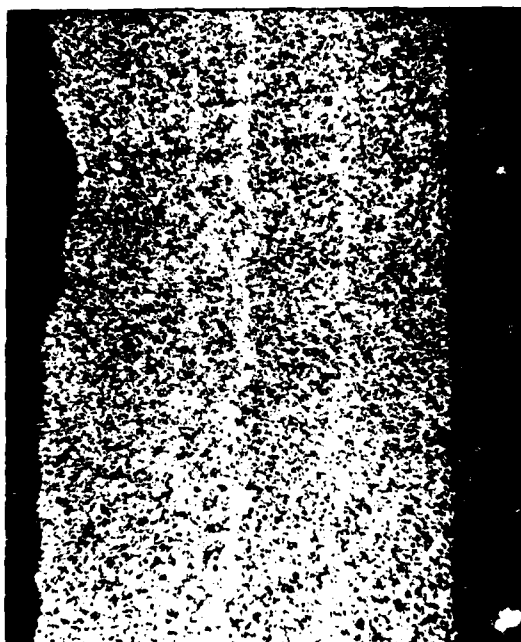


FIGURE 43: X-RAY ELEMENTAL DOT MAPS FOR SILICON-DOPED ALN DEPOSIT.

- (A) DOT MAP FOR SILICON. DARK BANDS INDICATE DECREASE IN SI CONTENT; 500X
- (B) DOT MAP FOR ALUMINUM. NOTE THE CORRESPONDENCE OF THE WHITE BANDS SHOWING INCREASED AL CONTENT TO THE BANDS IN UPPER PHOTOGRAPH; 500X

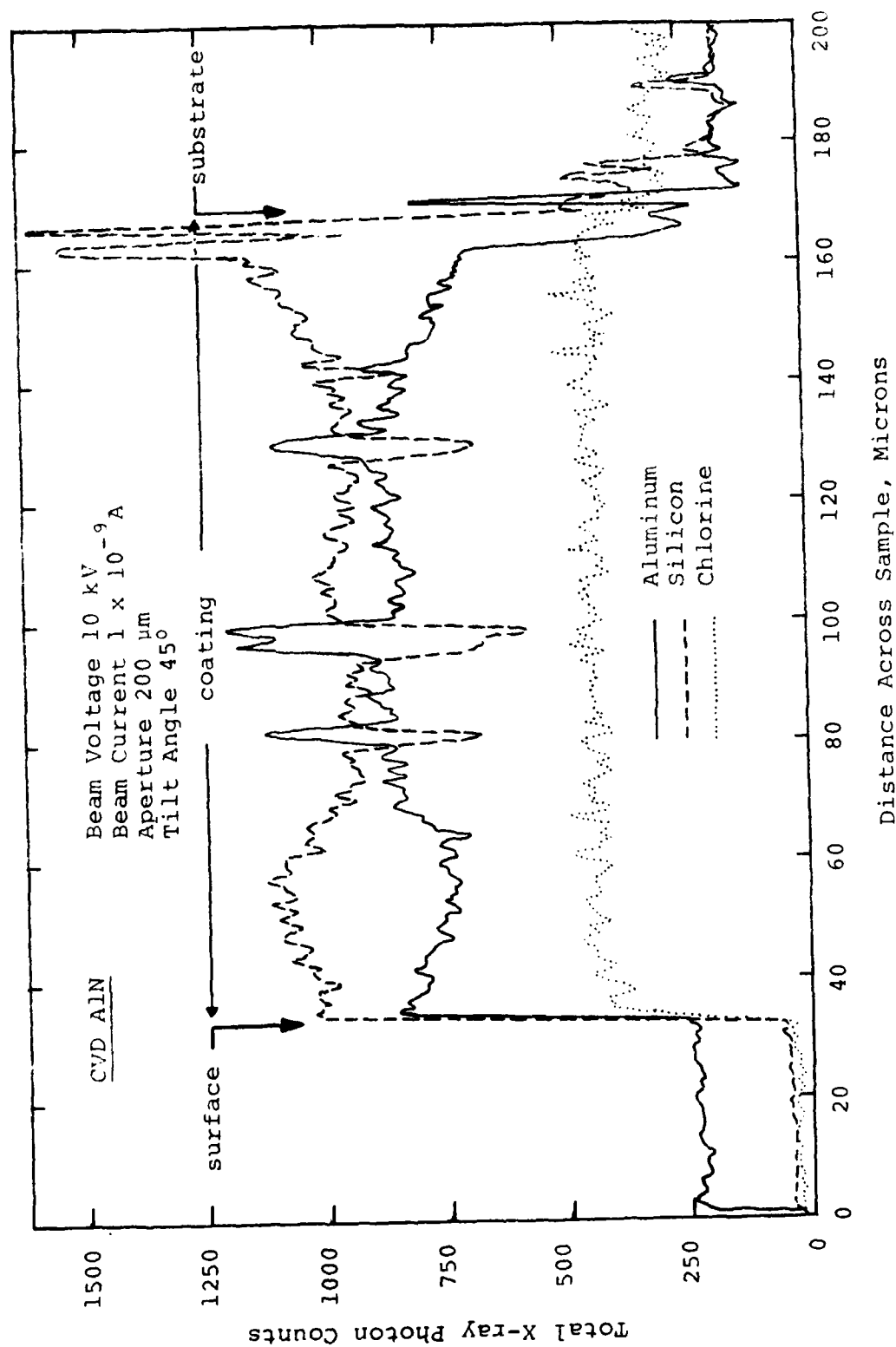


FIGURE 44: X-RAY LINE SCAN THROUGH THE CROSS-SECTION OF CVD ALN "DOPED" WITH SILICON SHOWING THE DISTRIBUTION OF AL, SI AND RESIDUAL CHLORINE IN

devices. Since BeO presents serious health hazards, this potential is attractive. Good transmittance properties might qualify CVD AlN as an IR window material. In either case, the CVD process offers a manufacturing method with potential advantages.

As such, we devoted some effort to the characterization of some electrical, thermal and IR properties of the CVD AlN produced during this program.

IV-B.1 Equipment and Procedures

The AlN deposition chamber which we used to deposit differed from the earlier system in the heating method. Figure 45 illustrates the system that was used to deposit specimens for IR quality AlN. For these experiments, the molybdenum substrates were heated by direct induction to the specimen. A disc shape was centered inside a 64 mm diameter quartz chamber. An induction coil surrounded the quartz chamber and was centered vertically on the specimen to be coated. Molybdenum discs (25.4 mm dia.) were chosen as substrates because they yielded crack-free material and could be dissolved in acid without noticeable effect on the AlN deposit. One disc was deposited per run.

A liquid nitrogen trapped Kinney mechanical vacuum pump provided exhaust vacuum down to about 1 Torr. Other details of the equipment were similar to that described above in Section IV-A.1.

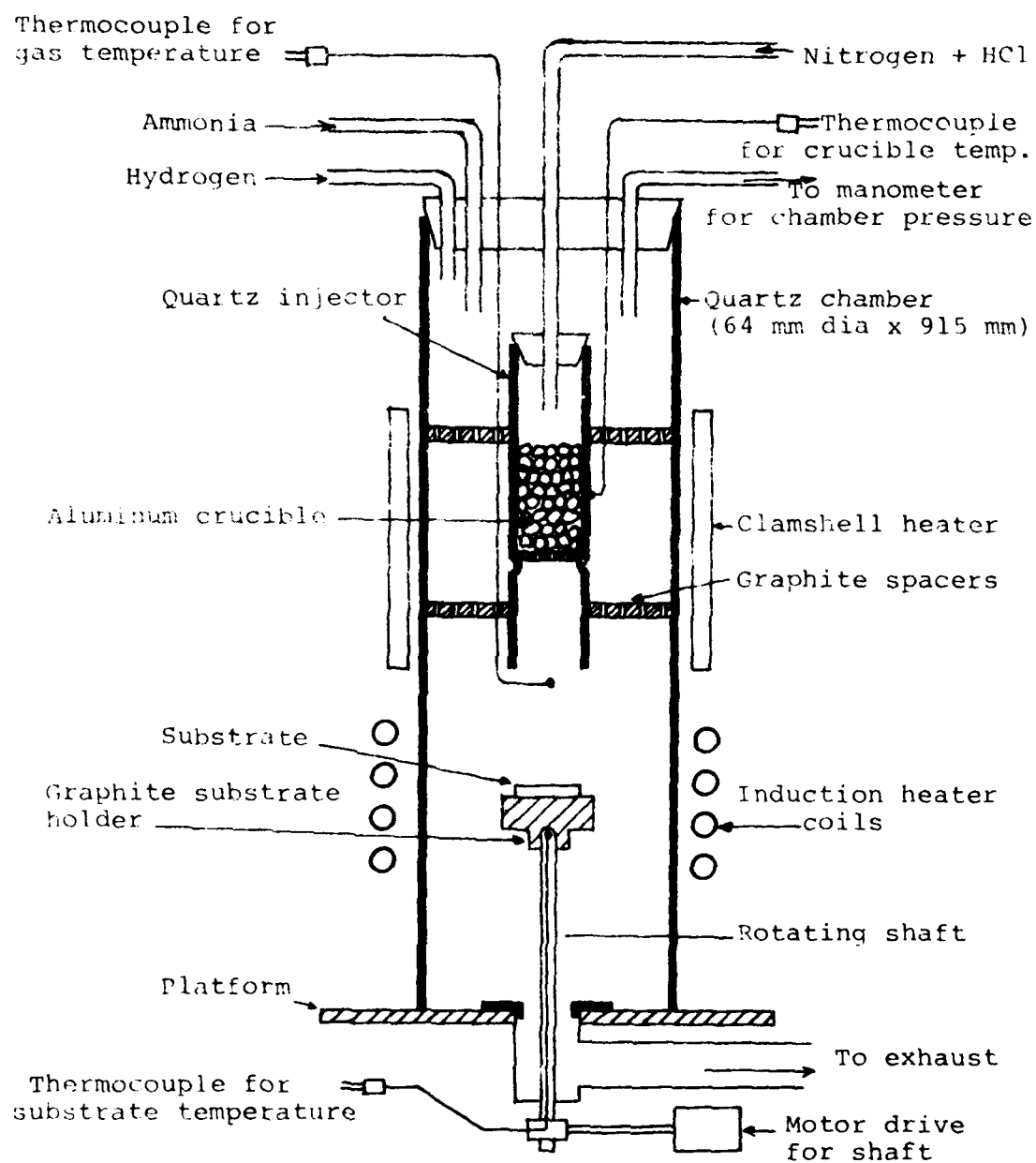


FIGURE 45: SCHEMATIC OF ALN DEPOSITION APPARATUS USING INDUCTION HEATING.

IV-B.2 Electrical Properties

The results of the electrical measurements are shown in Figures 46 to 48. For comparison, published data on CVD AlN made from $\text{AlCl}_3 \cdot \text{NH}_3$ complex are included.¹⁸

We should note that we observed a significant variation between specimens in their measured electrical properties. Since we have also observed a fairly large degree of chlorine contamination in some of our specimens (up to 4%), the properties shown in Figure 46 through 48 should not be taken to reflect pure AlN.

The electrical properties of AlN were measured by a guarded 3 terminal technique using a General Radio 1615A capacitance bridge. The schematic sketch of the circuit is shown in Figure 49.

The specimen geometry was essentially a parallel plate capacitor with the graphite substrate acting as one of the electrodes. The deposit surface was metallographically polished and a 200 Å film of Au/Pd alloy was deposited on the surface to prevent absorption of oxygen. A silver paste electrode was then applied. After attaching the lead wires to the silver paste, the assembly was baked at 200°C for about 2 hours. Capacitance and conductance were measured as a function of frequency in the range 100 to 10^5 Hz at room temperature, and for one sample, also at 200°C. The ac conductivity, dielectric constant and the loss tangent were calculated and plotted as functions of frequency. The

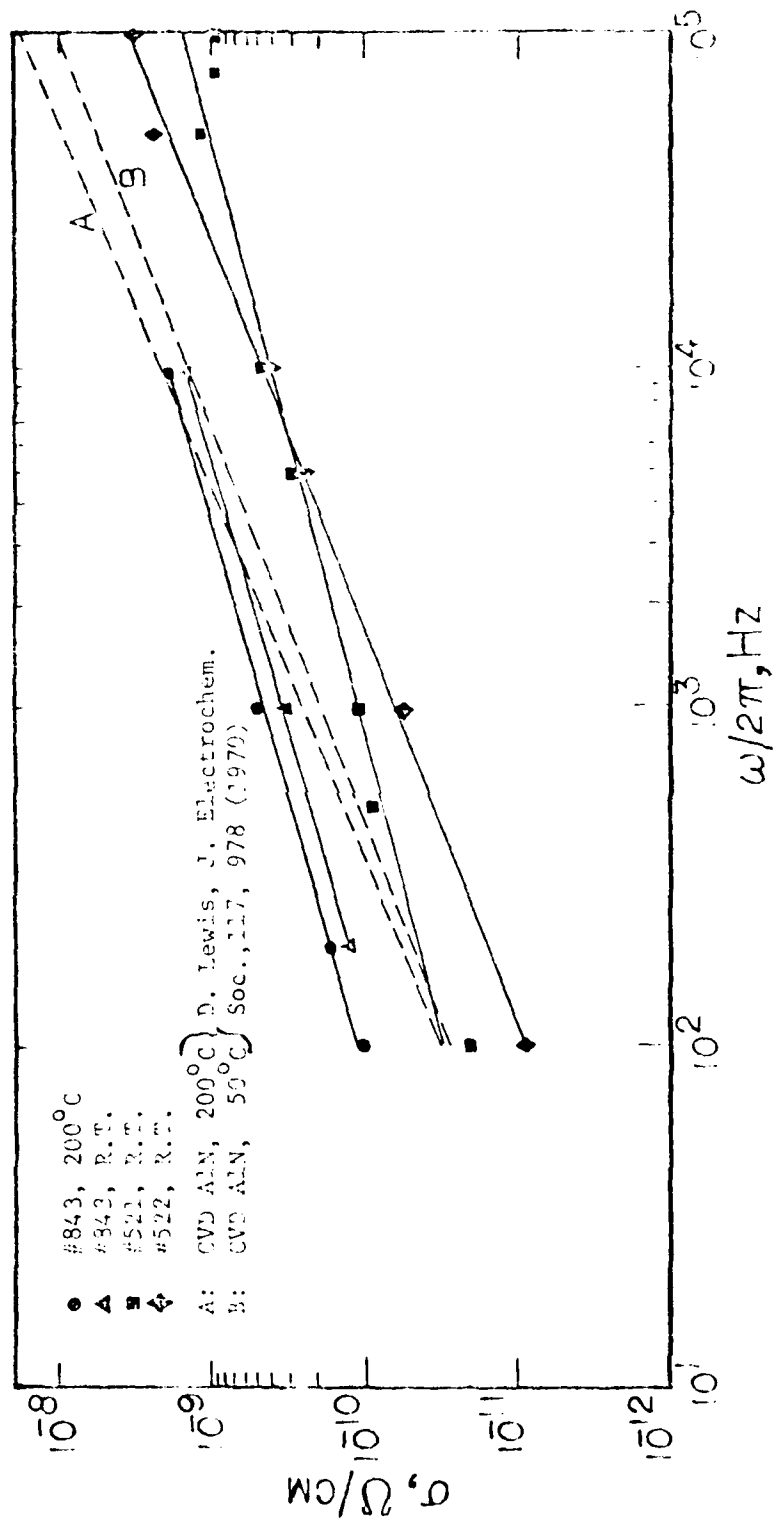


FIGURE 46: ELECTRICAL CONDUCTIVITY OF CVD ALN AS A FUNCTION OF FREQUENCY AND TEMPERATURE.

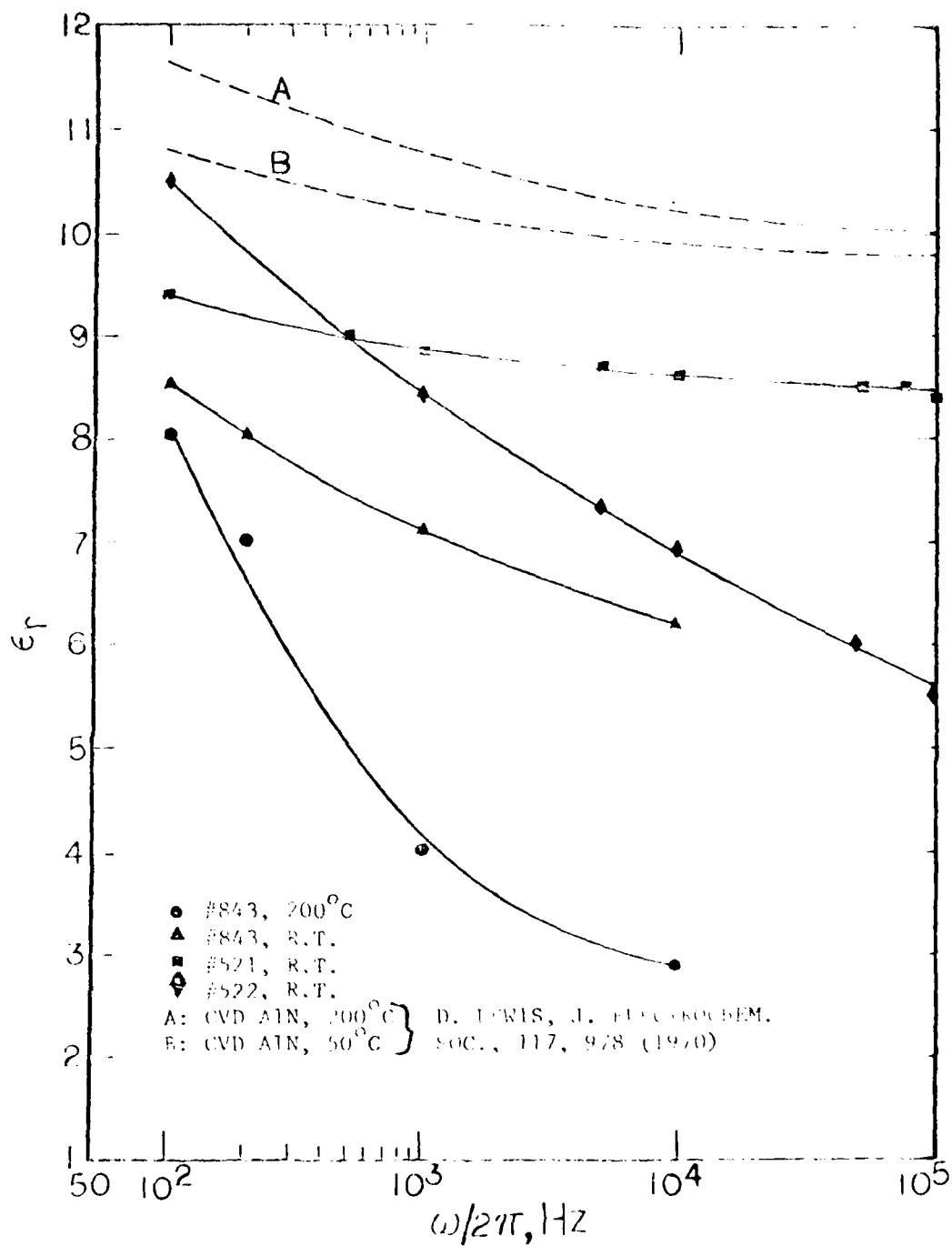


FIGURE 47: THE VARIATION OF DIELECTRIC CONSTANT AS A FUNCTION OF FREQUENCY AND TEMPERATURE FOR CVD ALN.

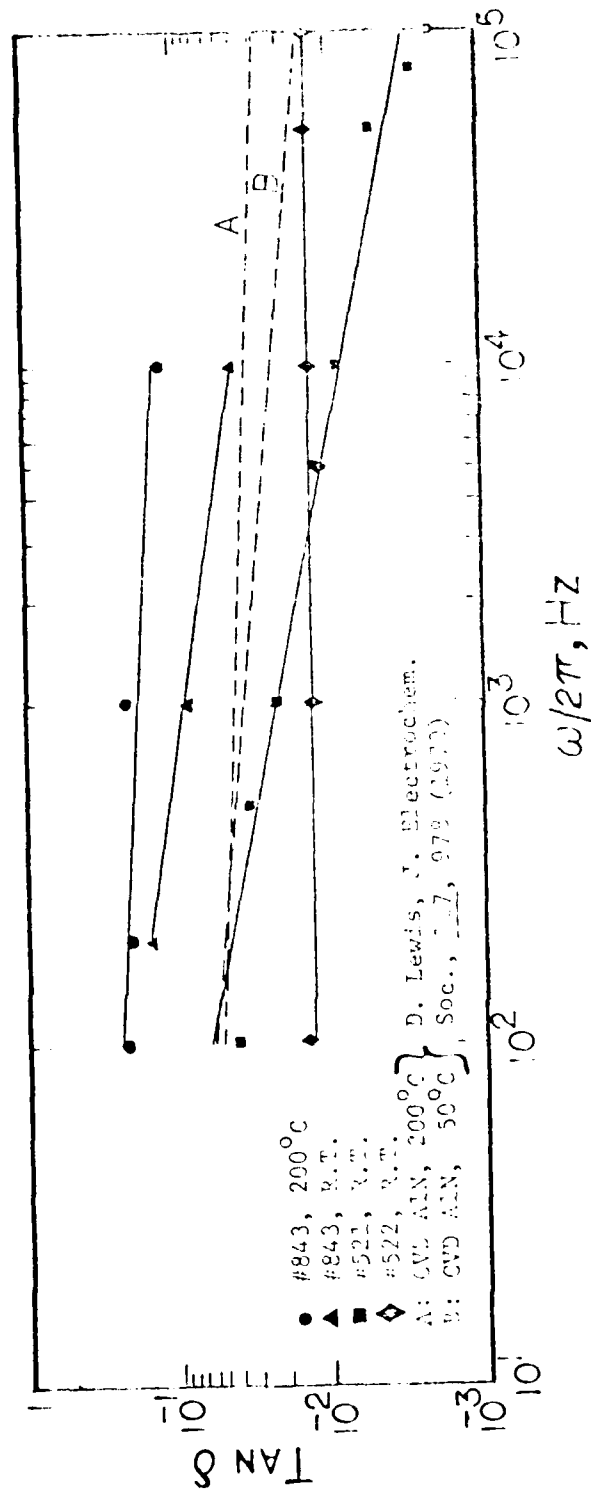
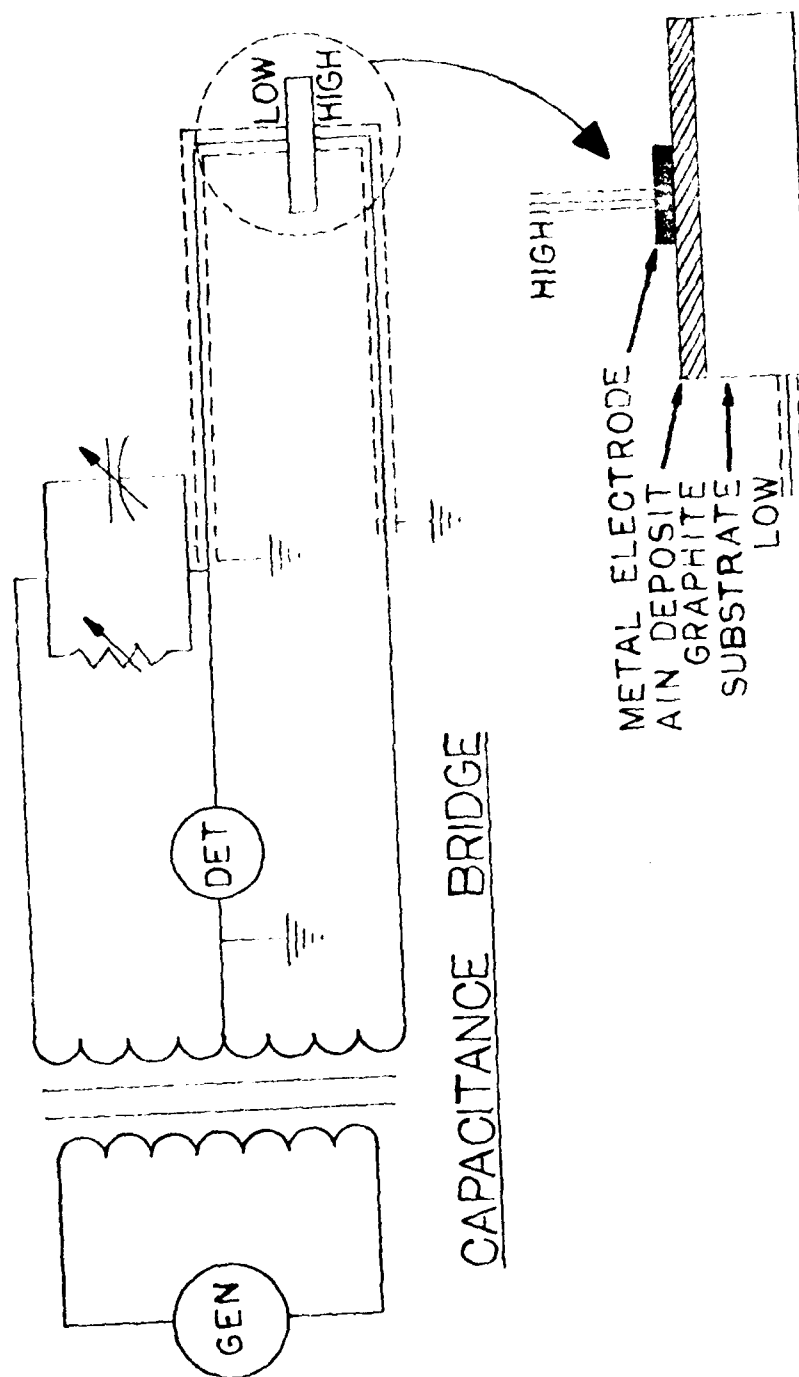


FIGURE 48: THE VARIATION OF LOSS TANGENT AS A FUNCTION OF FREQUENCY AND TEMPERATURE FOR CVD ALN.



CAPACITANCE BRIDGE

FIGURE 49: SCHEMATIC ARRANGEMENT OF APPARATUS USED FOR THE MEASUREMENT OF ELECTRICAL PROPERTIES OF CVD ALN.

dc conductivity was measured on two samples, using a Keithley 610C electrometer, having an input impedance of $10^{14} \Omega$. These two specimens had conductivity values of $1.3 \times 10^{-13} (\Omega\text{cm})^{-1}$ and $5 \times 10^{-14} (\Omega\text{cm})^{-1}$.

IV-B.3 Thermal Conductivity Measurements*

The AlN samples used for thermal conductivity measurements were coated with a thick layer of graphite to eliminate direct transmission of radiated energy during the pulse. The technique involved application of a short duration laser heat pulse to one surface of the 12.7 mm diameter disc specimen. The pulse transport time through the disc thickness was measured to evaluate thermal diffusivity. The thermal diffusivity of AlN was measured as a function of temperature in the range of room temperature to 300°C .

The results are shown in Figure 50 along with data for several other AlN materials published in the literature. The present data are subject to an error of $\pm 15\%$ and $\pm 10\%$ for samples 534 and 535 respectively. One source of error was the thickness of the sample. For example, sample #534 was only $250 \mu\text{m}$ thick and the heat pulse transverse time was less than 2 ms, preventing accurate measurements below about 500°K . On the other hand, the heat pulse traverse time for

*Measurements carried out by Mr. John Lagedrost, FMI, Inc., Beddefore, Maine.

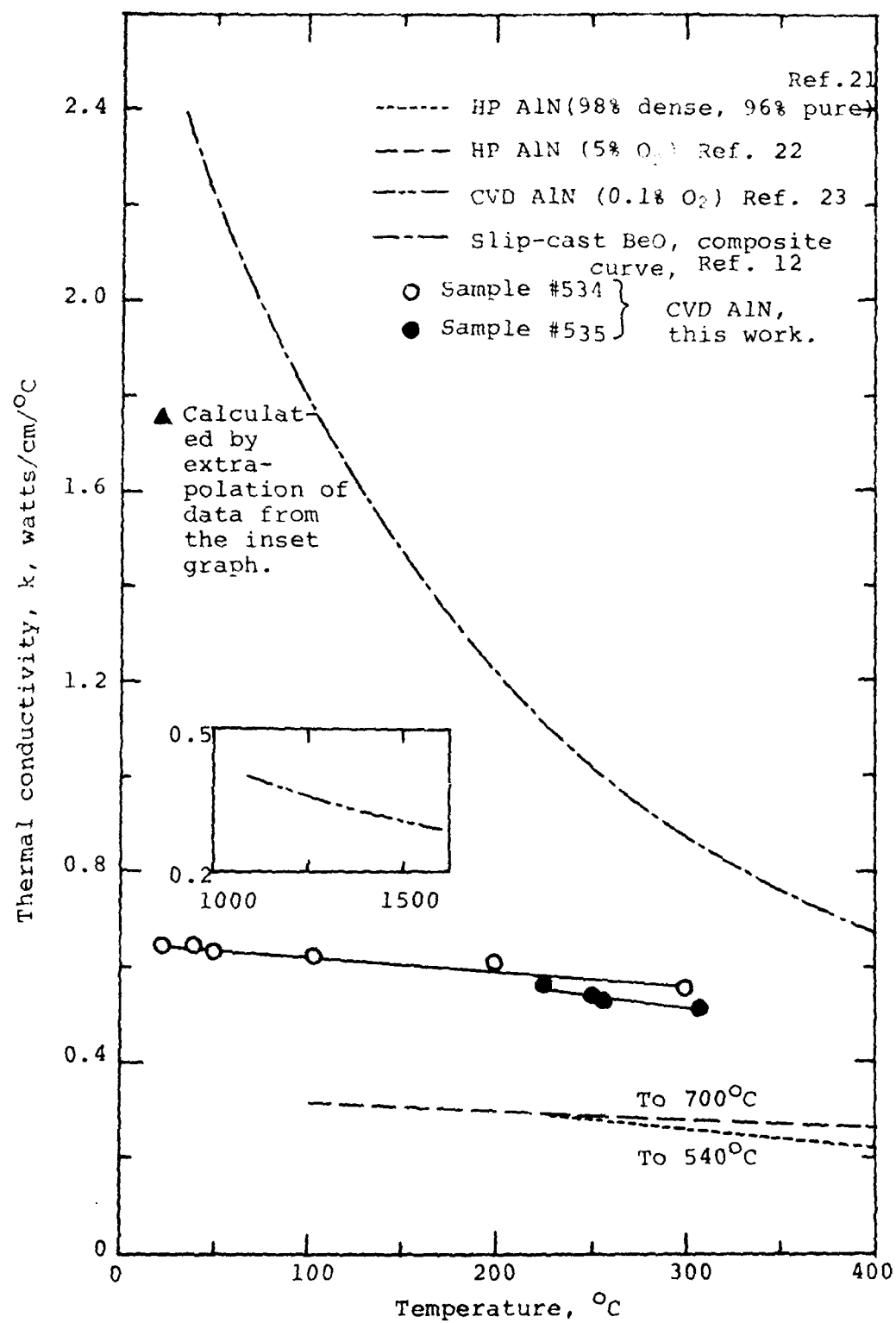


FIGURE 50: VARIATION OF THERMAL CONDUCTIVITY WITH TEMPERATURE OF VARIOUS ALN MATERIALS.

sample #535 (thickness 635 μm) was less than 10 ms, permitting a somewhat more accurate measurement.

The thermal conductivity data are consistent with the literature with respect to the temperature effect. The low value of α was probably due to the presence of impurities in the material although it was better than hot pressed AlN.

IV-B.4 IR Transmission

Specimens from runs 1 to 16 (Table 2a, Appendix A) were tested for IR Transmittance. It is important to notice that these runs were conducted at low pressure in an attempt to eliminate chlorine impurities by encouraging the stability and removal of gaseous HCl wastes. The deposits were removed from the molybdenum substrate using an acid etch. The 25.4 mm diameter discs of AlN were then metallographically polished. Eleven samples were tested for infrared transmission using a Beckman Model 4600 Infrared Spectrophotometer at University of Southern California. None demonstrated a good degree of transmittance. The transmittance levels varied from immeasurably small to a maximum of about 13%. The shape of the transmittance spectrum indicated that most of the losses were due to scattering. This observation indicated that either the deposited AlN was pure but fine-grained and unoriented, or that it was composed of more than one phase and probably had segregated impurities. Other data tend to support the latter explanation. Microprobe analysis has shown a significant chlorine and oxygen contamination, and

ammonium-aluminum-chloride salts are quite likely. XRD has shown preferred AlN orientation. It is, therefore, quite reasonable to conclude that the specimens which were tested had a significant amount of segregated impurities which acted as scattering centers.

IV-B.5 Acid Etch Tests

Tests were conducted on deposits of AlN to evaluate the chemical resistance of the material to two acid solutions. The information from these tests was useful in determining the method for removing the molybdenum substrate from the AlN discs made for transmission studies. Samples of AlN were subjected to a chemical attack by two acid solutions (50% HNO_3 in water and 25:25:50 $\text{HF}:\text{HNO}_3:\text{H}_2\text{O}$) at room temperature for 1 and 3 hours.

The samples were metallographically polished and weighed accurately on a microbalance. The change in weight was recorded after exposure, and the surface of the samples were examined in the SEM.

These tests revealed that AlN was fairly resistant to attack by 50% HNO_3 . The samples tested showed only about 1.5% weight gain after 1 hour exposure to this solution. In a solution of 25% HF , 25% HNO_3 and 50% water, the samples showed a weight loss after 1 hr., but after 3 hrs. there was a weight gain of about 4-6%. Examination of surfaces and cross sections in the SEM revealed that there was no discernible change in the surface appearance of samples after 1 hour

exposure to either solution, but after the 3 hour exposure there was some indication of a reaction. Some of the samples showed some attack when the fracture section was examined. Since the overall resistance to attack of the deposit was adequate for the removal of the substrate, the tests were concluded at this time.

IV-C. Summary of AlN Work

Our AlN efforts were directed toward two separate objectives: (a) development of CVD methods for grain refinement in AlN for improved structural properties and (b) development of AlN with good electro-optical properties.

Efforts directed toward the production of fine grained AlN found little evidence of grain refinement by normal deposition techniques. Our efforts have, however, shown good results with Si doped AlN. Codeposition of Si_3N_4 with AlN demonstrated substantial grain refinement as the nucleation of one codeposition compound apparently interrupted the growth of the other. Grain structure of some doped specimens showed at least an order of magnitude improvement over the conventional CVD AlN material. Values for associated strength improvements were not obtained due to problems with substrate compatibility. A suitable substrate should be found and the fine-grained doped, AlN material should be further evaluated.

Efforts to deposit pure, oriented, large grained AlN have proven quite difficult. The elimination of impurities

(principally Cl, O and Si) was most difficult. High vacuum (·2 Torr) experiments failed to remove chlorine as hoped. A cleaner and tighter CVD reactor system than what we used is undoubtedly required. Measurements of electrical and thermal properties were made. Low temperature thermal conductivity was low compared with BeO, but was still twice the values listed for hot pressed AlN (5% O₂). While electrical conductivity and dielectric loss tangent values were comparable to those reported for CVD AlN, the measured dielectric constant decreased with temperature in contrast to the reported behavior of other CVD AlN. IR transmission data gave some evidence for segregated second phase impurities.

APPENDIX A

DEPOSITION RUN CONDITIONS

FOR CNTD SiC

AND CVD ALN

TABLE A-1: Deposition Parameters for CNTD SiC using SiCl₄
and MTS as silicon sources

Run #	Ar	Gas Flow rates, ml/min					Press. Torr	Gas Temp °C	Pot Temp °C	Substrate Temp °C
		H ₂	SiCl ₄	MTS	CH ₄	C ₂ H ₆ O				
537	1430	2500	250	-	-	100	250	665	-	1200*
538	1430	2500	-	500	-	100	240	690	-	1200*
539	2000	300	-	600	-	-	250	650	-	1110
540	2000	300	-	600	-	-	250	690	-	1080
541	2000	300	-	600	-	-	250	673	-	1115
542	500	300	300	-	-	-	230	-	1500	960
543	1000	300	300	-	-	-	220	-	1500	990
544	1000	300	300	-	-	-	235	-	1500	995
545	1000	-	500	-	-	-	240	-	1240	1100
546	1000	-	500	-	-	-	250	-	1200	965
547	1000	-	500	-	100	-	360	-	1175	950
548	1000	-	500	-	50	-	360	-	1210	965
549	1000	-	500	-	50	-	360	-	1225	965
550	1000	-	500	-	75	-	350	-	1175	980
551	1000	-	500	-	75	-	250	-	1330	1110*
552	1000	-	500	-	75	-	350	-	1325	1110*
553	1500	-	500	-	75	-	350	-	-	1035*
554	1500	-	500	-	75	-	350	-	1300	1200*
555	1500	-	500	-	-	-	360	-	1320	1200*
556	1000	500	500	-	-	-	350	-	1400	1200*
557	1000	500	500	-	-	-	360	-	1550	1240*

TABLE A-1 Continued: Deposition Parameters for CNTD SiC using SiCl₄
and MTS as silicon sources

Run #	Ar	Gas Flow rates, ml/min					Press. Torr	Gas Temp °C	Pot Temp °C	Substrate Temp °C
		H ₂	SiCl ₄	MTS	CH ₄	C ₂ H ₆ O				
558	1000	500	500	-	-	-	250	-	1600	1150*
559	Run abandoned due to equipment problems									
560	1000	-	500	-	-	-	360	-	1350	885
561	2000	300	-	600	-	-	330	660	-	1090
562	2000	300	-	600	-	-	330	655	-	1085
563	2000	300	-	600	-	-	330	645	-	1125
564	2000	1200	-	600	-	-	330	666	-	1090
565	2000	1200	-	600	-	-	330	673	-	1085
566	2000	1200	-	600	-	-	330	678	-	1074
567	1000	-	500	-	-	-	325	-	1450	1180*
568	1000	-	500	-	-	-	320	-	1625	1270*
569	Run abandoned due to equipment problems									
570	2000	1200	-	600	-	-	320	-	1250	1140*
571	2000	1200	-	600	-	-	330	-	1250	1145*
572	2000	1200	-	600	-	-	350	-	1260	1150*

*Furnace temperature. Substrate was typically 50-150°C cooler than the furnace.

TABLE A-2: Deposition Parameters for CNTD SiC using propane and MTS

Run #	Gas Flow rates, ml/min				Pressure Torr.	Gas Temp. °C	Substrate Temp. °C
	Ar	H ₂	MTS	C ₃ H ₈			
662	2145	2400	800	-	320	625	1120*
663	4145	2400	800	-	325	625	1120*
664	4145	2400	800	-	320	610	1120*
665	4145	2400	800	-	290	795	1040*
666	4145	2400	800	-	290	825	1045*
667	4145	2400	800	-	290	785	1045*
668	4145	2400	800	-	250	850	1045*
670	1000	3375	250	-	230	655	1140
671	1000	3375	250	-	230	500	1115
672	1000	3375	250	-	230	550	1135
673	1000	3375	250	-	230	556	1150
674	1000	3375	250	-	230	680	1190
675	1000	3375	250	-	230	680	1210
676	1000	3375	500	-	230	660	1190
676A	1000	3375	500	-	230	640	1200
677	1000	1680	250	-	230	790	1180
678	1000	1680	250	-	230	840	1190
679	1000	1680	250	40	230	800	1205
680	1000	3375	250	40	230	705	1230
681	1000	3375	250	80	230	700	1225
682	1000	4500	250	80	230	755	1235

TABLE A-2 Continued: Deposition Parameters for CNTD SiC using propane and MTS

Run #	Gas Flow rates, ml/min				Pressure Torr.	Gas Temp. °C	Substrate Temp. °C
	Ar	H ₂	MTS	C ₃ H ₈			
683	1000	3375	250	60	230	780	1235
684	1000	3750	250	60	230	705	1235
685	1000	3750	250	60	230	785	1235
686	1000	3750	250	60	230	770	1235
687	1000	3750	250	60	230	800	1240
688	1000	3750	250	60	230	690	1240

*Furnace Temperature. The part temperature was typically about 100°C lower.

TABLE A-3: Deposition parameters for CVD SiC using C_3H_8 and CH_4
as carbon sources

Run #	Gas Flow rates, ml/min					Pressure Torr.	Gas Temp. ° C.	Substrate Temp. ° C.
	Ar	H_2	MTS	C_3H_8	CH_4			
689	1000	3750	250	-	60	230	800	1230
690	1000	3750	250	-	180-360	230	905	1250
691	1000	3750	250	-	360	230	895	1235
692	1000	3750	250	-	550	230	885	1250
693	1000	3750	250	-	1000	230	840	1250
694	1000	3750	250	-	1000	230	835	1250
695	1000	3750	250	-	1000	225	-	1230
696	1000	3750	250	-	700	230	835	1230
697	1000	3750	250	-	550	230	800	1235
698	1000	3750	250	-	450	230	890	1260
699	1000	3750	250	-	450	230	815	1260
700	1000	3750	250	-	450	230	790	1260
701	1000	3750	250	19-60	-	230	785	1240
702	1000	3750	250	60	19	220	795	1240
703	1000	1875 -3750	125 -250	19-60	19	220	794	1240
704	1000	1875 -3750	125 -250	19-60	-	220	675	1120
705	1000	5625	375	-	-	220	675	1130
706	Run abandoned due to equipment problem.							
707	1000	5625	375	-	-	220	750	1130

TABLE A-3 Continued: Deposition parameters for CNTD SiC using

 C_3H_8 and CH_4 as carbon sources

Run #	Ar	Gas Flow rates, ml/min				Press- sure Torr.	Gas Temp. ° C.	Substrate Temp. ° C.
		H_2	MTS	C_3H_8	CH_4			
708	1000	5625	375	-	-	220	800	1130
709	1000	5625	375	50	-	220	755	1130
710	1000	5625	375	50	-	380	768	1150
711	1000	6750	375	50	19	220	750	1130
712	1000	3750	250	60	-	230	785	1240

TABLE A-4: Deposition parameters for AlN Initial experiments

Run #	Gas Flow rates, ml/min					Pressure Torr	Gas Temp. °C	Al Pot °C	Substrate Temp. °C
	HCl	NH ₃	H ₂	Ar	N ₂				
840	475	50	-	-	3000	35	-	510	-
841	475	50	-	-	3000	25	500	500	590
842	475	50	-	-	3000	28	635	480	730
843	275	50	300	-	3000	30	1020	515	760
844	275	50	300	400	-	25	550	435	590
845	275	50	300	400	-	28	530	440	575
846	275	50	300	400	-	25	450	435	-
847	275	50	300	400	-	20	665	440	-
848	275	50	300	400	-	26	510	445	1080
849	275	50	300	400	-	25	455	440	1055
850	275	60	300	400	-	23	480	440	1030
851	275	50	300	400	-	25	465	440	1083
852	275	50	300	400	-	22	460	-	1050
853	275	50	300	400	-	27	650	445	1050
854	475	50	300	400	1500	28	460	-	1075
855	475	50	-	-	3000	28	430	-	1060
856	475	50	-	-	3800	28	425	-	1080
857	475	50	-	-	3000	28	440	-	1010

TABLE A-5: Deposition Parameters for AlN

Run #	HCl	Gas Flow rates, ml/min			Pressure Torr	Gas Temp °C	Al Pot Temp °C	Substrate Temp °C
		NH ₃	H ₂	Ar				
514	275	50	300	400	30	-	470	1100
515	275	50	300	400	33	-	470	1105
516	275	50	300	400	28	460	-	1125
517	275	50	435	2000	29	455	-	1160
518	275	135	435	400	19	460	-	1160
519	275	100	435	400	28	460	470	1300
520	275	80	435	2650	29	-	455	1285
521	275	80	435	400	33	-	450	1195
522	253	80	435	400	39	-	460	1175
523	233	80	435	400	48	-	455	1200
524	125	40	435	400	78	-	455	1210
525	253	80	435	400	54	-	-	1200
526	253	80	435	400	50	-	-	1200
527	252	85	435	400	40	455	-	1200
528	242	85	435	400	52	460	-	1200
529	126	40	435	400	64	465	-	1200
530	252	85	1000	400	66	445	-	1200
531	252	100	625	400	45	455	-	1200
532	232	100	435	400	47	460	-	1200
533	252	100	1000	400	45	465	-	1200
534	126	40	500	400	60	440	-	1200
534	126	40	500	400	58	-	455	1200

TABLE A-5 Continued: Deposition Parameters for AlN

Run #	Gas Flow rates, ml/min				Pressure Torr	Gas Temp °C	Al Pot Temp °C	Substrate Temp. °C
	HCl	NH ₃	H ₂	Ar				
535	202	100	435	400	47	-	445	1200
536	202	80	435	400	45	-	470	1200
619	202	100	435	400	50	570	430	1200
620	400	200	870	1000	43	560	415	1200
621	500	250	1087	2000	50	575	420	1200
622	500	250	1087	2000	45	540	425	1200
623	500	250	870	1500	35	515	430	1200
624	500	250	870	1500	50	530	435	1205
625	500	250	870	2500	50	540	445	1205
626	500	250	870	2500	50	455	420	1205-910
627	500	250	870	2500	50	620	440	1290
628	500	250	870	2500	45-320	525	435	1200
629	500	250	870	2500	50-60	700	440	1205
630	500	250	870	2500	90	755	440	1250
632	500	250	870	2500	50	575	435	1195
633	500	250	870	2500	60-65	580	425	1200
634	500	250	870	2500	52	650	445	1200
635	202	100	870	2500	50	500	430	955
636	400	200	870	2500	55	535	425	1025
637	400	100-300	870	2500	50	-	435	1020
638	500	250	870	2500	50	205	435	510

TABLE A-6: Deposition Parameters for AlN -- Oxygen Dopant Study

Run #	Gas Flow rates, ml/min						Pres- sure Torr.	Gas Temp °C	Al Pot Temp °C	Substrate Temp °C
	HCl	NH ₃	H ₂	Ar	CO ₂	H ₂ O				
639	500	250	870	2425	75	-	50	555	440	1020
640	400	300	870	1712	37.5	-	50	560	435	1025
641	400	533	870	1712	37.5	-	50	570	445	1015
642	400	533	870	1000	-	100 (w/air)	50	580	426	1010
643	400	533	870	1000	-	12.5-75 (w/air)	50	420	430	1025
644	400	533	870	1000	-	12.5-50 (w/air)	50	610	450	1015

TABLE A-7: Deposition Parameters for AlN -- Silicon Dopant Study

Run #	HCl	Gas Flow rates, ml/min				SiHCl ₃	SiCl ₄	Pres- sure Torr	Gas Temp °C	Al Pot Temp °C	Sub- strate Temp°C
	NH ₃	H ₂	Ar	N ₂							
645	400	533	870	2500	-	50	-	50	595	440	1020
646	400	400	870	2500	-	10	-	50	570	430	1020
647	400	400	870	2500	-	10	-	50	550	425	1020
648	400	400	870	2500	-	10	-	50	670	440	1125- 1320
649	400	400	870	2500	-	10	-	50	635	435	1120
650	400	400	870	2500	-	10	-	50	670	425	1220
651	400	400	870	2500	-	10	-	50	464	435	1120
652	-	700	20,000	-	18,000	-	600	65	635	-	1325
653	100	700	20,000	-	18,000	-	600	65	750	400	1350
654	200	700	20,000	-	18,000	-	600	65	800	430	1320
655	300	700	20,000	-	18,000	-	600	65	800	435	1320
656	300	700	20,000	-	18,000	-	600	65	640	380	1320
657	300	700	20,000	18,000	-	-	600	65	810	470	1310
658	400	700	20,000	18,000	-	-	600	90	800	425	1320
659	500	700	20,000	18,000	-	-	600	90	765	445	1320
660	400	400	870	2500	-	-	10	50	630	455	1150
661	400	400	870	2500	-	-	20	62	630	485	1155

TABLE A-8: Deposition Parameters for AlN -- Low Pressure Deposition Study

Run #	HCl	Gas Flow rates, ml/min				Pressure Torr	Gas Temp °C	Al Pot Temp °C	Substrate Temp °C
		NH ₃	H ₂	N ₂	SiCl ₄				
1	252.5	80	435	400	-	2.7	705	475	1235
2	252.5	80	435	400	-	3.2	705	505	1235
3	252.5	80	435	400	-	3.5	700	470	1235
4	252.5	80	435	400	-	3.2	690	500	1235
5	252.5	80	435	400	-	2.5	680	505	1235
6	252.5	80	435	400	-	2.3	680	480	1235
7	252.5	80	435	400	-	2.0	680	480	1220
8	252.5	80	435	400	-	2.0	705	500	1235
9	252.5	80	435	400	-	2.0	700	500	1250
10	252.5	80	435	400	-	1.8	-	-	1250
11	252.5	80	435	400	-	2.0	700	500	1225
12	252.5	80	435	400	-	1.7	700	500	1290
13	252.5	80	435	400	-	2.5	700	500	1230
14	252.5	80	435	400	50	2.5	650	500	1250
15	252.5	80	435	400	50	2.5	710	505	1400
16	252.5	80	435	400	50	2.5	700	500	1400-1485

APPENDIX B

A REPORT ON THE STUDY OF THE EFFECT OF SURFACE FINISH OF GRAPHITE SUBSTRATES ON THE TRS OF UNCOATED AND SiC-COATED BEND BARS

1. Scope

It is known that because of a high notch-sensitivity of brittle materials, the strength measurements are highly dependent upon the surface finish of the test specimen. The problem of surface finish is particularly complex for coatings of ceramic materials on a substrate such as graphite.

At SFL, one of the criteria used for the evaluation of materials made by chemical vapor deposition is the transverse rupture strength. An accurate determination of the TRS is dependent upon a variety of factors, such as surface finish of the coating, surface finish of the substrate, presence of sharp corners or edges on the specimen, alignment in the test set-up, etc. While the effects of misalignment have been quantified, those due to surface finish have not been addressed adequately. Therefore, the preliminary investigation reported herein was aimed at studying the effect of various surface finishes on the strength of uncoated SiC₆ graphite bend bars and bars coated with SiC. The overall aim of the program was to define the nature of surface finish of the substrate that would have the least influence on the scatter of the test data by possibly

eliminating the interface as an origin of the fracture-causing defect.

2. Experimental Procedure

- (a) Surface finish: After an examination of the surface finish of the as received bend bars of rectangular cross section made of SiC_6 graphite (nominal dimensions 2.5 mm x 5.0 mm x 76 mm), we decided to choose four different surface finishes for the preliminary investigations.

These are defined below:

<u>Designation</u>	<u>Surface preparation</u>
A :	None; substrates in as received (machined) condition.
B :	Fully polished on 600 grit SiC paper on all sides, with scratches running parallel to the length of the bar, edges chamfered.
C :	Edges chamfered. No other preparation carried out.
D :	Edges chamfered and short sides polished on 600 grit SiC paper with scratches running parallel to the long axis of the bar.

It will be noted that the order of the surface finish from worst to best is A, C, D, B. A total of 24 bars were prepared for each category. Twelve bars were retained for

strength measurement in the uncoated condition, and the other twelve were subjected to SiC deposition.

(b) Deposition of SiC: The deposition of SiC was carried out under constant conditions in the "flower pot" furnace. These were as follows:

Total pressure: 70 torr
Part temperature: 1070°C

Gas Flows:

N ₂	67,290 ml/min
H ₂	10,000 ml/min
MTS	600 ml/min
SiCl ₄	250 ml/min
Gas temperature	355°C (near inlet), 460°C near furnace
Run time	90 min.

Four bend bars were coated in each of the twelve runs, and then subjected to strength measurements.

(c) Measurement of TRS: The transverse rupture strength of all bend bars was measured on the Comten tester in a 3-point configuration. The load at failure was recorded and the TRS calculated according to the equation on p. 145 (of the text). In that equation the following values were inserted for various quantities:

P = the load at failure

$n = E_{\text{graphite}}/E_{\text{SiC}} \approx 0.02 \approx 0$

L = Loading span = 44.5 mm

x = Distance between central loading pin and origin of fracture.

b_1, h_1, b_2 and h_2 as defined in Figure 2
(of the text)

In the case of uncoated graphite substrates the following equation was used:

$$\sigma = \frac{3 P (L-2X)}{2b_1h_1^2}$$

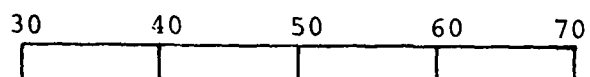
The strength values were then plotted as shown in Figures B-1 and B-2.

3. Results and Discussion

The TRS tests on uncoated graphite showed a trend that is not too surprising. The as-machined bars (A) had the maximum scatter in the strength (Figure B-1) while those bars with a better finish showed a relatively small scatter. It appears that a major source of scatter is the finish on the short side of the bar. However, the average strength values were reasonably close for the different finishes. It can be concluded that the graphite substrate is relatively insensitive to the surface finish within the scope of this work.

The results of tests on the coated bars, however, show a very significant effect of substrate surface finish

Flexure Strength, MPa



A —●— (12)

B —●— (10)

C —●— (12)

D —●— (12)

FIGURE B-1: EFFECT OF SURFACE FINISH ON THE FLEXURE STRENGTH OF UNCOATED GRAPHITE BEND BARS. THE FIGURES IN THE PARENTHESES INDICATE NUMBER OF SAMPLES TESTED. LETTERS ON LEFT INDICATE SURFACE FINISH DESIGNATION (SEE TEXT FOR DETAILS).

(Figure B-2). The strength of SiC on as received bars, type A, is very low. An application of the best surface finish (B) dramatically improves the strength of the coating from an average of about 395 MPa for type A to about 666 MPa for type B. The wide scatter in the strength of type C and D bars is puzzling. One of the reasons may be that some bars showed an assymetric fracture (i.e. fracture away from the center pin - $x \neq 0$). This may be related to structural inhomogeneity in the coating.

Very often, the four bars from the same run showed a wide scatter in the strength values. For example, in one run for type C bars, the four bars broke at values of 283, 400, 434 and 483 MPa, while for a run of 4 type D bars, the strength values were 262, 303, 379, and 621 MPa. On the other hand, some runs resulted in bars of much better consistency. For example, a run of type C bars gave strength values of 427, 455, 485 and 517 MPa. The scatter of strength values was not related to surface finish as can be seen in Table B-1. Thus, it appears that the scatter in the strength values of coated bars may, in part, be related to some unknown condition during deposition. The deposition conditions were kept nominally constant, but slight fluctuations of temperature or gas flow rates may have occurred that were not detectable.

Flexure Strength, MPa



A ———●———— (12)

B ———●———— (8)

C ———●———— (12)

D ———●———— (10)

FIGURE B-2: EFFECT OF SUBSTRATE SURFACE FINISH ON THE FLEXURE STRENGTH OF CNTD SIC COATING. FIGURES IN PARENTHESES INDICATE NUMBER OF SAMPLES TESTED. LETTERS ON LEFT INDICATE SURFACE FINISH DESIGNATION (SEE TEXT FOR DETAILS).

TABLE B-1: Strength of SiC deposited on SiC₀ graphite bend bars with different surface finishes

Surface Finish	Run No.	3-Point TRS, MPa		
A	2A-4488-427-152	400	227	304
	2A-4488-428-152	382	378	468
	2A-4488-435-152	526	411	322
B	2A-4488-432-152	596	636	545
	2A-4488-433-152	875	531	Samples retained for high temperature testing
	2A-4488-434-152	901	539	
C	2A-4488-424-152	664	719	872
	2A-4488-425-152	485	401	433
	2A-4488-426-152	519	427	459
D	2A-4488-429-152	685	380	592
	2A-4488-430-152	379	619	261
	2A-4488-431-152	770	672	Samples retained for high temperature testing

4. Conclusions

This preliminary study has shown that:

- (a) The graphite substrate is relatively insensitive to notch effect.
- (b) The surface finish on the substrate has a marked influence on the strength of the coating. The magnitude of the strength is increased and scatter reduced by applying a smooth, consistent surface finish. At the moment, light grinding on 600 grit paper and removal of sharp edges appears to provide the best consistency.
- (c) It appears that it is possible to further reduce the scatter due to inherent material variation by achieving a better control of the deposition chemistry.

APPENDIX C

X-RAY DIFFRACTION DETERMINATION OF THE SURFACE RESIDUAL STRESS AND ELASTIC PROPERTIES OF β -SiC COATINGS ON GRAPHITE SUBSTRATES

Introduction

San Fernando Laboratories contracted Lambda Research Inc., Cincinnati, Ohio, to carry out determination of surface residual stress and elastic constants of CNTD β -SiC deposits. We provided Lambda Research with nine samples of various geometries. All samples were nominally 125-200 μ m thick coatings on SiC₆ graphite substrates. In all, two flat specimens having dimensions 38.1 x 38.1 x 12.7 mm, three small cylindrical samples approximately 12.7 mm dia x 51 mm long and one large cylindrical sample 38.1 mm dia x 51 mm long were provided for the residual stress measurement. Three flat plates, approximately 19 x 115 x 2.5 mm thick were provided for the X-ray elastic constant determination. These constants were to be used in the measurement of residual stress.

The report, issued by Lambda Research is included with minor changes for uniformity of units.

Technique:

The test specification called for performing x-ray diffraction residual stress measurements in directions parallel and transverse (perpendicular) to one reference edge chosen arbitrarily on one of the flat test specimens.

Measurements were to be made on the square face at the center and at distances of nominally 2.5, 5.1, 7.6 and 10.2 mm from the center of the specimen along a line perpendicular to the reference edge.

X-ray diffraction residual stress measurements were made on the 38.1 mm and on one of the 12.7 mm diameter beta silicon carbide coated specimens on the cylindrical surface at a position chosen arbitrarily around the circumference of the cylinder. Measurements were made at the center and at distances of 5.1, 10.2, 15.2 and 20.3 mm displaced from the center along the cylindrical face of the specimen toward one end. At each measurement site on both the 12.7 mm and 38.1 mm diameter cylinders measurements were made in the longitudinal and circumferential directions.

X-ray diffraction residual stress measurements were made by the Two-Inclined Angle technique employing the diffraction of chromium K-alpha radiation from the (311) planes of the FCC structure of the beta silicon carbide coating. Diffraction peak angular positions were determined employing a five-point parabolic regression procedure after correction for the Lorentz-polarization and absorption effects, and for a linearly sloping background intensity. Details of the diffractometer fixturing are outlined in Table C-1.

The value of the single crystal elastic constant $E/(1 + \nu)$ for the crystallographic direction normal to the (311) planes of the beta silicon carbide FCC lattice was

TABLE C-1

Diffractometer Parameters

Incident Beam Divergence:		1.0 degree
Receiving Slit	:	0.5 degree
Detector	:	Si(Li) set for 90% acceptance of the chromium K-alpha energy
Counts per Point	:	10,000
Psi Rotation	:	0.0-45.0 degree
$E/(1 + \nu)$:	476 ± 3.5 GPa
Irradiated Area	:	2 x 2.5 mm (long axis aligned perpendicular to the direction of measurement)

determined experimentally in the course of the investigation by loading a simple rectangular beta silicon carbide coated graphite beam in four-point bending on the diffractometer and determining the change in the lattice spacing of the (311) planes as a function of applied stress. The sample was strain gaged so that the output of the full bridge circuit was proportional to the average strain on the surface which was irradiated by the x-ray beam when placed in the four point bending fixture. Determinations were made of the change in spacing of the (311) planes between psi angles of 0.0 and 45.0 deg. for applied stresses of approximately 0.0, 115, 229 and 344 MPa based upon the box beam calculation. The resulting data set provided a total of sixteen independent determinations of the observed shifts in the lattice in the (311) planes for a psi rotation of 45° over the applied stress range. The slope of a plot of the change in the lattice spacing as a function of applied stress was determined by linear least squares regression. The single crystal elastic constant $E/(1 + \nu)$ in the (311) direction was then determined from the slope of a plot of the change in d (311) as a function of applied stress. Details of the procedure are described in P.S. Prevey, "A Method of Determining the Elastic Properties of Alloys in Selected Crystallographic Directions for X-Ray Diffraction Residual Stress Measurement," Advances in X-Ray Analysis, Vol. 20, Plenum Press, 1977, pp. 345-354.

Attempts were made to obtain data as a function of depth beneath the surface of the beta silicon carbide coated

graphite specimens. Initially, an effort was made to remove layers of silicon carbide by etching in a molten salt bath. A small salt bath heat treating furnace was used and the specimen was immersed in the molten salt. After exposure to the molten salt for a period of an hour, no significant removal could be detected employing a micrometer with the least count of 2.5 micron. A second attempt was made to remove layers of material by lapping the surface of the flat specimen against a glass plate using six micron diamond dust as an abrasive. After approximately four hours of lapping, it was found that the surface of the specimen was concave and that material was being removed only from the perimeter of the flat specimen. The surface was judged to be sufficiently concave so that accurate measurements of the amount of material removed would not be possible. Further attempts to perform subsurface residual stress measurements on the flat samples as called for in the test specifications were abandoned.

Because all results obtained in this investigation are based upon surface data only, it was not possible to correct the data obtained for the effects of penetration of the radiation employed for subsurface residual stress measurement into any subsurface stress gradient which may be present in the specimens.

Mechanical Elastic Property Determination

As mentioned above under the discussion of the determination of the x-ray elastic constants $E/(1 + \nu)$ in the (311) direction, the actual stress in the beta silicon carbide coating on the surface of the graphite simple beam specimens when placed in four-point bending was calculated from the MC/I formulation for a simple box beam. The MC/I calculation was initially carried out assuming the specimen was a homogeneous solid beam. The calculations were modified by a factor after the beam failed at a load of approximately 345 MPa during the determination of the x-ray elastic constants. Following failure, the beam was returned to the San Fernando Laboratories where the actual thickness of beta silicon carbide coating was measured so that the box beam calculation could be performed. It was found at that time that the stress in the outer fiber assuming a box beam of beta silicon carbide with no significant support from the graphite interior was a factor of 3.35 times higher than the stress calculated assuming a homogeneous solid beam.

In order to perform the determination of the x-ray elastic constants, the simple beam specimen had been dead weight loaded repeatedly and the strain output from the full bridge attached to the tension face had been recorded for repeated applications of a known applied stress. If Poisson's ratio for the beta silicon carbide coating was also known, the mechanical value of Young's modulus, E , could be determined.

A second rectangular beam with nominally similar dimensions was instrumented on both the tension and compression sides in four-point bending with a single grid on each face in the longitudinal and one in the transverse direction. The strains were measured independently for each of the four strain gages for twenty-six independent changes in the applied stress. Poisson's ratio was then calculated from the ratio of the transverse and longitudinal strains for each of the twenty-six incremental changes in applied stress for both the tension and compression sides of the beam separately. The determination of Poisson's ratio in this manner of direct strain readings was totally independent of the material properties and the geometry of the simple beam with respect to coating thickness. It was only necessary to assume that uniform stress was applied in four point bending over the local area occupied on each face of the specimen by the longitudinal and transverse strain gages.

The total strain measured with the full bridge of two longitudinal and two transverse gages applied to the tensile face of the specimen which was employed for the determination of the x-ray elastic constants is equal to twice the longitudinal strain plus twice Poisson's ratio times the longitudinal strain. Knowing Poisson's ratio from the results obtained on the second beam described above, it was then possible to determine E and ν independently from the data obtained in dead weight loading of the calibration beam.

RESULTS AND DISCUSSIONS

Determination of X-ray Elastic Constants

The results of the determination of the single crystal elastic constants $E/(1 + \nu)$ for the (311) crystallographic direction of beta silicon carbide coating are presented graphically in Figure C-1. Reduction of these data as described above yields $E/(1 + \nu)$ equal to 476 ± 3.7 GPa. The value of $E/(1 + \nu)$ obtained for the (311) direction was employed to calculate the macroscopic residual stress from the microscopic strain measured in the crystal lattice in the reduction of residual stress data which follows. Details of the reduction of the data obtained to determine $E/(1 + \nu)$ are therefore shown in Table C-1. The accuracy, to one standard deviation, of x-ray elastic constants typically determined for metallic specimens which can be loaded in tension to stresses on the order of 480 to 690 MPa is typically on the order of $\pm 1\%$. The inordinately high uncertainty in these data is due not to any increased uncertainty in the change in lattice spacing measured, but rather to the limited range of stress which could be applied to the specimen and the high elastic modulus of silicon carbide.

An estimate of the stress applied in tension on the face of the box beam at the time of failure can be made. The beam was known to have sustained a load of 345 MPa in tension during the calibration procedure to determine $E/(1 + \nu)$ in the (311) direction. Although the precise strain level at

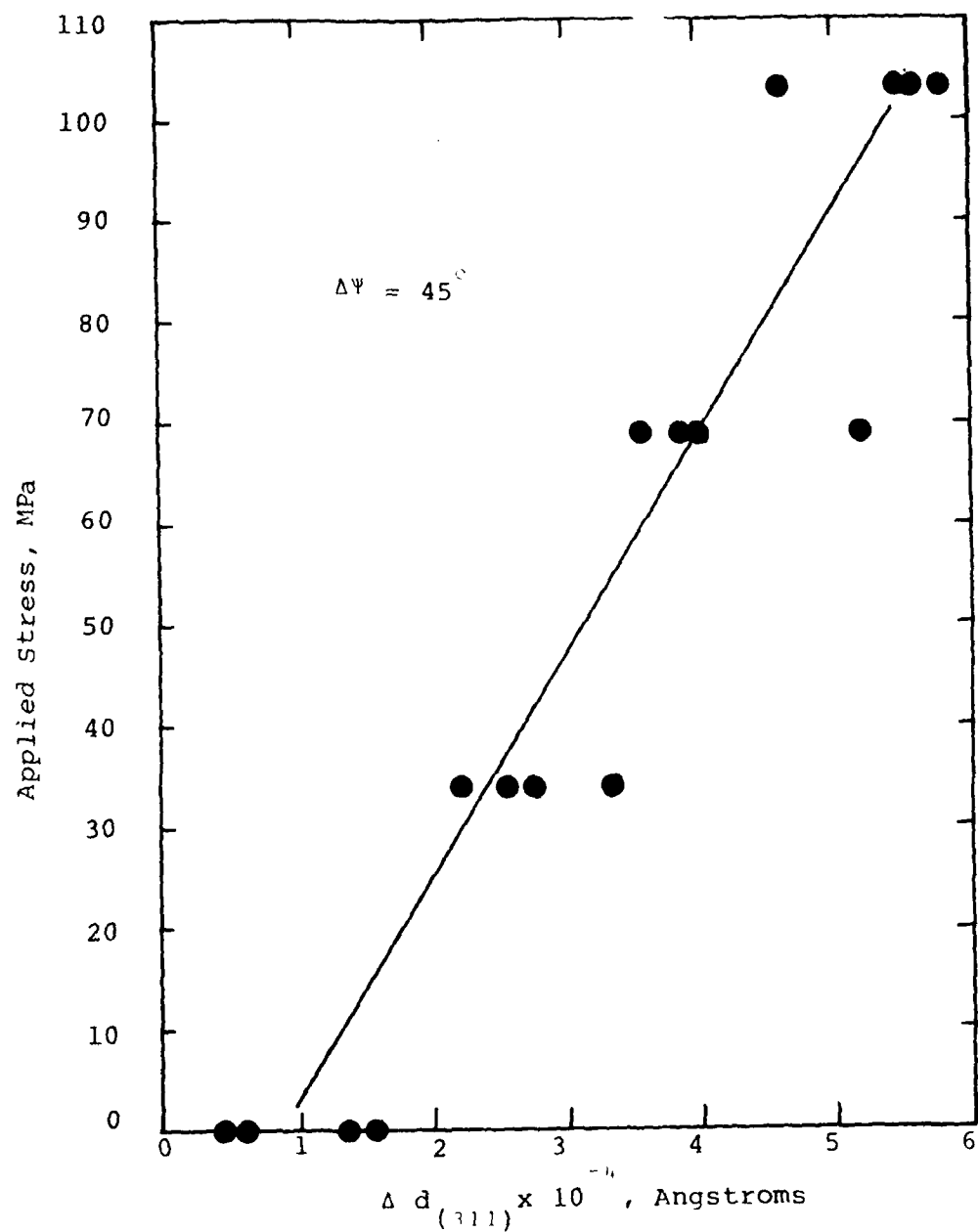


FIGURE C-1: CHANGE IN THE (311) LATTICE SPACING OF CNTD SiC AS A FUNCTION OF APPLIED STRESS.

the time of failure was not recorded because it was not of interest at the time, it is believed that the specimen failed after sustaining an applied stress of 404 MPa in tension for a period of a few seconds. It should be noted here that this breaking stress level is based upon the author's recollection rather than written documentation. The specimen is known to have sustained the load of 345 MPa in tension. After failure of the beam employed for the determination of the x-ray elastic constants, San Fernando Laboratories reported that the coating thickness at the point of fracture was 160 and 185 microns on the tensile and compression faces and 193 and 213 microns on the opposite edges. Assuming a ratio of elastic moduli for the two materials of 0.0222, and performing the calculation for the box beam, it was found that the outer fiber stress for the box beam was 3.35 times higher than the homogeneous simple beam case. This factor was used to adjust all of the applied stress calculations made on the simple rectangular beam.

The results of the determination of Poisson's ratio from strains measured in the longitudinal and transverse directions on both the tension and compressive sides of the second rectangular beam for twenty-six incremental changes in applied stress yield values of 0.18 for the tension side and 0.17 for the compression side. If the average of these values, 0.18 ± 0.02 is assumed to be the correct value of Poisson's ratio, then Young's modulus, based upon the strains measured on the beam used for the determination of the x-ray elastic

constants would be 462 ± 21 GPa, in agreement with values reportedly determined previously for beta silicon carbide.

X-ray Diffraction Residual Stress Measurements

The longitudinal, transverse and circumferential residual stresses measured on the one flat and two cylindrical beta silicon carbide coated graphite specimens examined are presented in Table C-2. Compressive stresses are shown as negative values, tensile as positive in units of MPa. All of the residual stresses measured in the silicon carbide coating on the three samples were found to be in compression.

The results obtained for the flat sample measured from the center out towards one edge in the longitudinal direction ranged from a minimum compressive stress of 10 MPa at the 5.1 mm location to a maximum compressive stress of 2331 MPa at a distance of 2.5 mm. The results in the transverse direction ranged from a minimum compressive stress of 600 MPa at the 51 mm location to a maximum of 1634 MPa at 7.6 mm from the center. The results appear to show a region of lower compression in the vicinity of the 5.1 mm distance from the center in both cases. There is, however, insufficient data to firmly establish this trend.

The results obtained on the 12.7 mm diameter cylinder in the longitudinal and circumferential directions are presented in Table C-2. These results show longitudinal stresses from the center of the cylinder out to a distance of 20.3 mm toward one end ranging from a minimum of 186 MPa at

TABLE C-2

SURFACE RESIDUAL STRESS β -SiC

COATED GRAPHITE

Flat Sample

Location (mm, from center)	Residual stress, MPa	
	Longitudinal	Transverse
0.0	-1795	-1276
2.5	-2330	-1241
5.1	- 10	- 600
7.6	- 917	-1634
10.2	-1108 (-1569)	- 669

() indicates repeat measurement

12.7 mm dia. cylinder

Location (mm, from center)	Longitudinal	Circumferential
0.0	-1062	-1800
5.1	- 634	-1117
10.2	- 186	- 821
15.2	- 965	- 903
20.3	-1490	- 924

38.1 mm dia. cylinder

Location (mm, from center)		
	- 88	-1469
0.0	-1214	-1655
	- 497	-1069
5.1	-1360	-1048
10.2	- 903	- 290
15.2		
20.3		

the 10.2 mm location to a maximum compressive stress of 1490 MPa at the 20.3 mm location. The circumferential results for the 12.7 mm diameter cylinder ranged from a minimum of 821 MPa at the 10.2 mm location to a maximum of 1800 MPa at the center. There again appears to be a tendency towards lower compression at the 10.2 mm location in both the longitudinal and circumferential directions.

The results for the 38.1 mm diameter cylinder do not appear to show any significant trend. The longitudinal results ranged from a minimum of 88 MPa at the center to a maximum compressive stress of 1359 MPa at the 15.2 mm location. The circumferential results for the 38.1 mm diameter cylinder ranged from a minimum of 290 MPa at the 20.4 mm location to a maximum compressive stress of 1655 MPa at the 5.1 location.

As shown at the top of Table C-2 repeat measurements made by repositioning the flat sample for the longitudinal direction at the 10.2 mm location yielded values of 1108 and 1569 MPa. The question of reproducibility was, therefore, investigated to determine the accuracy of the measurements being performed. Three repeat measurements were made on the flat sample at the 10.2 mm location in the longitudinal direction without replacing the sample between measurements. These results, as summarized in Table C-3 show values ranging from 1614 MPa to 1675 MPa. These results appear to indicate that the accuracy of the measurements made at the relatively

TABLE C-3

REPEAT RESIDUAL STRESS MEASUREMENTS

Beta Silicon Carbide

SiC Sample Repositioned

Flat Sample 5.1 mm longitudinal -1108 MPa

SiC Sample Static:

Flat Sample 5.1 mm, longitudinal -1614 MPa

-1674 MPa

-1667 MPa

low diffraction angle of nominally 121° available for this material is on the order of 34 MPa eliminating errors due sample repositioning.

When the sample is repositioned, the presence of a surface residual stress gradient and failure to reposition the measurement site exactly in the plane of the surface and errors in displacement of the diffracting volume from the center of the goniometer both can cause significant error. If, as appears to be the case for the silicon carbide coatings, there is a significant residual stress gradient across the surface, difficulty in reproducing measurements can result from the former source. The lower the angle, 2θ , the larger the error due to sample positioning uncertainty. At a diffraction angle of approximately 130° the error is on the order of 14 MPa per 2.5 mm of displacement of the sample. At a diffraction angle of approximately 155° the error drops to approximately 3 MPa per 2.5 mm displacement. The effect of sample displacement errors on measurements in β -silicon carbide at a diffraction angle of 121° appears to be on the order of ± 276 MPa based upon the results shown in Table C-3.

Details of the x-ray diffraction data reduction are shown in the computer printouts appended to this report. The error shown for each residual stress measurement is \pm one standard deviation resulting from random error in the determination of the diffraction peak angular positions and in

the empirically determined value of $E/(1 + \nu)$ in the (311) direction. An additional semi-systematic error of less than ± 14 MPa may result from instrument alignment errors. The magnitude of this systematic error was monitored using a powdered metal zero-stress standard, and found to be 15 MPa during the course of this investigation.

CONCLUSIONS

The results of this investigation of the residual stresses at the surface of the silicon carbide coatings deposited on a graphite substrate indicate entirely compressive residual stresses for both the flat and the 12.7 and 38.1 mm diameter cylindrical specimens examined. The residual stresses ranged from a minimum of approximately -7 to a maximum of -2331 MPa. An analysis of the uncertainty in the peak measurements which was the only technique available, shows a repeatability due to sample displacement errors which appears beyond the order of ± 276 MPa. This sample displacement error is much larger than the ± 3.5 MPa typically associated with metallic samples, and appears to be due in part to both the presence of a significant stress gradient across the surface of the specimens and an increased sensitivity, due to the low diffraction angle, to displacement of the diffracting volume from the center of the goniometer during measurement.

The x-ray elastic constants in the (311) direction were determined during the course of this investigation to be 476

± 3.5 GPa for the quantity $E/(1 + \nu)$. The bulk elastic properties were determined from data obtained on two rectangular beam specimens placed in four point bending. Young's modulus was found to be $E = 462 \pm 21$ GPa and Poisson's ratio 0.18 ± 0.02 . The tensile breaking stress in four point bending was calculated to be in excess of 1345 MPa based upon the box beam calculation for the silicon carbide coating.

Examination of partial diffraction patterns obtained for the material in the course of this investigation appears to indicate the presence of quantities of free silicon in the silicon carbide material. No attempt was made to precisely determine the secondary phases present.

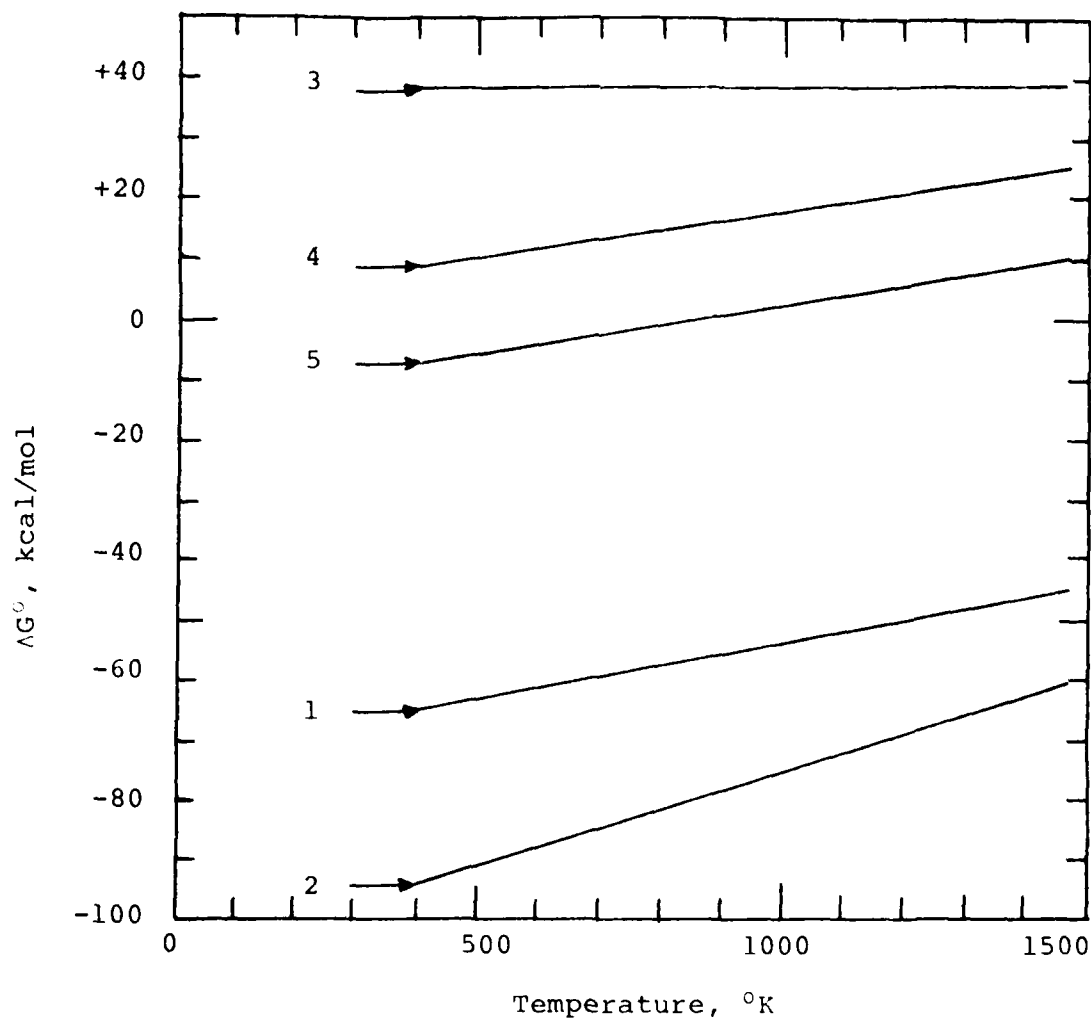
Attempts were made to obtain subsurface residual stress results by etching away layers in a molten salt bath and by lapping the surface to a flat sample with six micron diamond dust. Neither procedure proved to be effective. No measurable amount of material was removed by the molten salt bath after one hour of exposure. The flat sample was sufficiently concave on the surface to render removal by lapping against a flat glass plate useless. It was not possible to determine the precise depth of material removed in the lapping process. Further attempts to obtain subsurface data were, therefore, abandoned.

APPENDIX D
ALUMINUM NITRIDE THERMOCHEMISTRY

The AlN deposition process can be examined in terms of three separate reaction zones: the aluminum burner pot, the gas mixing zone, and the deposition area.

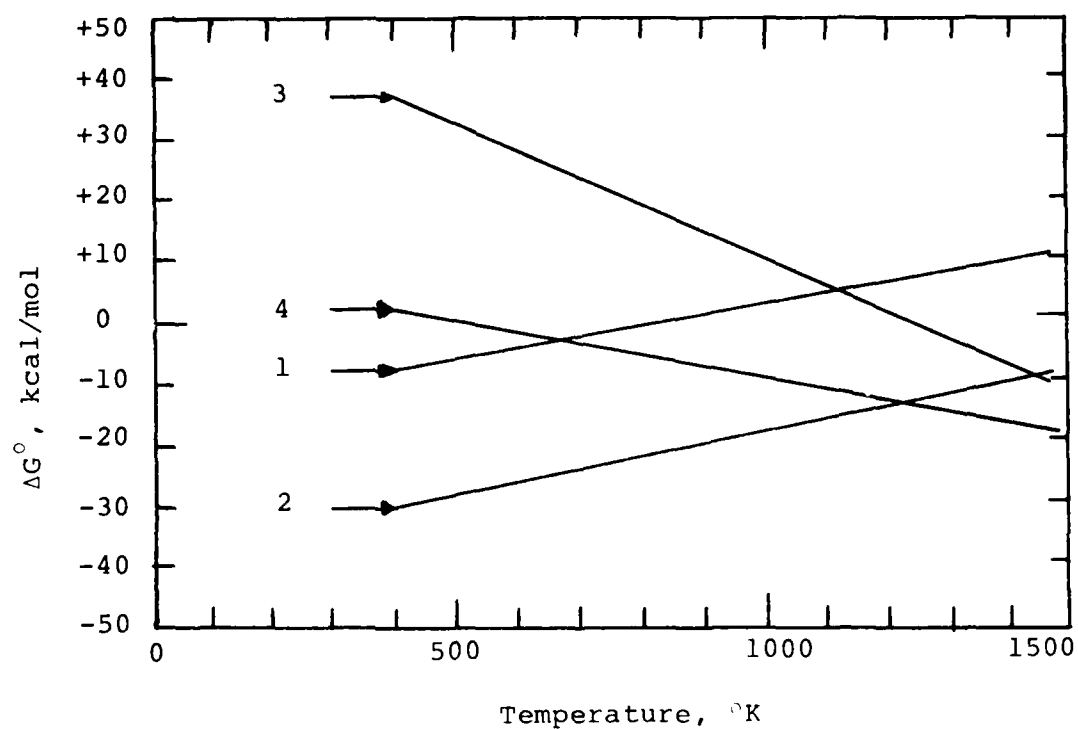
In the aluminum burner pot we are concerned with the reaction of granular aluminum with HCl gas. Figure D-1 displays the free energy of reaction vs. temperature²⁴ for several chemical reactions which must be considered in our analysis of the burner pot operation. It is apparent that theoretically HCl should not affect the oxide film which covers the aluminum granules in the pot. (Reactions #3 and #4). Since we know that at a pot temperature of about $400^{\circ} - 450^{\circ}\text{C}$ ($673-723^{\circ}\text{K}$), the HCl does in fact react with the granular aluminum, then somehow the HCl must be able to penetrate the oxide layer to react with aluminum metal. The reaction of HCl with aluminum metal is quite energetic (See Reaction #1). It is likely that as the pot is heated, the differences in the expansion coefficients of Al and Al_2O_3 might cause fracturing of the surface film and allow exposure of Al to the HCl gas.

In the gas phase mixing zone, gaseous AlCl_3 produced in the burner pot is mixed with gaseous ammonia carried with hydrogen and nitrogen (See Figure D-2). Actually, below about 850°K , gaseous AlCl_3 exists as a dimer, Al_2Cl_6 (reaction 1, Figure D-2). At temperatures below 1100°K the



- (1) $\text{Al (s)} + 3\text{HCl (g)} \longrightarrow \text{AlCl}_3 \text{ (g)} + \frac{3}{2} \text{H}_2 \text{ (g)}$
- (2) $\text{Al (s)} + \text{HCl (g)} + \text{H}_2\text{O (g)} \longrightarrow \text{AlClO (g)} + \frac{3}{2} \text{H}_2 \text{ (g)}$
- (3) $\frac{1}{2} \text{Al}_2\text{O}_3 \text{ (s)} + 3\text{HCl (g)} \longrightarrow \text{AlCl}_3 \text{ (g)} + \frac{3}{2} \text{H}_2\text{O (g)}$
- (4) $\frac{1}{2} \text{Al}_2\text{O}_3 \text{ (s)} + \text{HCl (g)} \longrightarrow \text{AlClO (s)} + \frac{1}{2} \text{H}_2\text{O (g)}$
- (5) $2 \text{HCl (g)} + \frac{1}{2} \text{O}_2 \text{ (g)} \longrightarrow \text{H}_2\text{O (g)} + \frac{1}{2} \text{Cl}_2 \text{ (g)}$

FIGURE D-1: CHANGE IN THE FREE ENERGY OF FORMATION AS A FUNCTION OF TEMPERATURE FOR REACTIONS IN THE ALUMINUM CRUCIBLE IN THE CVD OF ALN.

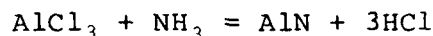


- (1) $\text{AlCl}_3 (\text{g}) \longrightarrow \frac{1}{2} \text{Al}_2\text{Cl}_6 (\text{g})$
- (2) $\text{AlCl}_3 (\text{g}) + \text{NH}_3 (\text{g}) \longrightarrow \text{AlCl}_3 \cdot \text{NH}_3 (\text{g})$
- (3) $\text{AlCl}_3 \cdot \text{NH}_3 (\text{g}) \longrightarrow \text{AlN} (\text{s}) + 3\text{HCl} (\text{g})$
- (4) $\text{AlCl}_3 (\text{g}) + \text{NH}_3 (\text{g}) \longrightarrow \text{AlN} (\text{s}) + 3\text{HCl} (\text{g})$

FIGURE D-2: CHANGE IN THE FREE ENERGY OF FORMATION AS A FUNCTION OF TEMPERATURE FOR REACTIONS IN THE GAS PHASE AND DEPOSITION CHAMBER IN THE CVD OF ALN.

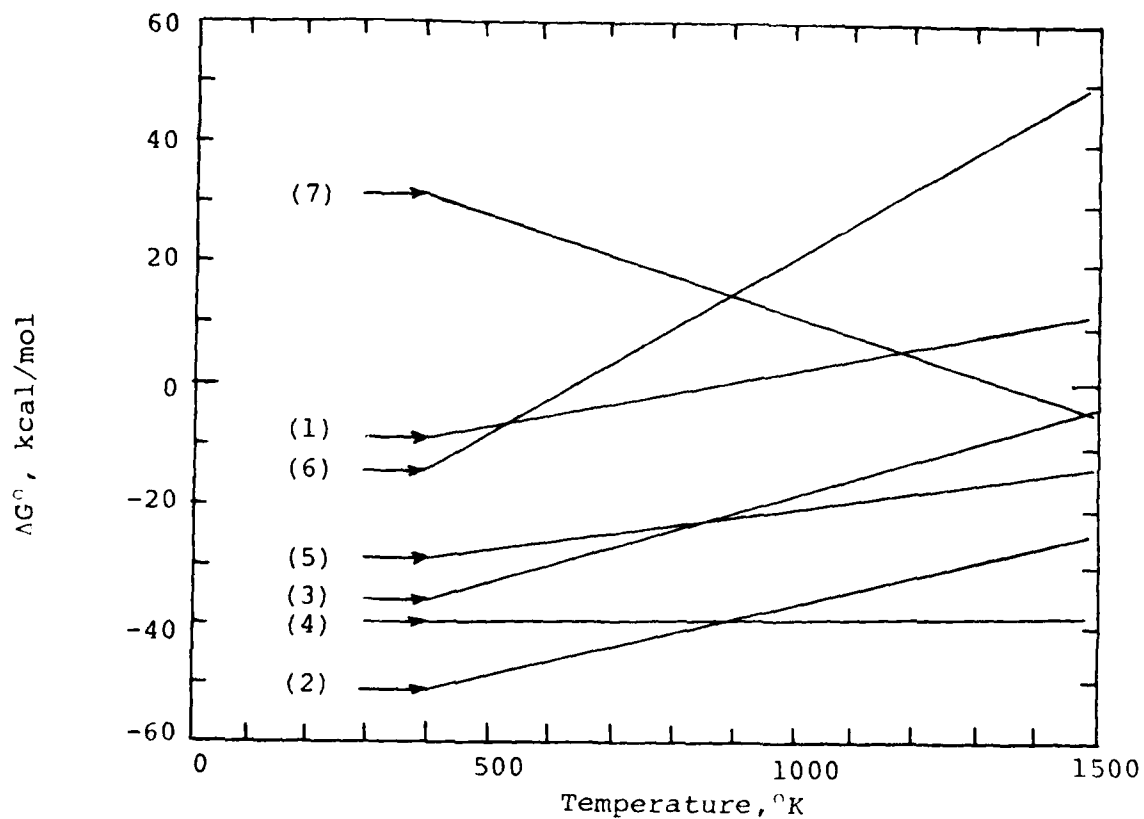
primary reaction will give a $\text{AlCl}_3 \cdot \text{NH}_3$ complex. This will not become thermodynamically unstable with respect to AlN formation until about 1200°K .²⁵ Therefore, in the absence of any contaminants, we should have a stable gas phase mixing zone at temperatures between that of the burner pot ($\sim 700^\circ\text{K}$) and the deposition furnace @ $>1200^\circ\text{K}$.

The deposition area must be held at a temperature greater than about 1200°K , in order to favor the AlN formation. Above this temperature the reaction



proceeds directly and the $\text{AlCl}_3 \cdot \text{NH}_3$ complex will decompose into AlN and 3HCl.

Water and oxygen undoubtedly comprise most of the contamination in the system. Water is available from the aspirator vacuum. Therefore, a liquid nitrogen cold trap in the vacuum line is necessary to protect the deposition chamber. Oxygen and water are both potentially available through system leaks, but water will also come from the ammonia supply tank. The primary effect of these contaminants is the formation of $\text{Al}_2\text{O}_3(\text{s})$ upon reaction with $\text{AlCl}_3(\text{g})$. A secondary reaction which should occur somewhat less readily will produce $\text{AlClO}(\text{s})$. $\text{AlClO}(\text{s})$ will react with $\text{NH}_3(\text{g})$ to form AlN(s) above 1300°K . At lower temperatures (less than $\sim 900^\circ\text{K}$) the $\text{AlCl}_3(\text{g})$ can possibly produce some $\text{SiCl}_4(\text{g})$ contaminant by reacting with the quartz chamber walls. (See



Reactions:

- (1) $\text{AlCl}_3 (\text{g}) + \frac{3}{4} \text{SiO}_2 (\text{s}) \longrightarrow \frac{1}{2} \text{Al}_2\text{O}_3 (\text{s}) + \frac{3}{4} \text{SiCl}_4 (\text{g})$
- (2) $\text{AlCl}_3 (\text{g}) + \frac{3}{4} \text{O}_2 (\text{g}) \longrightarrow \frac{1}{2} \text{Al}_2\text{O}_3 (\text{s}) + \frac{3}{2} \text{Cl}_2 (\text{g})$
- (3) $\text{AlCl}_3 (\text{g}) + \frac{1}{2} \text{O}_2 (\text{g}) \longrightarrow \text{AlClO} (\text{s}) + \text{Cl}_2 (\text{g})$
- (4) $\text{AlCl}_3 (\text{g}) + \frac{3}{2} \text{H}_2\text{O} (\text{g}) \longrightarrow \frac{1}{2} \text{Al}_2\text{O}_3 (\text{s}) + 3 \text{HCl} (\text{g})$
- (5) $\text{AlCl}_3 (\text{g}) + \text{H}_2\text{O} (\text{g}) \longrightarrow \text{AlClO} (\text{s}) + 2 \text{HCl} (\text{g})$
- (6) $\text{NH}_3 (\text{g}) + \text{HCl} (\text{g}) \longrightarrow \text{NH}_4\text{Cl} (\text{s})$
- (7) $\text{AlClO} (\text{s}) + \text{NH}_3 (\text{g}) \longrightarrow \text{AlN} (\text{s}) + \text{HCl} (\text{g}) + \text{H}_2\text{O} (\text{g})$

FIGURE D-3: CHANGE IN THE FREE-ENERGY OF FORMATION AS A FUNCTION OF TEMPERATURE OF SECONDARY REACTION PRODUCTS IN THE CVD OF ALN.

Figure D-3). Thus, the various sources of contamination present in the system will tend to affect the composition of AlN. It should be possible to minimize these reactions by a careful reactor design and selection of gases.

REFERENCES

1. Holzl, R. A., Proceedings of Sixth International Conference on CVD, Atlanta, GA (1977), p. 107.
2. Stiglich, J. J., Bhat, D. G. and Holzl, R. A., Ceramurgia International, 6, 3 (1980).
3. Popov, E. P., "Introduction to Mechanics of Solids", Prentice-Hall, Inc., Englewood Cliffs, N. J. (1968), p. 202.
4. Evans, A. G. and Charles, E. A., J. Amer. Ceram. Soc., 59, 371 (1976).
5. Holzl, R. A., AFOSR Final Report, Contract No. F49620-77-C-0068, March 1979.
6. Dutta, S., Rice, R. W., Graham, H. C. and Mendiratta, M. G., NASA TM-79277, Paper presented at 80th Annual Meeting of American Ceramic Society, Detroit, Michigan, May 1978.
7. Hirsch, P. B., Howie, A., Nicholson, R. B., Pashley, D. W. and Whelan, M. J., "Electron Microscopy of Thin Crystals", Butterworths, London (1969), p. 357.
8. Rice, R. W., Naval Research Laboratory, Washington, D. C., Private Communication.
9. Powell, C. F., Oxley, J. H. and Blocher, J. M. (Eds.), "Vapor Deposition", John Wiley & Sons, Inc., New York (1967), p. 655.
10. Guentert, O. J., J. Chem. Phys., 37, 884 (1962).
11. Weiss, J. R., Ph. D. Thesis, Rensselaer Polytechnic Institute (1974).
12. Lynch, J. F., Ruderer, C. G., and Duckworth, W. H., Battelle Memorial Institute Report No. AD-803-765, June 1966.
13. Scace, R. I. and Slack, G. A., in "Silicon Carbide" (O'Connor, J. R. and Smittens, J. (Eds.), Pergamon Press, New York (1960), p. 24.
14. Quinn, G., AMMRC TN 77-4, August 1977.

15. Larsen, D. C. and Adams, J. W., IITRI Semi-annual Report No. 8, AFML Contract No. F33615-79-C-5100, June 1980.
16. McLean, A. F., Fisher, E. A. and Bratton R. J., AMMRC CTR 72-19, Interim Report, Contract No. DAAG 46-71-C-0162, September 1973.
17. Srinivasan, M., Carborundum Company, Niagara Falls, New York, Private Communication.
18. Lewis, D., J. Electrochem Soc., 117, 978 (1970).
19. Kirkorian, O. H., Report No. UCRL 6132, University of California, Lawrence Radiation Laboratory, Livermore, CA, (1960).
20. Bhat, D. G., Final Technical Report, U. S. Naval Air Systems Command, Contract No. N0019-78-C-0557, October 1980.
21. Taylor, K. and Lenie, C. J., J. Electrochem. Soc., 107, 308 (1960).
22. Weiloniski, R. F., AFML Report No. TR-78-31, May 1978.
23. Fridlender, B. A., Neshpor, V. S., Eron'yan, M. A. and Bychkov, A. Kh., Tepl. Vys. Temp., 15(3), 668 (1977).
24. Bauer, J., Biste, L. and Bolze, D., Phys. Stat. Solidi (9), 39, 173 (1977).
25. JANAF Thermochemical Tables, Second Edition, July 1970.